

**Mechanical Properties of Dual Phase Alloys
Composed of Soft and Hard Phases**

2016

Hongxing Li

Mechanical Properties of Dual Phase Alloys Composed of Soft and Hard Phases



By

Hongxing Li

A dissertation submitted to Kyoto University for
Doctor of Philosophy in Engineering

Department of Materials Science and Engineering
Graduate School of Engineering

Kyoto University

2016

Table of Contents

Chapter 1: Background and purpose	1
1.1. Introduction.....	1
1.2. Dual phase steels.....	5
1.3. Dual phase non-ferrous alloy	9
1.4. Objective of present study.....	11
1.5. Experimental methods.....	14
1.5.1. Nanoindentation	14
1.5.2 Digital image correlation (2D-DIC)	17
1.5.3. In-situ neutron diffraction.....	19
1.6. Outline of dissertation.....	22
Reference	
Chapter 2: Influence of tempering on mechanical properties and microstructure in dual phase steel composed of ferrite and martensite	25
2.1. Introduction.....	25
2.2. Experimental procedure	27
2.3 Effect of tempering temperature on microstructure evolution.....	30

2.4. Effect of tempering temperature on mechanical properties	36
2.4.1. Nanohardness change of martensite and ferrite phases	36
2.4.2. Stress-strain behaviors	38
2.4.3. Effect of tempering temperature on strength and elongation	40
2.4.4. Relationship between strength-elongation and nanohardness ratio of martensite to ferrite.....	42
2.5. Discussion	43
2.5.1. Mixture rule	44
2.5.2. Work-hardening behavior	46
2.6. Conclusions.....	50
References	

**Chapter 3: Effect of hardness ratio between two phases on deformation behavior
in dual phase steel..... 56**

3.1 Introduction.....	56
3.2 Experimental procedure	57
3.2.1. Materials	57
3.2.2 Local strain measurement by DIC method.....	57
3.3 Strain partitioning in martensite-based dual phase steel.....	60

3.3.1 Strain partitioning in specimen A (M/F=1.1)	61
3.3.2 Strain partitioning in specimen B (M/F=1.34)	63
3.4.3 Strain partitioning in specimen C (M/F=1.59)	66
3.4.4 Comparison of the deformation behaviors of specimens with different hardness ratios	70
3.4.5 Discussion.....	72
3.6 Conclusions.....	75
Reference	

**Chapter 4 Effect of volume fraction of martensite on deformation behavior in dual
phase steel..... 78**

4.1. Introduction.....	78
4. 2. Experimental procedure	80
4.3. Comparson of tempering temperature on microstructure evolution in martensite-based DP steel and ferrite-based DP steel.....	82
4.4 Comparson of tempering temperature on microstructure evolution.....	86
4.4.1 Nanohardness change of martensite and ferrite phases:	86
4.4.2 Stress-strain behaviors.....	89
4.4.3 Effect of tempering temperature on strength and elongation.	91

4.5 Effect of hardness ratio between two phases on deformation behavior in ferrite-based dual phase steel	95
4.5.1 Strain partitioning in specimen A (M/F=1.23)	95
4.5.2 Strain partitioning in specimen B (M/F=1.26)	98
4.5.3 Strain partitioning in specimen C (M/F=1.69)	100
4.5.4 Comparison of the deformation behaviors of specimens with different hardness ratios	103
4.5.5 Comparison of the deformation behaviors of specimens in ferrite-based DP steels and martensite-based DP steels with different hardness ratios	105
4.6 Discussion	107
4.7 Conclusions	110
Reference	

Chapter 5: Microstructure and mechanical properties of dual phase Cu-Zn alloy composed of soft and hard phases.....	113
5.1. Introduction	113
5.2. Experimental procedure	115
5.3. Results and discussion	118
5.3.1 Microstructure and phase identification of specimens before deformation ..	118

5.3.2 Mechanical properties.....	123
5.3.3 Microstructure and mechanical properties change in Specimen A ($f_{\alpha}=75.1\%$)	125
5.3.4 Microstructure and mechanical properties change in Specimen B ($f_{\alpha}=55.6\%$)	133
5.3.5 Microstructure and mechanical properties change in Specimen C ($f_{\alpha}=18.4\%$)	141
5.4 Conclusion	148
References	
Chapter 6 Summary and conclusions	152
Acknowledgement.....	158
List of publications	159

Chapter 1: Background and purpose

1.1. Introduction

Steels are widely used as important structure materials in many fields, such as vehicles (e.g., automobiles, ships), constructions (e.g., skyscraper, bridges) and infrastructures (e.g., pipeline, electric power plants, chemical plants). The type of steels employed depends on where it is used. Big ships are made by welding many plate steels, which are required to have a good welding ability. Steel bars used in skyscraper need to have a high strength to sustain.

Steels used in automobiles are required to have a good toughness for absorbing high energy to ensure passengers' safety when a collision takes place [1]. To manufacture a car body, the steels should have a good formability for realizing various shapes. Considering fuel efficiency, cars should reduce their weight to save fuel. However, steels used in an automobile accounts for more than 70% of the total weight of the car (**Fig. 1.1**)[2]. For reducing the car weight, using less amount of steel should be considered firstly. As a result, in order to keep the shape the automotive, steels used in cars need to reduce their thickness. Considering passenger safety, on the other hand, the steel parts should have enough thickness to absorb energy in collision. That is, two

demands described above (increasing fuel efficiency and increasing crash worthiness) give opposite requirements to the steels used in automotive. The way to satisfy both demands is to increase the strength of steels, maintaining formability (ductility) and toughness.

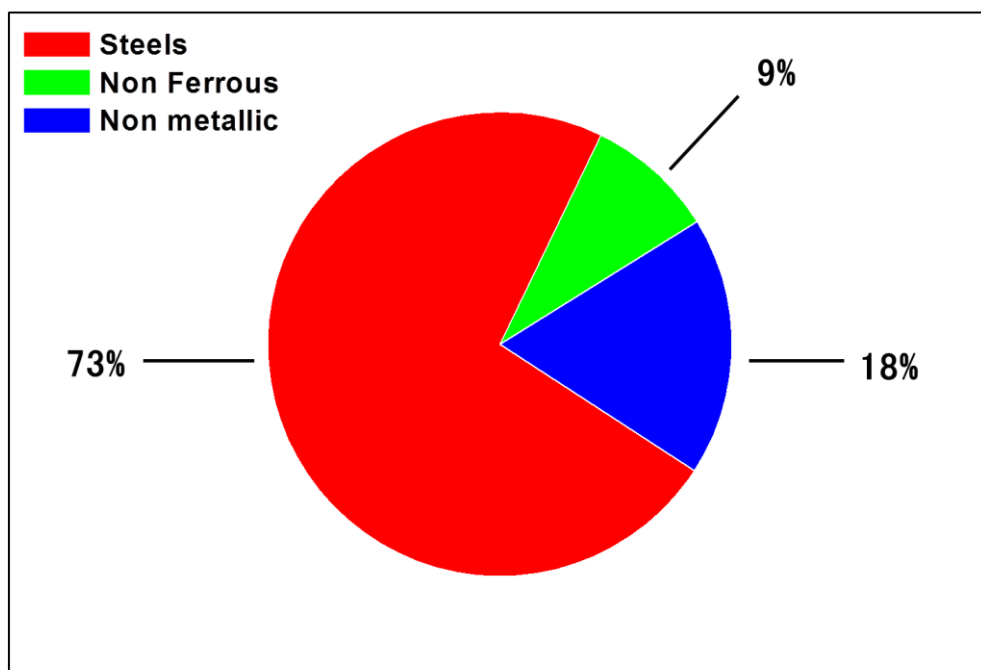


Fig. 1.1 Utilization ratio of body materials in an automobile[2].

However, the strength and ductility in steels are usually show tradeoff relationship. That is to say, with increasing the strength in steels, generally will decrease their ductility, and vice versa. For example, Figure 1.2 illustrates the relationship between strength and ductility in conventional steels. Interstitial free (IF) based steel shown in Fig. 1.2 show a large total elongation (ductility) but low tensile strength. On the

contrary, martensite steel exhibits a low elongation but high tensile strength.

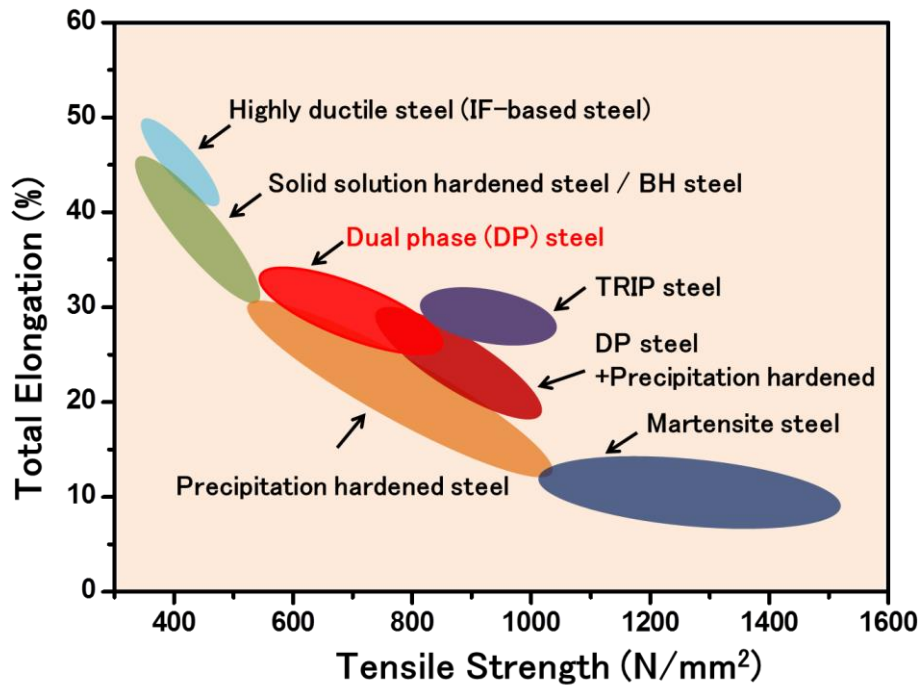


Fig. 1.2 Relationship between elongation and strength in steels[3].

Dual phase (DP) steels (red color in Fig. 1.2) consist of a hard martensite phase and a soft ferrite phase exhibit a good balance of strength and ductility, compared with other conventional steels. Large amount of DP steels have been used in automobile industry due to their good mechanical properties. To confront the continuous environment challenge, DP steels used in automotive required to continuous reducing their thickness in practice. It requires the steels continuous to increase their strength and ductility to meet the demand. Therefore, for designing higher strength and higher ductility steels,

it is necessary to understand the reason why DP steels combined high strength and formability (ductility) together. And understand the mechanical properties in DP steels can provide a new insight on designing both higher strength and higher ductility steels in the further.

1.2. Dual phase steels

As mentioned in section 1.2, DP steels are widely used in automotive applications because their good mechanical properties exhibit a good combination of high strength and formability. The good mechanical property of DP steels is due to their microstructure which consists of hard martensite phase and soft ferrite phase. Martensite phase and ferrite phase in DP steels can be produced by rapid quenching (e.g., Water quenching) from two-phase region (austenite and ferrite phases region) shown in Fig. 1.3. During the rapid quenching, austenite phase will transform to martensite phase results in volume change between austenite phase and martensite phase. The volume change will generate numerous of mobile dislocations distributed in martensite phase and ferrite phase [4]. Fig. 1.4 shows the scanning electron microscope (SEM) image and a comparison of stress-strain curves between DP steel and high strength low alloy (HSLA) steel and plain carbon steel. Fig. 1.4a shows the microstructures of martensite phase (uneven region with light gray) and ferrite phase (smooth region with dark gray) in DP steel. Fig. 1.4b shows the tensile properties of DP steel. Compared the tensile properties with HSLA alloy and plain carbon steel, DP steel shows low yield ratio (ratios of yield strength and tensile strength) and continuous

yielding during deformation (e.g., tensile test). In addition, DP steels show high work-hardening ability during deformation.

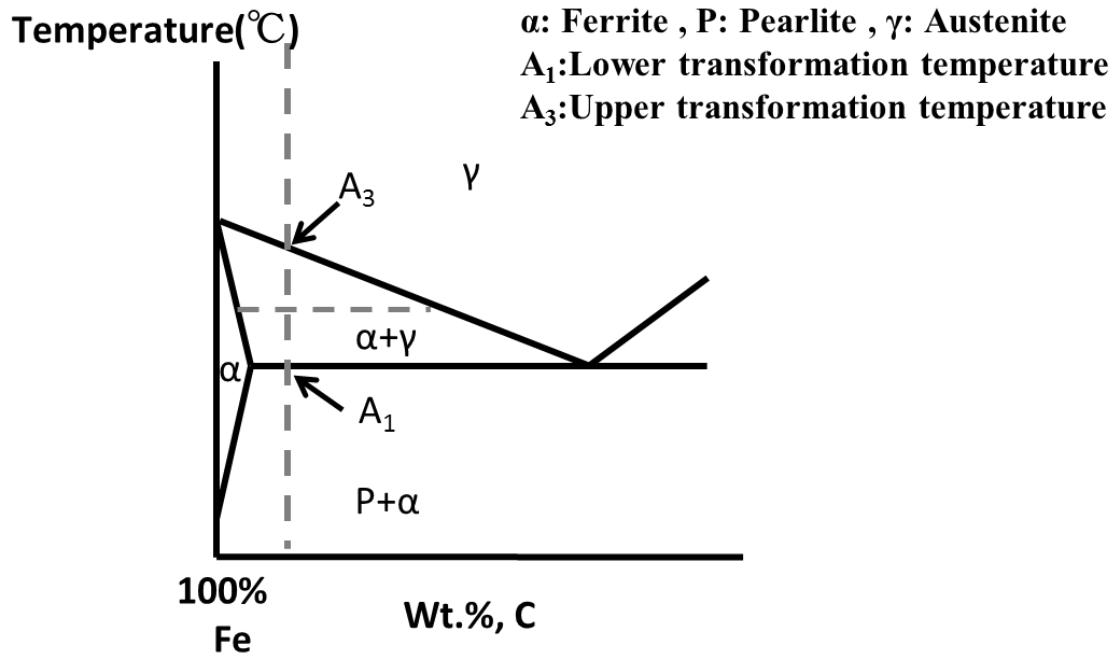


Fig. 1.3 Part of the equilibrium phase diagram for the Fe-C system.

In order to understand the mechanical properties of DP steels, many factors such as individual mechanical properties of martensite and ferrite, dislocation density in ferrite[6], grain size [7-10], texture[11, 12], volume fraction of martensite[13], martensite morphology[14] and martensite distribution [15-18] were investigated. The strength of DP steel can be increased by decreasing ferrite grain sizes [10] and increasing volume fraction of martensite. The uniform elongation can be improved by refining martensite phase [9] and changing the morphology of martensite and martensite

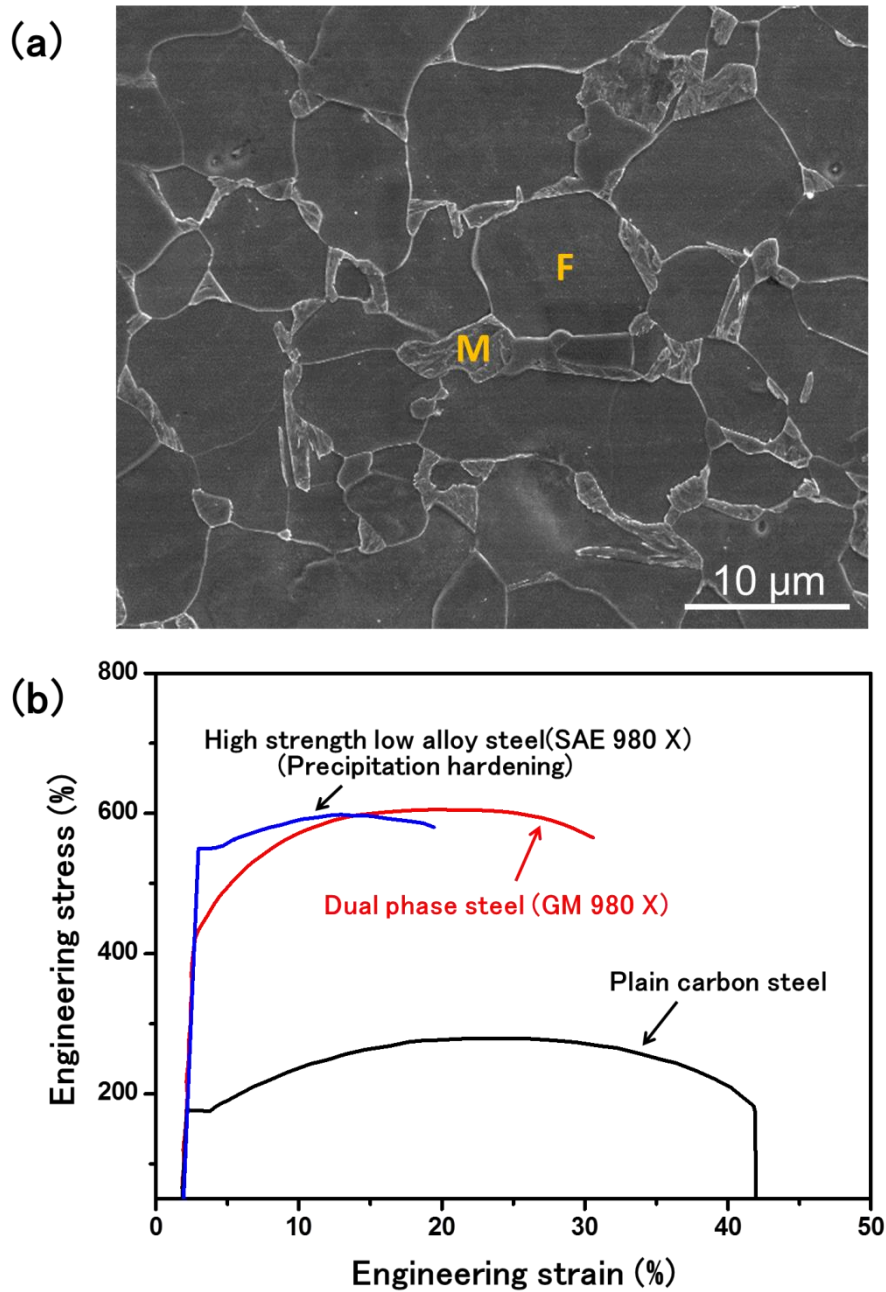


Fig. 1.4 Microstructure and mechanical properties of DP steel[5]. M: martensite phase; F: ferrite phase. (a) SEM image of DP steel showing martensite phase and ferrite phase structures. (b) stress-strain curves of DP steel, high strength low alloy steel (HSLA) and plain carbon steel.

For investigating individual mechanical properties of martensite and ferrite in DP steels, nanohardness of individual phases has been measured and the deformation responses of martensite and ferrite phases were estimated [20]. In addition, some models [21-24] based on simple composite materials in DP steels were used to predicting their mechanical properties. However, mechanical properties of DP steels with various volume fractions, sizes, and morphology of two phases would not apply to the models based on simple composite materials, because the interaction between ferrite phase and martensite phase also can affect the mechanical properties in plastic deformation. Therefore, In order to understand the good mechanical properties in DP steels, local deformation behaviors of interaction between ferrite and martensite should be considered.

1.3. Dual phase non-ferrous alloy

Dual phase non-ferrous alloy such as α - β brass contain soft α phase and hard β phase, which has a similar structure to ferrite and martensite DP steel. The factors studied in DP steels are also available for dual phase non-ferrous alloy. One reason for studying dual phase non-ferrous alloy is due to the beneficial for understanding the universal mechanical properties in DP alloys by studying the factors in DP steels and in dual phase non-ferrous alloys together. Another reason is because there is a disadvantage in experimental research to study the deformation behavior of martensite and ferrite phases in DP steels. In DP steels, martensite phase has a body-centered tetragonal (BCT) structure and ferrite phase has a body-centered cubic (BCC) structure. The difference between BCT structure and BCC structure are small in DP steels, especially carbon content in martensite phase less than 0.25wt. %. For studying the deformation behavior of individual phases, it is hard to distinguish martensite phase and ferrite phase by EBSD, XRD, etc. methods. It is because the similar phase structure between martensite phase and ferrite phase.

α - β brass is a kind of non-ferrous DP alloys having two different phase structures. α

phase has a face-centered cubic (FCC) structure and β phase has BCC structure. Due to the difference of phase structures, α phase and β phase can be distinguished by Optical Microscopy (OM), Electron Back-Scattered Diffraction (EBSD) and X-ray diffraction (XRD), etc. By studying the deformation behavior of α phase and β phase in α - β brass alloy, it is also benefit to understand the deformation behavior of phases in DP steels. This is the reason why dual phase non-ferrous alloy such as α - β brass is chosen to investigate in this study.

1.4. Objective of present study

DP steels having soft ferrite phase and hard martensite phase shows a good balance of strength and ductility. The special good mechanical properties, such as the high work-hardening rate, low yield ratio (ratios of yield strength and tensile strength) and continuous yielding, satisfied the development of automotive industry. However, why DP steel behaves such kind of good mechanical properties are still unclear. Previous studies shows factors such as dislocation density, grain size, texture, volume fraction of martensite, martensite morphology and martensite distribution, etc. can affect the mechanical properties of DP steels. However, the reason for DP steels combining both high strength and high ductility is still unclear. In the previous studies, some models based on simple composite materials have been proposed to predict the mechanical properties in DP steels. However, the interaction between ferrite phase and martensite phase will also affect the mechanical properties during plastic deformation. Therefore, for understanding the good mechanical properties of DP steels, deformation behavior of ferrite and martensite phases should be studied. However, in DP steels, martensite phase has a BCT structure which is similar to BCC structure in ferrite phase. It is hard to distinguish martensite phase and ferrite phase by experimental methods, such as

EBSD, XRD, etc., which makes study on deformation behavior of martensite phase and ferrite phase become difficult. However, non-ferrous alloys such as α - β brass having two different phase structures. It is easy to study the deformation behavior of individual phases by experimental methods. By studying the deformation behavior of individual phases in non-ferrous alloys is benefit to understand the deformation behavior in DP steels. Due to the reasons described above, we choose two kinds of materials, DP steel and α - β brass, to do research. It has been considered that hardness of martensite is the main factor contributing to the strength of DP steels. However, difference of hardness between martensite and ferrite phases could also be an important factor for the mechanical properties of DP steels. Based on the description above, the purposes of present study are listed as follows:

1. To investigate the change in mechanical properties of DP steel from a viewpoint of hardness difference between ferrite and martensite phases. The hardness ratio of martensite and ferrite phases (M/F) will be changed by tempering treatments.
2. To study the local deformation behavior of martensite phase and ferrite phase in DP steel with various hardness ratios between martensite phase and ferrite phase.
3. Comparison of the deformation behaviors in martensite based DP steel and ferrite based DP steel.

4. To clarify the deformation behavior of two phases with different microstructures in dual phase non-ferrous alloy, using Cu-Zn alloy in present study.

1.5. Experimental methods

1.5.1. Nanoindentation

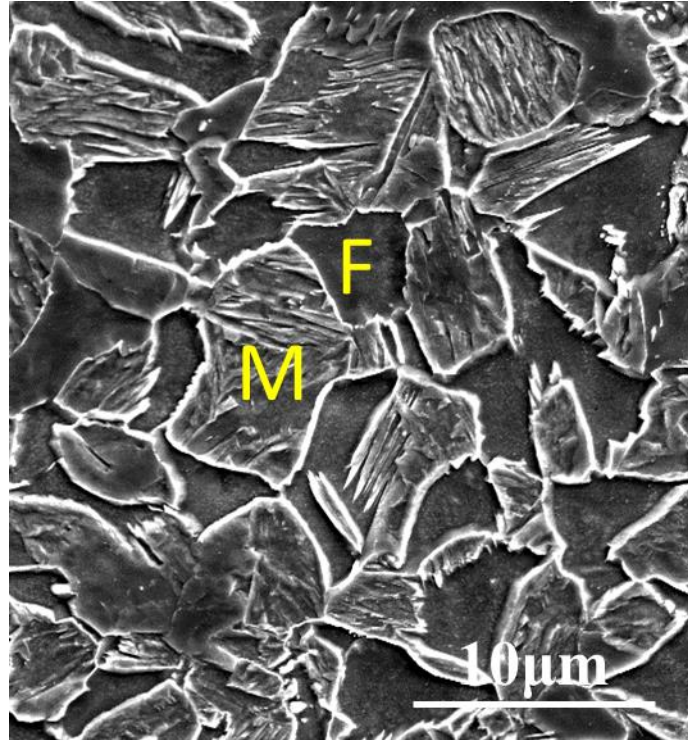


Fig. 1.5 SEM image shows the microstructure of DP steel.

Fig. 1.5 shows SEM image of one specimen in ferrite and martensite DP steel used in this study. Before taken SEM image, the specimen was electric polished and etched in 3% nital solution. In **Fig. 1.5**, the uneven region is martensite phase and smooth region is ferrite phase. Martensite phase was connected together and shown “net-work” microstructure. The average phase size of martensite and ferrite are 10 um and 5 um, respectively. Because the phase sizes of martensite and ferrite are too small, it is difficult to measure the microhardness by Vickers hardness test due to the large

indentation size. Therefore, in this study, we use Nanoindentation to measure nanohardness of martensite phase and ferrite phase in DP steel and α - β brass.

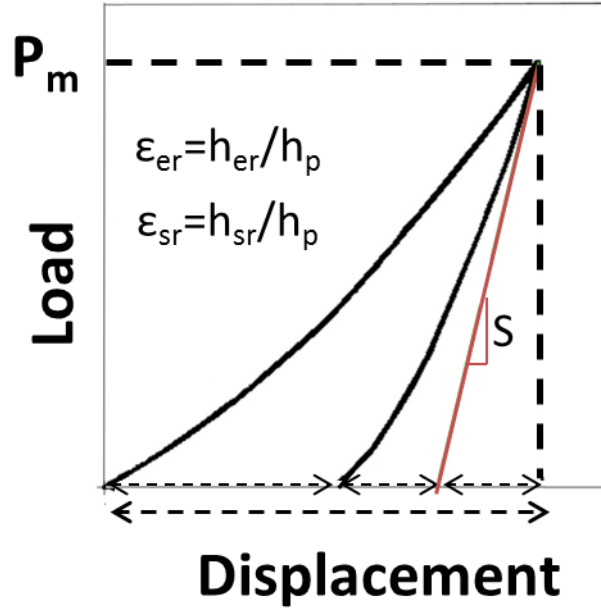


Fig. 1.6 Schematic illustration of nanoindentation load P–displacement h curve [25].

Fig. 1.6 shows schematic of Nanoindentation load P and displacement h curve. Nanohardness can be determined by equations shown below:

$$\epsilon_r = (h_p - h_r) / h_p \quad (1.1)$$

$$\epsilon_{sr} = (h_{sr} / h_p = h_p - h_r - P_m / S) / h_p \quad (1.2)$$

$$A = C_0 h c^2 + C_1 h c + C_2 h c^{1/2} + C_3 h c^{1/4} + C_4 h c^{1/8} + C_5 h c^{1/16} \quad (1.3)$$

$$h_c = h_p - \epsilon P_m / A \quad (1.4)$$

$$H = P_m / A \quad (1.5)$$

Where P_m is peak load, h_p is depth at peak load, h_{er} is elastic recovery displacement, h_{sr} is superelastic recovery displacement, h_r is residual displacement, S is initial unloading slope, ε_{er} and ε_{sr} is superelastic strain, ε is the geometric constant, H is nanoindentation hardness, A is the indentation area after nanoindentation.

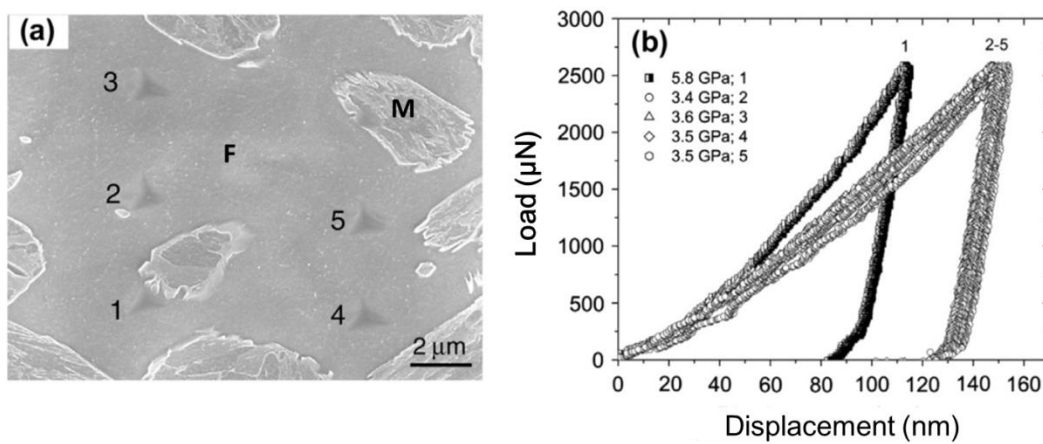


Fig. 1.7 (a) SEM image shows five nanoindentations in ferrite. (b) The corresponding load-displacement curves for the five nanoindentations[26].

Fig. 1.7 shows the example of nanoindentation test applied in ferrite phase. **Fig. 1.7(a)** is an SEM image after nanoindentation test. The indentation size is about 1μm, which is smaller than ferrite and martensite phase sizes. **Fig. 1.7(b)** is load-displacement curve for the indentations. The nanohardness of indentation 1 is near martensite phase showing a higher nanohardness value than indentation 2-5. For measuring the average nanohardness of martensite and ferrite phases, the nanohardness is measured within

martensite phase and ferrite phase region.

1.5.2 Digital image correlation (2D-DIC)

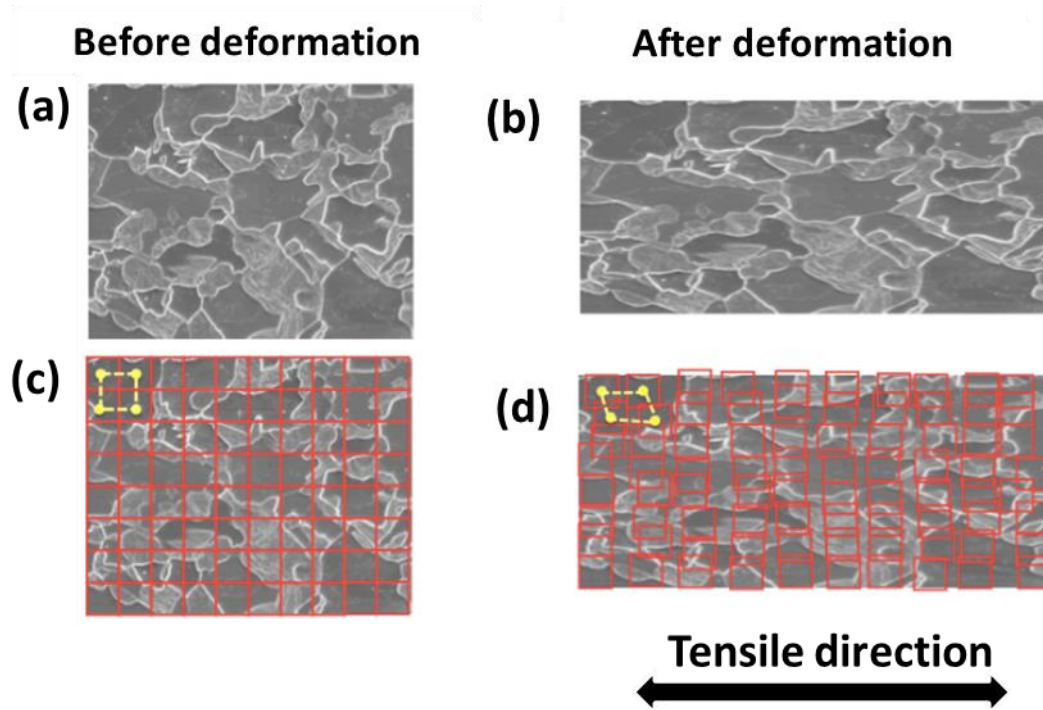


Fig. 1.8 Schematic illustration showing the measurement of digital image correlation method[27].

In this study, the strain partitioning in ferrite and martensite are analyzed by digital image correlation (DIC) method. Digital image correlation (DIC) method is an image analysis method based on track movement of local points by comparing two images of specimen before and after deformation. DIC method can apply optical and SEM images of DP steels to calculate the local displacements during tensile deformation. The measurement of DIC method is schematically illustrated in **Fig. 1.8**. For DIC method, square grids are set on the microstructure before deformation. The center

points in the squares are considered to represent the point of grads. The positions of the center points were determined by comparing the parameters of images, such as contrast and brightness.

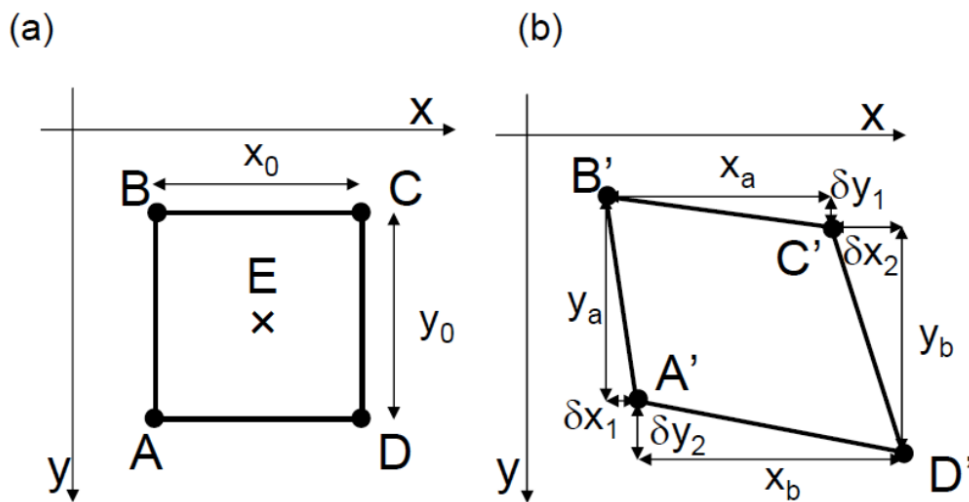


Fig. 1.9 Schematic illustrations showing displacements of the representative points in (a) undeformed and (b) deformed specimens for calculating local strains[27].

Fig. 1.9 shows the calculating local strains by tracing the displacements point. Four center points A, B, C, and D in the unreformed image was shown in **Fig. 1.9(a)**. Point E is supposed to be a fixed point before and after deformation. No position change in point E. After deformation, the points are moved to A', B', C' and D', respectively (**Fig. 1.9(b)**).

The strain can be calculated by the equations as below:

$$\varepsilon_{xx} = 1/2((x_a - x_0)/x_0 - (x_b - x_0)/x_0) \quad (1.6)$$

$$\varepsilon_{yy} = 1/2((y_a - y_0)/y_0 - (y_b - y_0)/y_0) \quad (1.7)$$

$$\varepsilon_{xy} = 1/2((\delta_{x1}/y_a + \delta_{y1}/x_a) + (\delta_{x2}/y_b + \delta_{y2}/x_b)) \quad (1.8)$$

$$\varepsilon_{eq} = (\{2/3 (\varepsilon_{xx}^2 + \varepsilon_{yy}^2) + 1/3 (\varepsilon_{xy}^2)\})^{1/2} \quad (1.9)$$

Where, x axis is parallel to the tensile direction, ε_{xx} is strain parallel to x axis, ε_{yy} is strain parallel to y axis, ε_{xy} is shear strain, ε_{eq} is equivalent strain.

1.5.3. In-situ neutron diffraction

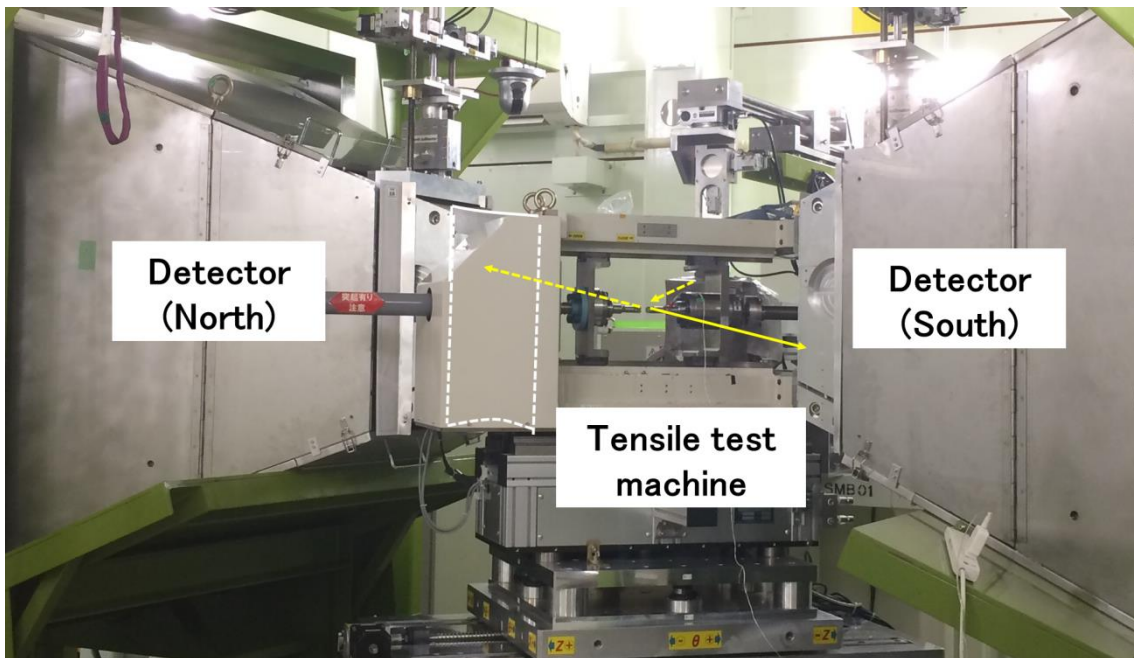


Fig. 1.10 Outlook of in situ-neutron diffraction machine at J-Parc.

In-situ neutron diffraction method can be used to measure the stress and strain partitioning in phases during tensile deformation [28]. In this study, we use In-situ

neutron diffraction method to study stress and strain partitioning on ferrite and martensite in DP steel and Cu-Zn alloy. In-situ neutron diffraction experiment was carried out in J-Parc (Japan Proton Accelerator Research Complex). **Fig. 1.10** and **Fig. 1.11** show the tensile test machine (TAKUMI instrument) used at J-Parc. The detectors in the north direction and south direction are measuring the results of specimen in transverse direction and tensile direction, respectively.

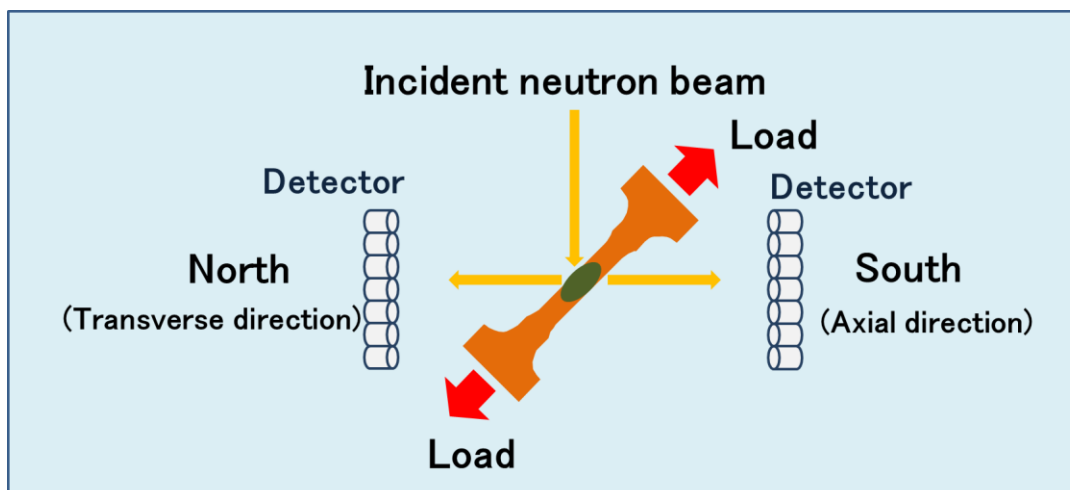


Fig. 1.11 Schematic illustrations the TAKUMI instrument on the beam line at J-Parc[29].

The lattice strain and the average phase strain can be obtained from the changes in lattice spacing and average lattice spacing. The calculation can be according to equations below [29]:

$$\varepsilon_{hkl}=(d_{hkl}-d_0)/d_0 \quad (1.10)$$

$$\varepsilon_{phase}=(a_{phase}-a_0)/a_0 \quad (1.11)$$

Where, ε_{hkl} is the lattice strain, ε_{phase} is the average phase strain, d_0 is particular lattice spacing, a_0 is lattice parameter in the stress-free specimen, d_{hkl} is lattice spacing of (hkl) plane, a_{phase} is average lattice spacing.

1.6. Outline of dissertation

The present dissertation contains six chapters. In **Chapter 1**, the background, purpose and experimental methods are introduced. In **Chapter 2**, martensite based DP steel is prepared, and the hardness ratio of martensite and ferrite phases (M/F) is changed by tempering treatments. The relationship between the mechanical properties of DP steel and M/F is revealed. In **Chapter 3**, Local deformation of martensite and ferrite phases are studied by DIC method and In-situ neutron diffraction in martensite based DP steels with different M/F. In **Chapter 4**, deformation behavior of ferrite based DP steels are compared with martensite based DP steels to clarify the martensite volume fraction effects. In **Chapter 5**, for better understand the deformation behavior of two phases during tensile deformation, Cu-Zn alloy, as dual phase non-ferrous alloys, is chosen to study due to the phases structure in Cu-Zn alloys are different. **Chapter 6** is summary and conclusions of present dissertation.

Reference

- [1] R. Kuziak, R. Kawalla, S. Waengler, *Arch Civ Mech Eng*, 8 (2008) 103-117.
- [2] Y. Azuma, TMS International Symposium on Niobium Microalloyed Sheet Steel for Automotive Application 2006, (2006) 8.
- [3] H. Takechi, *JOM*, 60 (2008) 22-26.
- [4] T. Sakaki, K. Sugimoto, T. Fukuzato, *Acta Metallurgica*, 31 (1983) 1737-1746.
- [5] M. Rashid, SAE Technical Paper, 1977.
- [6] M. Calcagnotto, D. Ponge, E. Demir, D. Raabe, *Mat Sci Eng a-Struct*, 527 (2010) 2738-2746.
- [7] Y.-l. Kang, Q.-h. Han, X.-m. Zhao, M.-h. Cai, *Mater Design*, 44 (2013) 331-339.
- [8] M. Calcagnotto, Y. Adachi, D. Ponge, D. Raabe, *Acta Mater*, 59 (2011) 658-670.
- [9] N. Saeidi, F. Ashrafizadeh, B. Niroumand, *Mat Sci Eng a-Struct*, 599 (2014) 145-149.
- [10] Y. Mazaheri, A. Kermanpur, A. Najafizadeh, *Isij Int*, 55 (2015) 218-226.
- [11] S.H. Choi, E.Y. Kim, W. Woo, S.H. Han, J.H. Kwak, *Int J Plasticity*, 45 (2013) 85-102.
- [12] D.H. Kim, S.-J. Kim, S.-H. Kim, A.D. Rollett, K.H. Oh, H.N. Han, *Acta Mater*, 59 (2011) 5462-5471.
- [13] M.R. Akbarpour, A. Ekrami, *Mat Sci Eng a-Struct*, 477 (2008) 306-310.
- [14] Q. Han, Y. Kang, P.D. Hodgson, N. Stanford, *Scripta Mater*, 69 (2013) 13-16.
- [15] S.R. Mediratta, V. Ramaswamy, *Jom-J Min Met Mat S*, 36 (1984) 35-35.
- [16] G. Avramovic-Cingara, Y. Ososkov, M.K. Jain, D.S. Wilkinson, *Mat Sci Eng a-Struct*, 516 (2009) 7-16.
- [17] C. Thomser, V. Uthaisangsuk, W. Bleck, *Steel Res Int*, 80 (2009) 582-587.
- [18] K. Park, M. Nishiyama, N. Nakada, T. Tsuchiyama, S. Takaki, *Mat Sci Eng a-Struct*, 604 (2014) 135-141.
- [19] A.P. Pierman, O. Bouaziz, T. Pardoën, P.J. Jacques, L. Brassart, *Acta Mater*, 73 (2014) 298-311.
- [20] P. Chen, H. Ghassemi-Armaki, S. Kumar, A. Bower, S. Bhat, S. Sadagopan, *Acta Mater*, 65 (2014) 133-149.
- [21] J.Y. Koo, M.J. Young, G. Thomas, *Metall Trans A*, 11 (1980) 852-854.
- [22] S. Kuang, Y.L. Kang, H. Yu, R.D. Liu, *Int J Min Met Mater*, 16 (2009) 393-398.
- [23] E. Ahmad, *J Mater Eng Perform*, 22 (2013) 2161-2167.
- [24] E. Fereiduni, S.S.G. Banadkouki, *J Alloy Compd*, 577 (2013) 351-359.
- [25] R.D. Dar, Y. Chen, *Acta Mater*, 91 (2015) 112-127.

- [26] H. Ghassemi-Armaki, R. Maaß, S.P. Bhat, S. Sriram, J.R. Greer, K.S. Kumar, *Acta Mater*, 62 (2014) 197-211.
- [27] T. Daisuke, M. Wadamori, Nobuhiro, Tsuji, *Symposium on New Developments in AHSS*, (2013).
- [28] S. Morooka, Y. Tomota, T. Kamiyama, *Isij Int*, 48 (2008) 525-530.
- [29] S. Morooka, N. Sato, M. Ojima, S. Harjo, Y. Adachi, Y. Tomota, O. Umezawa, (2011).

Chapter 2: Influence of tempering on mechanical properties and microstructure in dual phase steel composed of ferrite and martensite

2.1. Introduction

As mentioned in **Chapter 1**, ferrite and martensite dual phase (DP) steels composed of soft ferrite phase and hard martensite phase usually show a good balance of high strength and good ductility [1]. Due to the good combination of strength and ductility, DP steels are widely used in practical applications, especially in automotive-related fields [2-5]. In addition, compared with other conventional high strength steels, DP steels satisfy some special properties required for good formability, such as high work-hardening rate, low yield ratio (ratios of yield strength and tensile strength), and continuous yielding [6-12]. In order to clarify the origin of the superior mechanical properties in DP steels, several factors such as grain sizes [13-22], volume fraction of phases [23-32], constituent phases morphology [24, 28, 30, 33-35] and constituent phases properties [36, 37] have been investigated. Peng-Heng and Preban [38] found that yield ratio decreased with increasing ferrite grain size and the ratio kept a constant value after reaching a certain ferrite grain size. Saeidi. al. et [14] found that uniform

and total elongation values were affected by refining martensite particles. The higher ductility of ultrafine grained DP microstructure specimen was due to the higher plasticity of fine martensite particles which resulted in higher strain hardenability. Mohammad. al. et[25] showed that the limiting strains decrease by increasing the amount of martensite volume fractions. Zhang al.et [24] studied two different morphologies of martensite in DP steel. Their results showed fibrous martensite in DP steel resulted in less strain hardening than blocky martensite, before over a threshold volume fraction. And the threshold value was smaller in DP steel having blocky martensite. Azuma. al.et[37] studied the influence of the hardness of martensite and ferrite phases in dual phase steel on void formation by in situ tensile loading in a scanning electron microscope. Their results showed that reducing the hardness difference between martensite and ferrite phases by tempering was an effective approach to retard the void formation in martensite. It has been considered that hardness of martensite phase is the main factor contributing to the strength of DP steels. However, difference of hardness between martensite and ferrite phases could also be an important factor for the mechanical properties of DP steels.

Recently, Nanoindentation technique was used to measure the nanohardness of constituent phases in DP steels [39-44]. Several studies [42, 45] reported that

tempering decreased the nanohardness of martensite phase. Azuma et al. [37] found that the nanohardness of ferrite phase also decreased by tempering. However, Hayashi et al. [45] reported that tempering did not change the nanohardness of ferrite phase. Therefore, the objective of **Chapter 2** is to investigate the change in mechanical properties of DP steel from a viewpoint of hardness difference between ferrite and martensite phases. The hardness ratio of two phases was changed by intercritical annealing and tempering treatments.

2.2. Experimental procedure

In this study, chemical composition of the steel is presented in **Table 2.1**. A_1 (lower critical temperature for ferrite) and A_3 (upper critical temperature for ferrite) temperatures were calculated to be 696 and 885 °C, respectively, using a thermodynamics calculation software Thermo-Calc.

Table 2.1 Chemical composition of the investigated steel (wt. %).

Element	C	Si	Mn	P	S	Fe
Composition	0.08	0.75	1.74	0.008	0.003	Bal.

The heat treatment process used in this study is shown in **Fig. 2.1**. A sheet 1 mm thick of the steel was homogenized at 950 °C (above A_3 temperature) for 1.8 ks, followed by air cooling to obtain a microstructure composed of ferrite and pearlite. The sheet was then intercritically annealed at 840 °C (ferrite + austenite region) followed by water quenching to obtain a DP structure composed of martensite and ferrite, and then tempered at various temperatures ranging from 200 to 600 °C for 3.6 ks to change hardness of martensite and ferrite phases. All the heat treatments were carried out by a salt bath furnace.

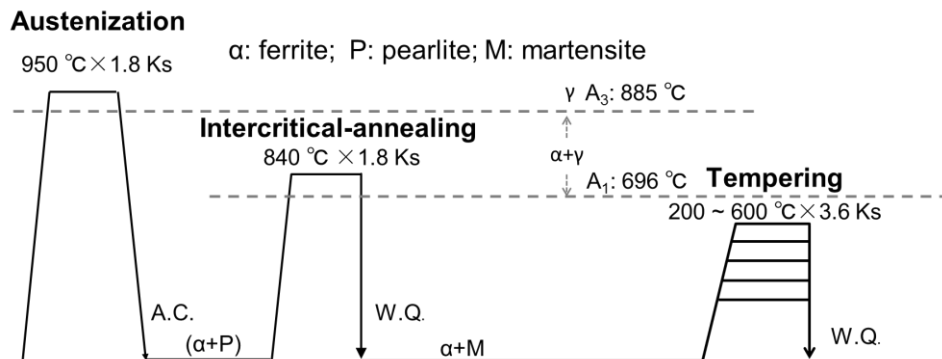


Fig. 2.1 Schematic illustration of the heat treatment process used in this study.

The microstructures of the specimens were observed by scanning electron microscopy (SEM, Jeol: JSM7800F). For the microstructure observations, the specimens were polished mechanically by emery papers and then electrochemically in a 10 % perchloric acid solution (100 ml $HClO_4$ + 900 ml CH_3COOH). The polished surfaces were etched

in a 3 % nital solution to distinguish martensite and ferrite phases. The volume fraction of martensite was measured by calculating the martensite area from low magnification (500X) SEM images. Tensile tests at an initial strain rate of $8.3 \times 10^{-4} \text{ s}^{-1}$ were conducted at room temperature. Tensile test specimens with a gauge length of 10 mm, width of 5 mm, and thickness of 1 mm were prepared from the heat-treated specimens by spark-cutting. Extensometer was used to measure tensile strain of the specimens. The extensometer was removed after the specimen was necked. The part of stress-strain curve after specimen necking was estimated by the crosshead travel. Nanohardness of the specimens were also measured by Nanoindentation test machine (Hysitron: TI 950 TriboIndenter) with a Berkovich indenter. The loading rate was $50 \mu\text{N s}^{-1}$, and the maximum load was 500 N. The nanohardness of martensite and ferrite phases were obtained within martensite and ferrite phase region, and the obtained values were averaged.

2.3 Effect of tempering temperature on microstructure evolution

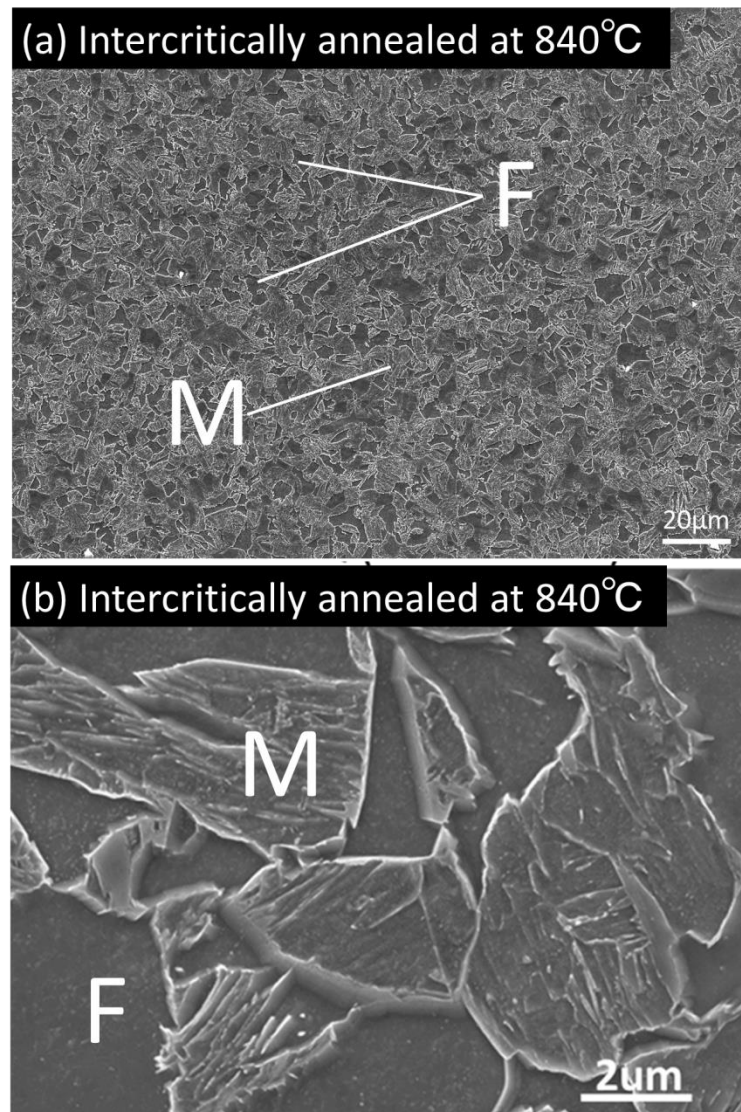


Fig. 2.2 SEM images showing microstructures of the specimens intercritically annealed at 840 °C.

Fig. 2.2 shows the SEM microstructures of the specimen intercritically annealed at 840 °C. Before SEM observation, the specimen was etched in a 3 % nital solution.

Under the SEM observation, specimen reveals net-work connected martensite and isolated ferrite structure (**Fig. 2.2a**). Ferrite phase shows a dark color and smooth surface, on the contrary martensite phase shows a relatively bright color and uneven surface (**Fig. 2.2b**).

The volume fraction of martensite was 80% measured by calculating the martensite area using low magnification (500X) SEM images. The morphology of net-work connected martensite and the volume fraction of martensite were decided by isothermal intercritical annealing condition and intercritical annealing temperature.

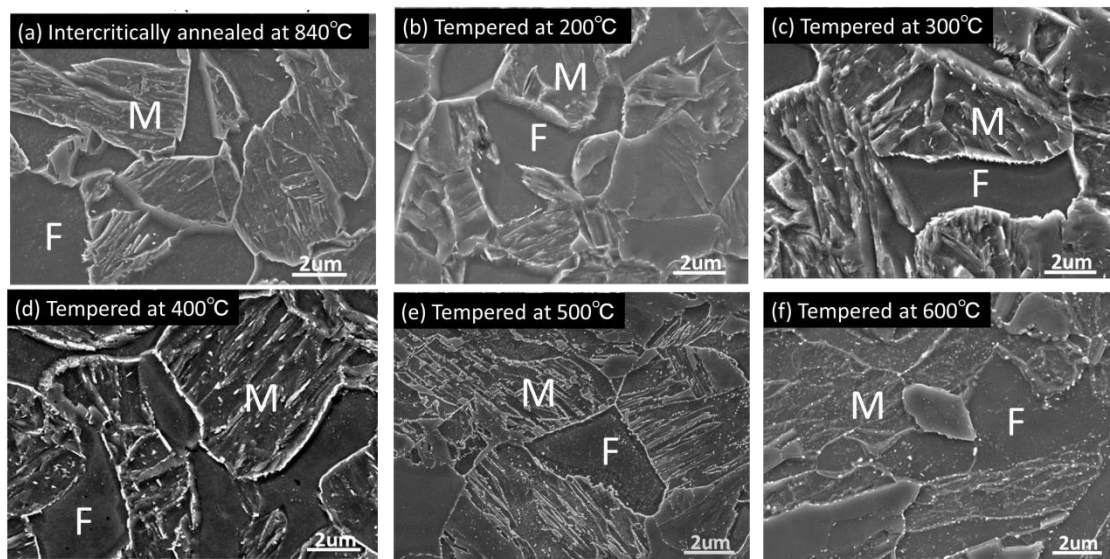


Fig. 2.3 SEM images showing microstructures of the specimens intercritically annealed at 840 °C and subsequently tempered at various temperatures for 3.6 Ks: (a) as intercritically annealed, (b) tempered at 200 °C, (c) tempered at 300 °C, (d) tempered at 400 °C, (e) tempered at 500 °C and (f) tempered at 600 °C. (F, ferrite; M, martensite).

Fig. 2.3 shows SEM images of the specimens intercritically annealed at 840 °C (a) and

subsequently tempered at 200 °C (b), 300 °C (c), 400 °C (d), 500 °C (e) and 600 °C (f) for 3.6 ks, respectively. The uneven and smooth regions in the SEM images correspond to martensite and ferrite phases, respectively. The interphase boundaries are clear to be seen in specimen (Fig. 2.3a) before tempering. And the interphase boundaries can be easy to distinguish in tempered specimens (Fig. 2.3 (b-e)). When the specimen was tempered at 600 °C (Fig. 2.3f), the interphase boundaries became unclear, but the martensite phase region and ferrite phase region were still can be distinguished from SEM image.

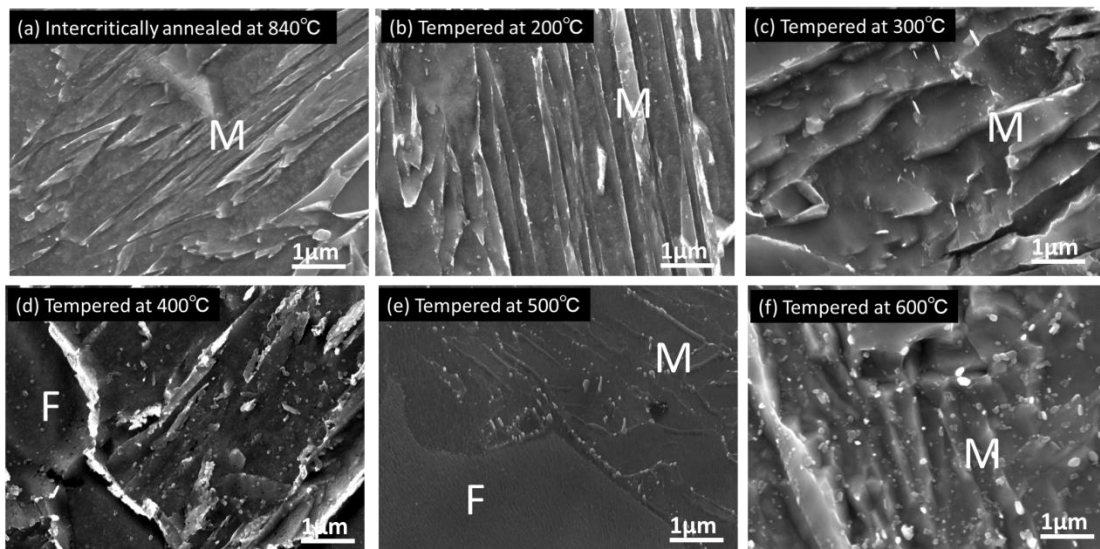


Fig. 2.4 High magnification SEM images showing microstructures of the specimens intercritically annealed at 840 °C and subsequently tempered at various temperatures for 3.6 Ks: (a) as intercritically annealed, (b) tempered at 200 °C, (c) tempered at 300 °C, (d) tempered at 400 °C, (e) tempered at 500 °C and (f) tempered at 600 °C. (F, ferrite; M , martensite).

Fig. 2.4 shows the high magnification SEM images of specimens to observe the microstructure changes before and after tempering at 200 °C to 600 °C. The microstructure of the specimen tempered at 200 °C (**Fig. 2.4b**) was similar to that of the intercritically annealed specimen (**Fig. 2.4a**). But the specimen tempered at 200 °C (**Fig. 2.4b**) show more fine iron carbide appear in martensite substructure compared with the intercritically annealed specimen (**Fig. 2.4a**). As the specimen tempered at 300 °C, iron carbide shows a microstructure as a distribution of rods in martensite substructure (**Fig. 2.4c**). With increasing the tempering temperature (**Fig. 2.4(d-f)**), more carbides precipitated and carbide sizes increased and change their crystallographic morphology to be spheroidized.

Fig. 2.5 shows TEM microstructures of the specimens intercritically annealed at 840 °C (a) and subsequently tempered at 400 °C (**Fig. 2.5b, Fig. 2.5d**), 600 °C (**Fig. 2.5c, Fig. 2.5e**). **Fig. 2.5a** shows lath martensite structure with high density of dislocations. However, martensite lath structure became coarser with reduction of dislocation when specimens tempered at 400 °C (**Fig. 2.5b**) and 600 °C (**Fig. 2.5c**). It is expected that recovery and recrystallization of martensite appear at higher tempering temperatures. After tilting zone axis, the change of iron carbide during tempering could be observed in

Figs. 2.5(d-e). With increasing the tempering temperature (**Fig. 5e**), more carbides precipitated and carbide sizes increased and their crystallographic morphology tend to be spheroidized. Ferrite phase is surrounded by tempered martensite (**Fig. 2.5e**). The spheroid iron carbides are located mainly at interlath boundaries and interphase boundary between martensite phase and ferrite phase.

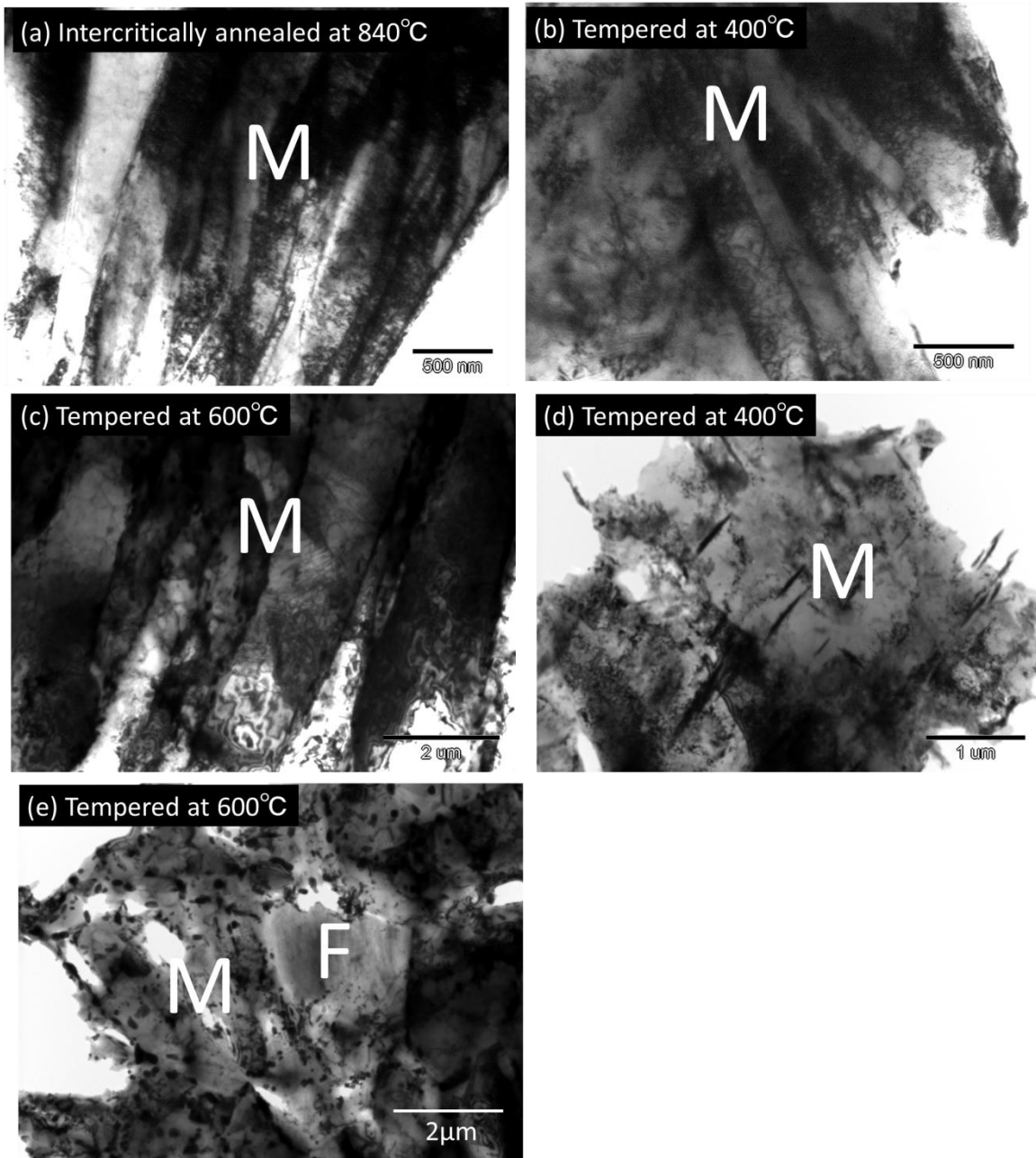


Fig. 2.5 shows TEM microstructures of the specimens intercritically annealed at 840 °C (a) and subsequently tempered at 400 °C (b,d), 600 °C (c,e-f).

2.4. Effect of tempering temperature on mechanical properties

2.4.1. Nanohardness change of martensite and ferrite phases

Fig. 2.6 shows tempering temperature as a function of (**Fig. 2.6a**) nanohardness values of martensite and ferrite and (**Fig. 2.6b**) nanohardness ratio between martensite and ferrite.

The nanohardness values of martensite and ferrite are shown in **Fig. 2.6a**. The scattering of hardness in martensite is basically larger than that in ferrite. This is possibly because several boundaries inside the martensite structure, such as lath boundaries, block boundaries, and packet boundaries, could affect the nanohardness of martensite measured within a small volume. It is found from **Fig. 2.6a** that the nanohardness of both martensite and ferrite decreased with increasing the tempering temperature. In addition, the difference in nanohardness between martensite and ferrite decreased with increasing temperature. The nanohardness of martensite became similar to that of ferrite after the specimen tempered at 600 °C. The ratio of nanohardness between martensite and ferrite (M/F) is plotted in **Fig. 2.6b** as a function of the tempering temperature. The nanohardness ratio was decreased with increasing tempering temperature.

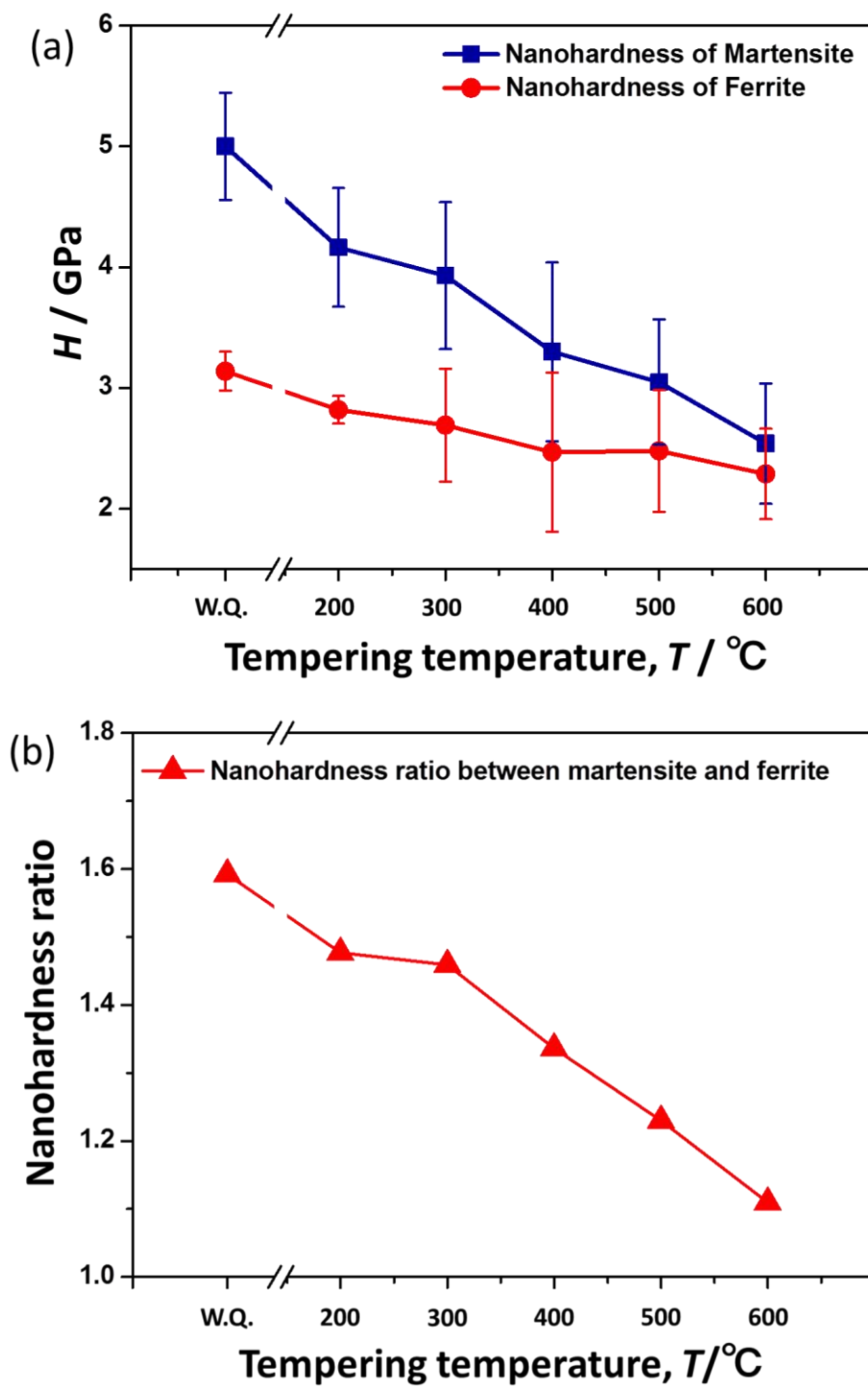


Fig. 2.6 Tempering temperature as a function of (a) nanohardness values of martensite and ferrite and (b) nanohardness ratio between martensite and ferrite

2.4.2. Stress-strain behaviors

Fig. 2.7a shows the nominal stress-strain curves for the specimen intercritically annealed at 840 °C and subsequently tempered from 200 to 600 °C. The yield stress (0.2% proof stress), ultimate tensile strength, uniform elongation and total elongation are determined from stress-strain curves. From the stress-strain curve, the tensile strength was decreased with increasing tempering temperature. However, the total elongation was increased with increasing tempering temperature. **Fig. 2.7b** is the enlarge image of **Fig. 2.7a**. **Fig. 2.7b** shows that the yielding behavior changed from continuous yielding to discontinuous yielding after tempering. In addition, with increasing tempering temperature, the Lüders elongation increased and the specimen showed more obvious of yield drop. It is expected that the carbide precipitation pinned the mobile dislocation and cause the discontinuous yielding.

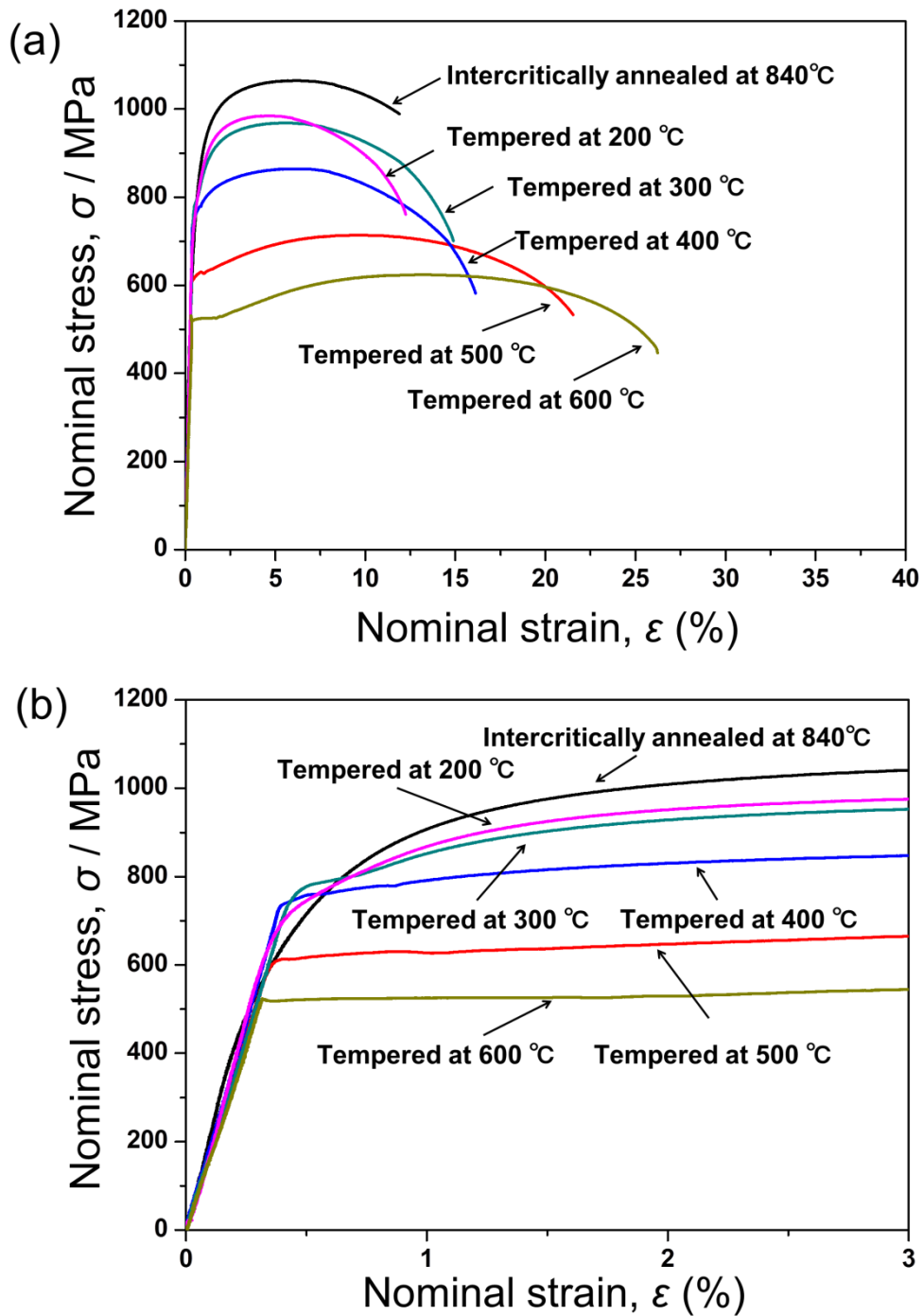


Fig. 2.7 Nominal stress-strain curves of (a) Intercritically annealed specimen and tempered at 200-600 °C specimens and (b) enlarged figure at early stages of nominal stress-strain curves.

2.4.3. Effect of tempering temperature on strength and elongation

Fig. 2.8a summarizes the change of strength (0.2% proof stress and ultimate tensile strength) as a function of tempering temperature. It is found that the ultimate tensile strength monotonously decreased with increasing the tempering temperature. On the other hand, the 0.2% proof stress firstly increased a little bit by tempering at temperatures below 300 °C, and then decreased above 300 °C. The increase of 0.2% proof stress by tempering at temperatures below 300 °C is presumably because precipitated carbides pinned mobile dislocations in martensite phase. After further tempering above 300 °C, the coarsening of carbides and martensite led to the decrease of 0.2% proof stress.

Fig. 2.8b shows the change of elongation, i.e., uniform elongation and total elongation, as a function of tempering temperature. With increasing the tempering temperature, the total elongation monotonously increased. On the other hand, the uniform elongation did not change so much after tempering at temperature below 400 °C, while it quickly increased above 400 °C.

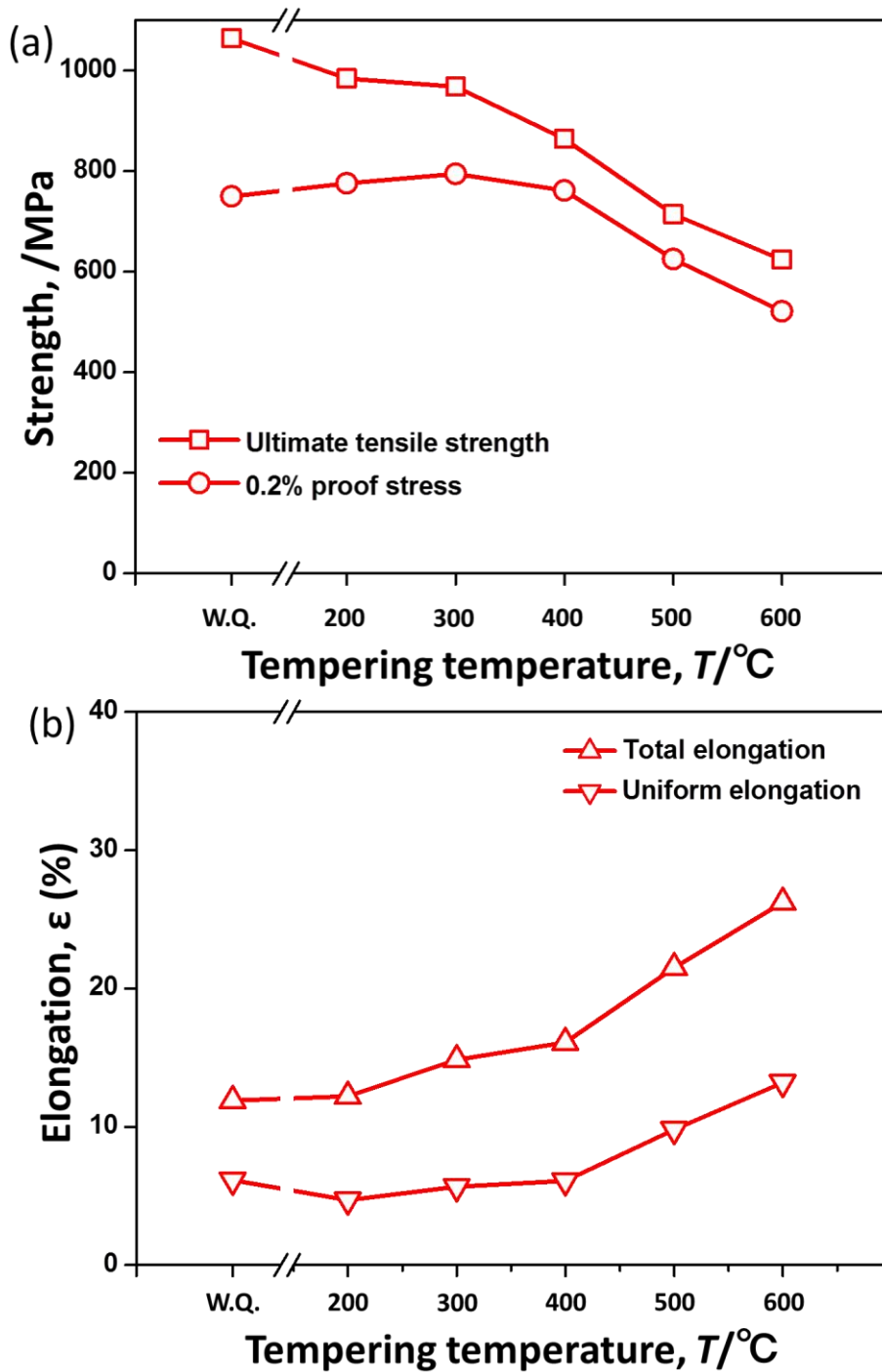


Fig. 2.8 The strength and elongation plotted as a function of tempering temperature. (a) 0.2% proof stress and ultimate tensile strength plotted as a function of tempering temperature. (b) Uniform elongation and total elongation plotted as a function of tempering temperature.

2.4.4. Relationship between strength-elongation and nanohardness ratio of martensite to ferrite

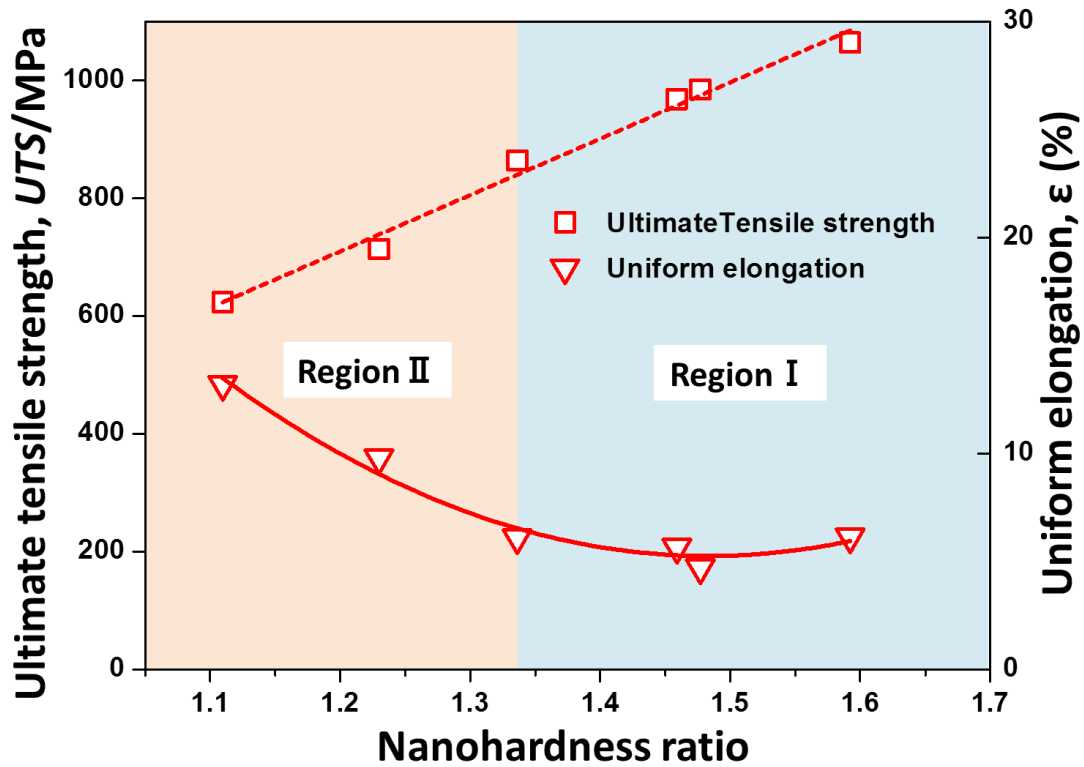


Fig. 2.9 Ultimate tensile strength and uniform elongation in the DP steel summarized as a function of the nanohardness ratio.

The ultimate tensile strength and uniform elongation are plotted in **Fig. 2.9** as a function of the ratio of nanohardness between martensite and ferrite (M/F). The ultimate tensile strength has a linear-like relationship with the nanohardness ratio and decreased monotonously with decreasing the nanohardness ratio. The change of uniform elongation can be divided into two regions (I and II in **Fig. 2.9b**). In the region I (M/F

< 1.34), the uniform elongation increased with decreasing the nanohardness ratio. In contrast, the uniform elongation was nearly independent of the nanohardness ratio in the region II ($M/F > 1.34$).

2.5. Discussion

The strength and ductility of the ferrite and martensite DP steel was investigated in this study as a function of nanohardness ratio between martensite and ferrite. The specimens with various hardness ratios were successfully prepared through intercritical annealing and sequent tempering process.

The very high hardness of martensite phase in ferrite and martensite DP steels is due to three aspects. One is because martensite with carbon atoms has a tetragonal structure, the distortion of the iron lattice lead dislocation movement to be difficult. Second is due to the solid solution strengthening by carbon atoms. Third is lath martensite structure contain high density of dislocations obtained from martensite transformation is also contributes to the high strength.

Fig. 2.6a shows both the nanohardness of martensite phase and ferrite phase decreased by tempering. The reasons are as follows. Martensite could reject carbon to form iron carbide phases during tempering. Reducing carbon content in martensite is one

reason for decreasing the hardness of lath martensite [46]. In addition, tempering decreases the mobile dislocation density by dislocation recovery and coarsening fine lath martensite structure by carbon diffusion [47], which also decrease the nanohardness of martensite. Recovery and recrystallization might be happen in martensite also decreasing the nanohardness of martensite. And also the martensite decomposition to ferrite and carbide will also decrease the nanohardness of martensite. Dislocations were also generated in ferrite phase due to the volume change of martensite phase during martensite transformation. During tempering, recovery of dislocation in ferrite phase will decrease the hardness of ferrite phase.

2.5.1. Mixture rule

In this study, we estimate the average microhardness of DP steel by a simple mixture rule rewritten as following equation [48-50],

$$H_{avg}=H_m V_m+H_f (1-V_m) \quad (2.1)$$

Where H_{avg} is the average hardness of DP steel, and H_m and H_f are the nanohardness of martensite and ferrite, respectively. V_m is the volume fraction of martensite.

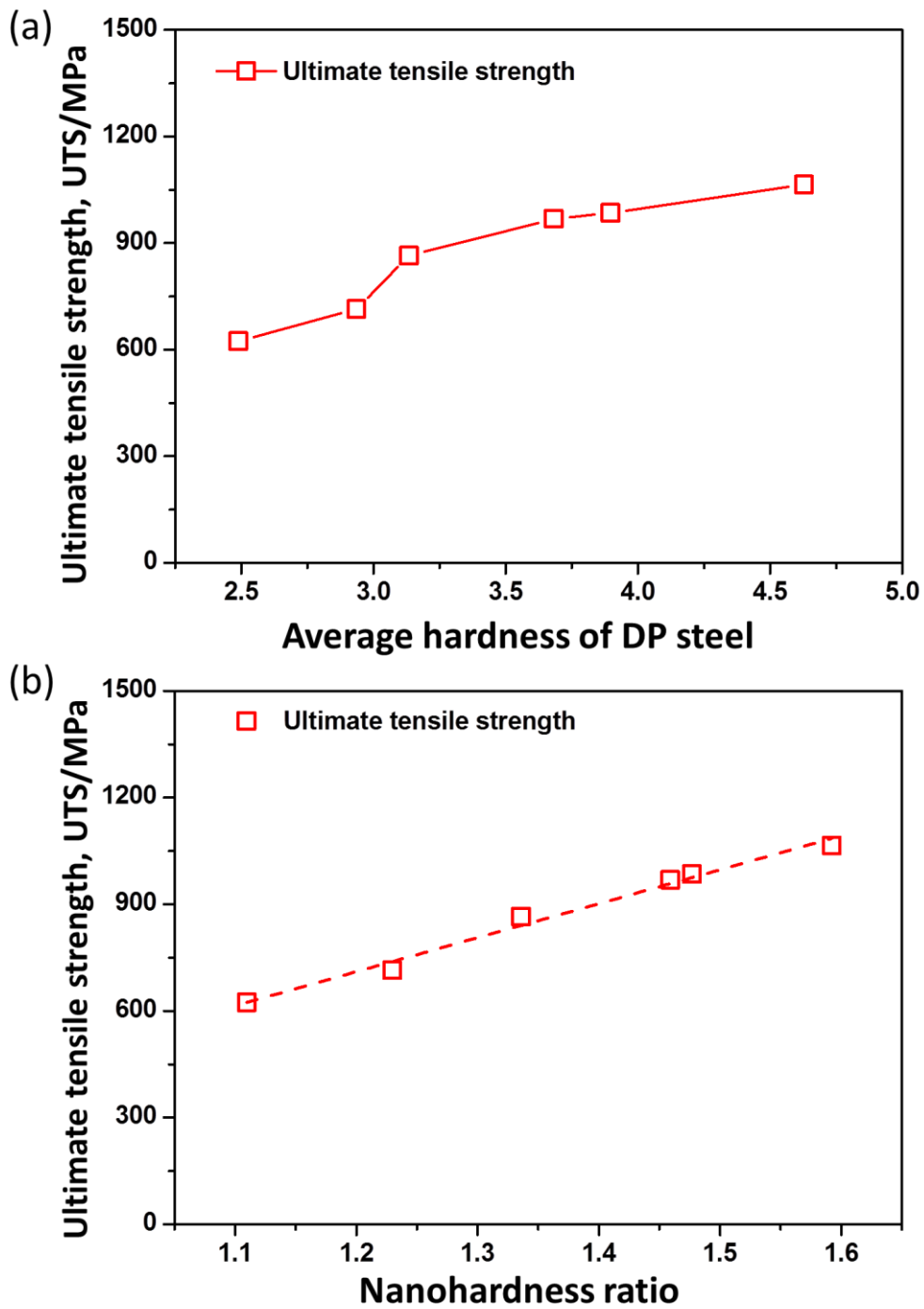


Fig. 2.10 Ultimate tensile strength as a function of (a) average hardness of DP steel, and (b) nanohardness ratio.

According to Eq (2.1), the ultimate tensile strength was plotted as a function of average

hardness of DP steel in **Fig. 2.10a**. **Figure 2.10b** shows the relation of ultimate tensile strength as a function of nanohardness ratio. The dotted line is linear fitting curve. Compared with the **Fig 2.10a**, nanohardness ratio in **Fig. 2.10b** shows a more linear relationship with ultimate tensile strength. It may be because martensite and ferrite have different properties deforms differently in DP steels during deformation. The difference of their mechanical properties results in additional interaction stress and strain. The interaction between martensite and ferrite phases might be the reason why the relationship of ultimate tensile strength and average hardness of DP steel were not linear.

2.5.2. Work-hardening behavior

As described in **Fig. 2.9**, the change of uniform elongation can be divided into two regions (I and II in **Fig. 2.9**). In the region I ($M/F < 1.34$), the uniform elongation increased with decreasing the nanohardness ratio. In contrast, the uniform elongation was nearly independent of the nanohardness ratio in the region II ($M/F > 1.34$). In the region I ($M/F < 1.34$), increasing the nanohardness ratio of DP specimens lead to higher tensile strength, but the uniform elongation are almost constant , which indicated the specimens increased their work-hardening ability. During the tensile test, the applied

load has to increase due to the work hardening of the specimen. The competition between work hardening ability and the loading capacity decide the stability of the specimen. When the work hardening ability of the specimen was less than the loading capacity, the specimen becomes instability. Plastic instability appears in DP specimens indicated necking take place in tensile deformation.

The plastic instability can be expressed by the Considère criterion [51]:

$$\frac{d\sigma}{d\varepsilon} \leq \sigma \quad (2.2)$$

where σ and ε are the true stress and true strain, respectively, and $d\sigma/d\varepsilon$ is the work hardening rate. When the equation is satisfied (work hardening rate became smaller than true stress), necking takes place and uniform elongation can be determined.

Fig. 2.11 shows the work hardening rate curves of the specimens in region I (a) and in region II (b). The true stress-strain curves were transformed from the nominal stress-strain curves, and the work hardening rate curves were obtained by differentiating the true stress with respect to the true strain. For one specimen, the same color was used in the work hardening rate curve (dot) and true stress-strain curve (solid). The intersections of the work hardening rate curve and the true stress-strain curve are marked in big dot correspond to the uniform elongation of the specimen, which satisfied Considère criterion indicate the plastic instability of the specimen.

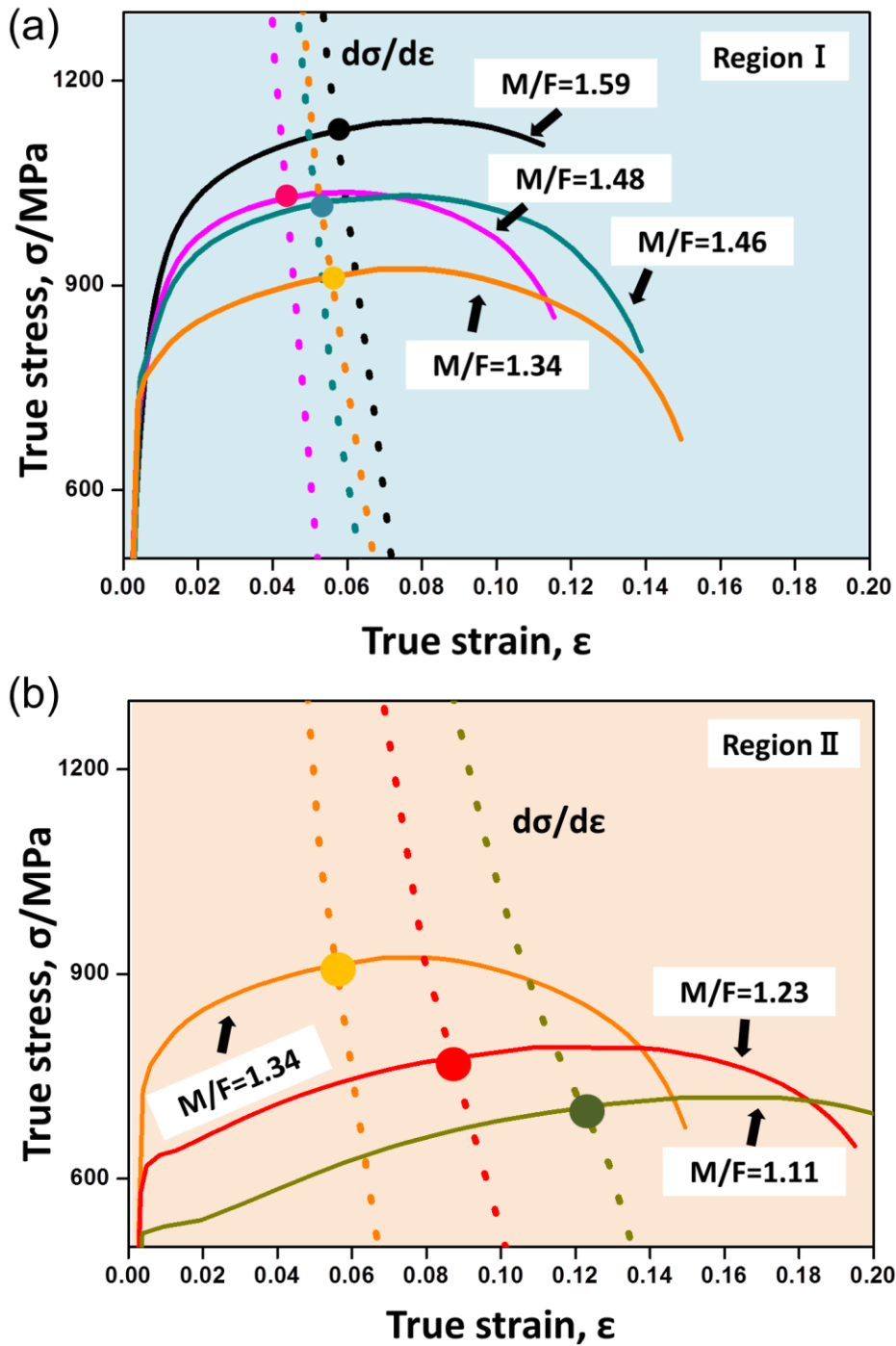


Fig. 2.11 True stress-strain curve and work hardening rate for the specimens in the region I ($M/F < 1.34$) and in the region II ($M/F > 1.34$). In the region I ($M/F < 1.34$), (b) in the region II ($M/F > 1.34$)

Fig. 2.11a shows the work hardening rate curves of the specimens in region I ($M/F < 1.34$). It is seen that in the specimens with $M/F < 1.34$, there is no remarkable difference in the work hardening rate in the specimens in in region I ($M/F < 1.34$). The tensile strength of the specimen ($M/F=1.59$) is higher than the other specimens in in region I, the onset of plastic instability starts at a similar strain level, leading to similar uniform elongations in the specimens. On the other hand, in region II ($M/F > 1.34$), the work hardening rate in the high M/F specimens become larger than that in the small M/F specimens, leading to delay the onset of plastic instability and larger uniform elongation in high M/F specimens.

It is noteworthy that the uniform elongation of the specimens in region I ($M/F < 1.34$) almost keep constant, although the strength continuous increasing with increase nanohardness ratio (M/F). The detailed reasons such as local strain and stress partitioning in ferrite and martensite phases will be shown and discussed in **Chapter 3**.

2.6. Conclusions

In **Chapter 2**, dual phase steel consisting martensite and ferrite was tempered for 3.6 ks at various temperatures ranging from 200 to 600 °C, and the changes of microstructure and mechanical properties with tempering temperature were investigated. The key results obtained are summarized as follows:

(1) The tempering treatments resulted in carbide precipitation and coarsening of martensite structure. It was suggested that finely precipitated carbides in the specimens tempered below 300 °C pinned mobile dislocations, leading to the slight increase of 0.2% proof stress.

(2) The nanohardness values of martensite and ferrite decreased with increasing the tempering temperature. The ultimate tensile strength monotonously decreased with decreasing the ratio of nanohardness between martensite and ferrite (M/F). On the other hand, the tendency of uniform elongation could be classified into two regions. In the region I where the hardness ratio (M/F) is smaller than 1.34 (corresponding to the tempering temperatures above 400 °C), the uniform elongation increased with decreasing the nanohardness ratio. In contrast, the uniform elongation was independent of the nanohardness ratio in the region II (M/F > 1.34, corresponding to the tempering temperatures below 400 °C). It was concluded that the nanohardness ratio

can be a good parameter for controlling the mechanical properties of dual phase steels.

The uniform elongation change in dual phase steels could be explained in terms of plastic instability.

References

- [1] A. Fallahi, *J Mater Sci Technol*, 18 (2002) 451-454.
- [2] C. Wei, J. Zhang, S. Yang, L. Sun, W. Tao, F. Wu, W. Xia, *Sci Technol Weld Joi*, 20 (2015) 145-154.
- [3] P. Matteis, G. Scavino, F. D'Aiuto, D. Firrao, *Steel Res Int*, 83 (2012) 950-956.
- [4] R. Koganti, A. Elliott, C. Orsette, *Asme, RESISTANCE SPOT WELDING EVALUATION OF 1.4 MM ELECTRO GALVANIZED (EG) DUAL PHASE 780 (DP780) AND 1.6 MM ELECTRO GALVANIZED TRANSFORMATION INDUCED PLASTICITY 780 (TRIP780) STEEL FOR AUTOMOTIVE BODY STRUCTURAL APPLICATIONS*, 2012.
- [5] S. Celotto, A. Kamp, A. Kampf, *Tata Steel Nederland Technology Bv; Corus Technology Bv*.
- [6] XS. Liao, XD. Wang, X.F. Li, ZH. Guo, YH. Rong, *Design and characterization of ultrahigh strength dual-phase steel with low ratio of yield strength/ultimate tensile strength*, in: Z. Jiang, C.L. Zhang (Eds.) *Manufacturing Science and Engineering*, Pts 1-5, 2010, pp. 728-732.
- [7] P.C. Chakraborti, M.K. Mitra, *Mat Sci Eng a-Struct*, 466 (2007) 123-133.
- [8] N.D. Beynon, S. Oliver, T.B. Jones, G. Fourlaris, *Mater Sci Tech-Lond*, 21 (2005) 771-778.
- [9] T. Sakaki, K. Sugimoto, T. Fukuzato, *Acta Metallurgica*, 31 (1983) 1737-1746.
- [10] K. Kunishige, N. Nagao, S. Hamamatsu, S. Sugisawa, *T Iron Steel I Jpn*, 23 (1983) B71-B71.

- [11] N. Yamauchi, T. Taka, K. Kunishige, N. Nagao, T Iron Steel I Jpn, 22 (1982) B107-B107.
- [12] S.S. Hansen, R.R. Pradhan, Jom-J Min Met Mat S, 32 (1980) 30-30.
- [13] Y. Mazaheri, A. Kermanpur, A. Najafizadeh, Isij Int, 55 (2015) 218-226.
- [14] N. Saeidi, F. Ashrafizadeh, B. Niroumand, Mat Sci Eng a-Struct, 599 (2014) 145-149.
- [15] M.P. Rao, V.S. Sarma, S. Sankaran, Metall Mater Trans A, 45A (2014) 5313-5317.
- [16] A. Karmakar, R.D.K. Misra, S. Neogy, D. Chakrabarti, Metall Mater Trans A, 44A (2013) 4106-4118.
- [17] Y. Kang, QH. Han, XM. Zhao, MH. Cai, Mater Design, 44 (2013) 331-339.
- [18] A. Ramazani, K. Mukherjee, U. Prahl, W. Bleck, Metall Mater Trans A, 43A (2012) 3850-3869.
- [19] Y. Chen, E. Wang, Y. Guo, W. Chen, The law of the grain size changing in the warm tension test for the B340/590DP dual-phase steel, in: H.X. Zhang, Y. Han, F. Chen, J. Wen (Eds.) Materials and Computational Mechanics, Pts 1-3, 2012, pp. 1264-1268.
- [20] P.R. Mondi, V.S. Sarma, S. Sankaran, T Indian I Metals, 64 (2011) 89-92.
- [21] M. Calcagnotto, Y. Adachi, D. Ponge, D. Raabe, Acta Mater, 59 (2011) 658-670.
- [22] K. Mukherjee, S.S. Hazra, M. Militzer, Metall Mater Trans A, 40A (2009) 2145-2159.
- [23] J. Zhou, A.M. Gokhale, A. Gurusurthy, S.P. Bhat, Mat Sci Eng a-Struct, 630 (2015) 107-115.
- [24] J. Zhang, H. Di, Y. Deng, R.D.K. Misra, Mat Sci Eng a-Struct, 627 (2015) 230-240.

- [25] M. Zaeimi, A. Basti, M. Alitavoli, *J Mater Eng Perform*, 24 (2015) 1781-1789.
- [26] S.K. Paul, N. Stanford, T. Hilditch, *Mat Sci Eng a-Struct*, 638 (2015) 296-304.
- [27] Q. Lai, O. Bouaziz, M. Goune, L. Brassart, M. Verdier, G. Parry, A. Perlade, Y. Brechet, T. Pardoën, *Mat Sci Eng a-Struct*, 646 (2015) 322-331.
- [28] M. Turkmen, S. Gunduz, *Acta Metall Sin-Engl*, 27 (2014) 279-289.
- [29] T. Matsuno, D. Maeda, H. Shutoh, A. Uenishi, M. Suehiro, *Isij Int*, 54 (2014) 938-944.
- [30] A. Ghaheri, A. Shafyei, M. Honarmand, *Mater Design*, 62 (2014) 305-319.
- [31] S.K. Paul, *Mater Design*, 50 (2013) 782-789.
- [32] M.R. Akbarpour, A. Ekrami, *Mat Sci Eng a-Struct*, 477 (2008) 306-310.
- [33] S.K. Paul, N. Stanford, T. Hilditch, *Mat Sci Eng a-Struct*, 644 (2015) 53-60.
- [34] M. Turkmen, S. Gunduz, *J Fac Eng Archit Gaz*, 28 (2013) 353-362.
- [35] E. Ahmad, T. Manzoor, M.M.A. Ziai, N. Hussain, *J Mater Eng Perform*, 21 (2012) 382-387.
- [36] J. Kadkhodapour, S. Schmauder, D. Raabe, S. Ziaei-Rad, U. Weber, M. Calcagnotto, *Acta Mater*, 59 (2011) 4387-4394.
- [37] M. Azuma, S. Goutianos, N. Hansen, G. Winther, X. Huang, *Mater Sci Tech-Lond*, 28 (2012) 1092-1100.
- [38] C. Peng-Heng, A.G. Preban, *Acta Metallurgica*, 33 (1985) 897-903.
- [39] Y. Mazaheri, A. Kermanpur, A. Najafizadeh, *Mat Sci Eng a-Struct*, 639 (2015) 8-14.
- [40] J. Breuils, H. Pelletier, J. Krier, V. Vignal, *Surf Coat Tech*, 204 (2010) 2068-2072.
- [41] V.H. Baltazar Hernandez, S.K. Panda, Y. Okita, N.Y. Zhou, *J Mater Sci*, 45 (2010) 1638-1647.

- [42] V.H. Baltazar Hernandez, S.K. Panda, M.L. Kuntz, Y. Zhou, *Mater Lett*, 64 (2010) 207-210.
- [43] B.-W. Choi, D.-H. Seo, J.-Y. Yoo, J.-i. Jang, *J Mater Res*, 24 (2009) 816-822.
- [44] M. Delince, P.J. Jacques, T. Pardoen, *Acta Mater*, 54 (2006) 3395-3404.
- [45] K. Hayashi, K. Miyata, F. Katsuki, T. Ishimoto, T. Nakano, *J Alloy Compd*, 577 (2013) S593-S596.
- [46] T. Ohmura, K. Tsuzaki, S. Matsuoka, *Scripta Mater*, 45 (2001) 889-894.
- [47] F. Maresca, V.G. Kouznetsova, M.G.D. Geers, *Scripta Mater*, 110 (2016) 74-77.
- [48] E. Fereiduni, S.S.G. Banadkouki, *J Alloy Compd*, 577 (2013) 351-359.
- [49] J.Y. Koo, M.J. Young, G. Thomas, *Metall Trans A*, 11 (1980) 852-854.
- [50] S. Kuang, Y.L. Kang, H. Yu, R.D. Liu, *Int J Min Met Mater*, 16 (2009) 393-398.
- [51] N. Tsuji, Y. Ito, Y. Saito, Y. Minamino, *Scripta Mater*, 47 (2002) 893-899.

Chapter 3: Effect of hardness ratio between two phases on deformation behavior in dual phase steel

3.1 Introduction

As described in **Chapter 1**, the strength and ductility are usually show tradeoff relationship in traditional steels (plain-carbon steels, martensite steels, etc.). However, dual phase (DP) steel with various hardness ratios between martensite and ferrite shows a new relationship which breaks the tradeoff relationship between strength and elongation shown in **Fig. 2.9** in **Chapter 2**. As described in **Chapter 2**, with increasing the tensile strength, the uniform elongation maintained in DP steels ($M/F \geq 1.34$, M/F : refers hardness ratio between martensite phase and ferrite phase in this study). This new relationship in DP steel was explained in terms of plastic instability[1] in **Fig. 2.11a** in **Chapter 2**. The work hardening rate in DP steels($M/F \geq 1.34$) increased to keep DP steel stable resulting in maintaining the uniform elongation. However, the reason for increasing the work hardening rate in DP steels ($M/F \geq 1.34$) has not been clarified yet in **Chapter 2**. Therefore, the reason for increasing the work hardening rate to maintain the uniform elongation in DP steels will be investigated in

this Chapter by studying the local deformation behavior of martensite phase and ferrite phase in DP steel using digital image correlation (DIC) method.

3.2 Experimental procedure

3.2.1. Materials

In this study, chemical composition of the steel and the heat treatment process are the same as it used in **Chapter 2**. The chemical composition of the steel is presented in **Table 2.1**. The heat treatment process is shown in **Fig. 2.1**.

3.2.2 Local strain measurement by DIC method

As introduced in **Chapter 1**, the position change in specimen can be traced by DIC method. In this study, DIC method was applied to measure the local strain distribution and phases strain in martensite and ferrite DP steels[2]. The details of the local strain measurement in this study are shown as follows. (1) Get scanning electron microscope (SEM) images under various tensile strains. The specimen was tensile deformed at different strains, and SEM images were taken after unloading the specimen from tensile test machine. In order to know the position of the local deformation area in the whole specimen, surface indentation was marked on the specimen surface near the position where SEM images were taken. (2) Compare the SEM images by DIC software

(Correlated Solution company, DIC-2D, 2009) to measure local strain distribution and local strains in martensite phase and ferrite phase in DP steels. **Figure 3.1** shows an example of DIC method applied in this study. **Fig. 3.1a** shows the OM image of unloading specimen (M/F=1.1) of DP steel tensile deformed at 20.8%. Position A (marked by black point) is the position where SEM images are taken. Necking region of the specimen is identified by reduction of gage-section of the specimen. Necking region is marked on the specimen between two red solid lines. The stress-strain curve of the specimen is shown in **Fig. 3.1b**. The tensile strain is measured by crosshead travel. The tensile strain of the specimen shown in Fig. 3.1a is marked in dash line in **Fig. 3.1b**. **Fig. 3.1(c-d)** show SEM images of DP steel before tensile deformation ($\epsilon=0\%$) and after tensile deformation ($\epsilon=3.8\%$). **Fig. 3.1e** shows the mapping of equivalent stain by comparing two SEM images (**Fig. 3.1(c-d)**) using DIC software. In order to measure the local strain distribution in martensite phase and ferrite phase, martensite phase in **Fig. 3.1c** is painted into white, and then overlapped with **Fig. 3.1e** to find local strains in martensite phase and ferrite phase. Martensite phase and ferrite phase are recognized by their microstructure difference. Martensite phase in SEM image (captured after the specimen etched in a 3 % nital solution) shows a relatively bright color and uneven surface, on the contrary, ferrite phase shows a dark color and

smooth surface. The overlapped map is shown in **Fig. 3.1f**, hereinafter referred to as strain map in this study. All the local strain measurements in this study are measured the positions out of the necking region in DP steels.

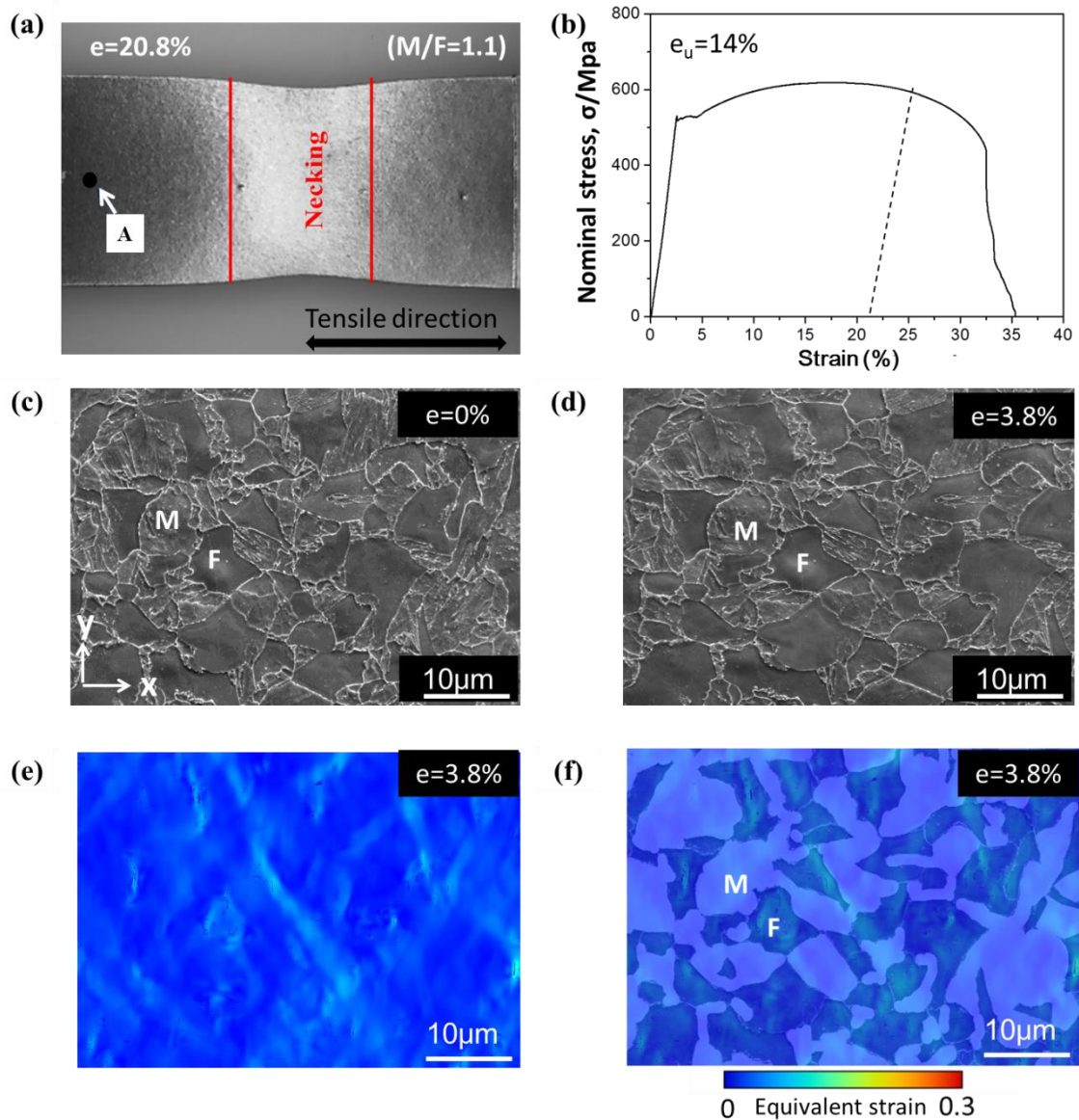


Figure 3.1 illustration of the DIC method applied in this study. (a) OM image of unloading specimen ($M/F=1.1$) of DP steel tensile deformed at 20.8%. Position A (black point) is the marked position where capture SEM images for DIC comparison. (b) The stress-strain curve of the specimen. The tensile strain is measured by crosshead travel. (c) SEM images of DP steel before tensile deformation ($e=0\%$) and

(d) after tensile deformation ($\epsilon=3.8\%$) (e) Mapping of equivalent strain by comparing two SEM images (c-d) using DIC software. (f) Equivalent strain map obtained by overlapping SEM image ($\epsilon=0\%$) and strain mapping. Equivalent strain value is shown by color. Blue color is representing low local strain and red color is representing high local strain. M and F are representing martensite phase and ferrite phase, respectively.

3.3 Strain partitioning in martensite-based dual phase steel.

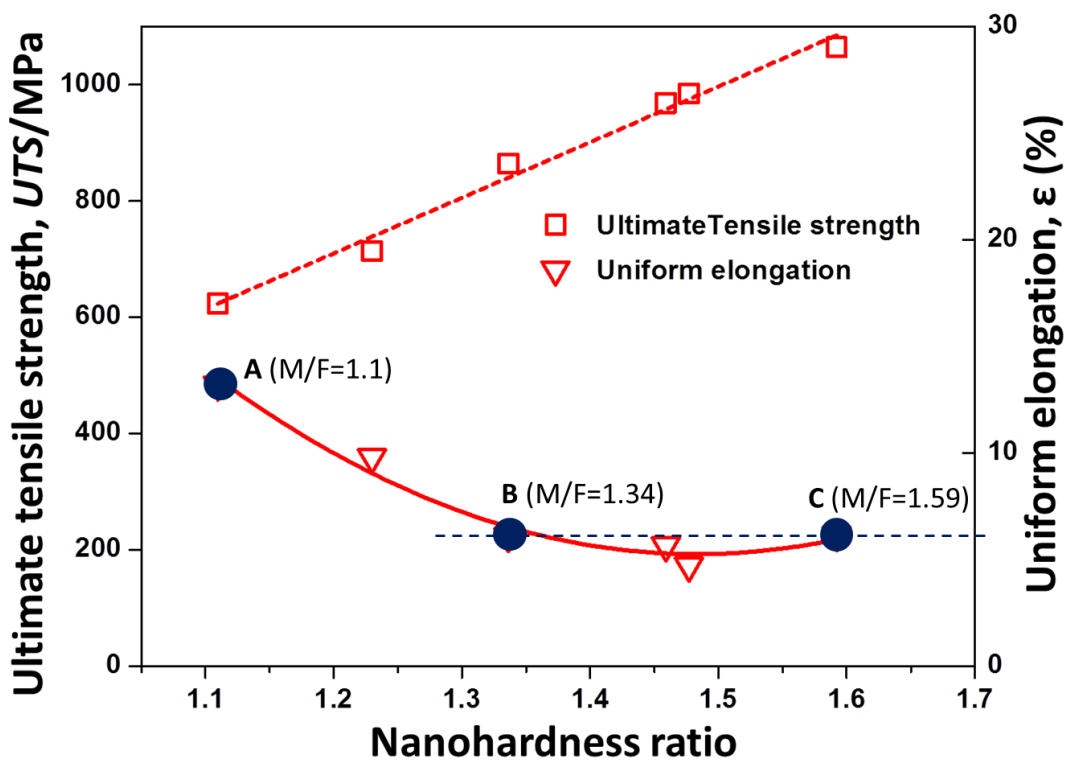


Figure 3.2 Ultimate tensile strength and uniform elongation in the DP steel summarized as a function of the nanohardness ratio. Specimens A ($M/F=1.1$), B ($M/F=1.34$) and C ($M/F=1.59$) are marked using blue points.

As mentioned in **Chapter 2**, it is interesting that the relationship of tensile strength and uniform elongation in DP steels ($M/F \geq 1.34$) can break the tradeoff relationship in conventional steels. **Figure 3.2** shows ultimate tensile strength and uniform

elongation in the DP steel as a function of the nanohardness ratio. The tensile strength increased in DP steels ($M/F \geq 1.34$), while the uniform elongation maintained. In order to clarify the reason in detail, specimens A ($M/F=1.1$), B ($M/F=1.34$) and C ($M/F=1.59$) shown in **Fig. 3.2** are selected to study the local strain distribution in DP steels during deformation.

3.3.1 Strain partitioning in specimen A ($M/F=1.1$)

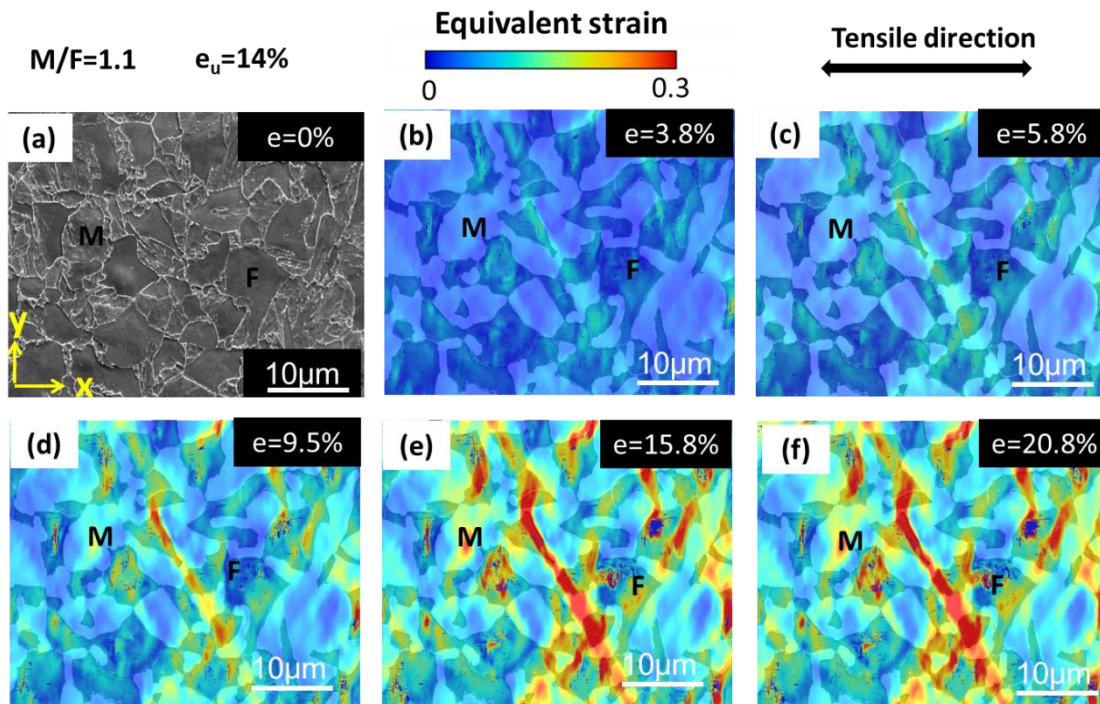


Figure 3.3 Strain maps of specimen A tensile deformed (b) $e=3.8\%$, (c) 5.8% , (d) 9.5% (e) 15.8% and (f) 20.8% . (a) SEM image of specimen A before deformation. “M”, “F” represent martensite phase and ferrite phase, respectively. The uniform elongation of specimen A is 14% . Tensile direction t is in horizontal direction.

Figure 3.3 shows the strain maps of specimen A tensile deformed at 3.8% , 5.8% , 9.5% ,

15.8% and 20.8%. **Fig. 3.3a** is the SEM image of specimen A without deformation. Tensile direction is in horizontal direction. The red color in strain map represent high strain and blue color in strain map represent low strain. From strain maps shown in **Fig. 3.10 (b-f)**, the high strain color (yellow and red color) increase with increasing tensile strain. On the other hand, the low strain color (blue color) decreases with increasing tensile strain. The morphology of high strain in strain maps is showing line-like morphology. The spread direction of the line-like high strain is inclined to the tensile direction at an angle of about 45 degrees.

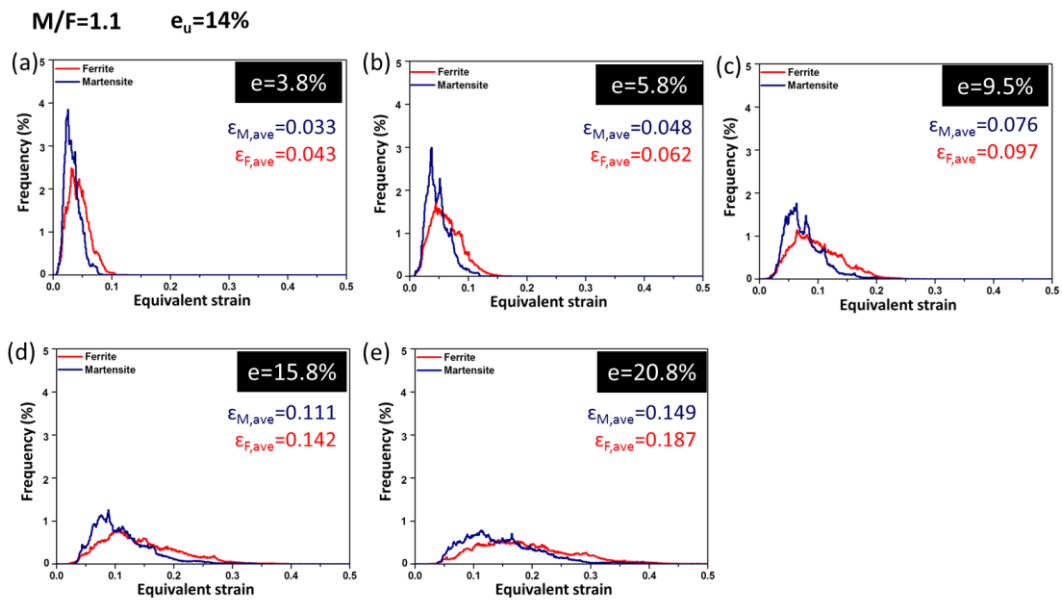


Figure 3.4 Local strain distribution in ferrite phase and martensite phase obtained from strain maps in **Fig. 3.3**. The local strain distributed in martensite phase and ferrite phase are separated. The uniform elongation of specimen A is 14%. The bin size of the distribution is an equivalent strain of 0.001.

Figure 3.4 shows Local strain distribution in ferrite phase and martensite phase

obtained from strain maps in **Fig .3.3**. The local strain distributed in martensite phase and ferrite phase are separated and plotted as histograms into blue curve and red curve, respectively. The average local strain in martensite phase ($\epsilon_{M,ave}$) and ferrite phase ($\epsilon_{F,ave}$) are both increased with increasing tensile strain. In addition, at the beginning of tensile deformation ($e=3.8\%$) (**Fig. 3.3a**), it can be seen both high strain region (equivalent strain near 0.1) and low strain region (equivalent strain near 0) are distributed in ferrite phase and martensite. With further deformation ($e=5.8\%$ to $e=9.5\%$) before specimen necking (**Fig. 3.3(b-c)**), both high strain region and low strain region in ferrite phase and martensite phase are shifted into larger strain level. This indicates that the deformation in martensite phase and in ferrite phase is relatively homogeneous. **Fig. 3.3d** and **Fig. 3.13e**, show the strain distributed in ferrite phase and martensite phase after specimen necking, which are considered to be associated with post uniform deformation (deformation after necking). The details will be discussed and studied in the future study.

3.3.2 Strain partitioning in specimen B (M/F=1.34)

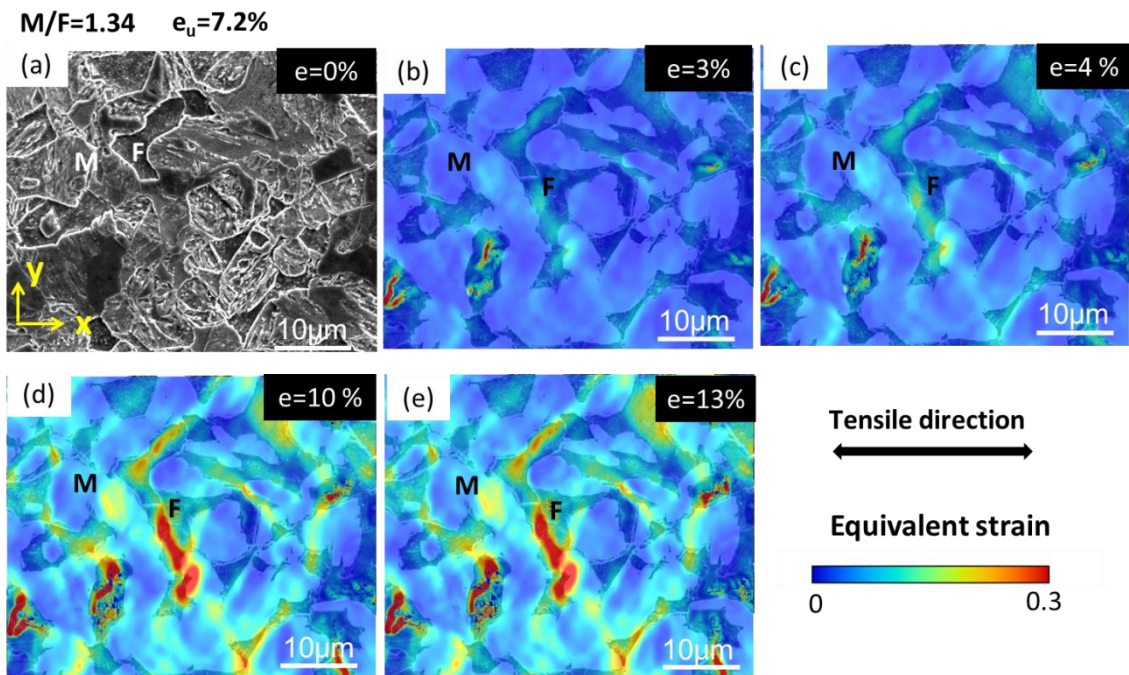


Figure 3.5 Strain maps of specimen B tensile deformed (b) $e=3\%$, (c) 4% , (d) 10% and (e) 13% . (a) SEM image of specimen B before deformation. “M”, “F” represent martensite phase and ferrite phase, respectively. The uniform elongation of specimen B is 7.2% . Tensile direction t is in horizontal direction.

Figure 3.5 shows the strain maps of specimen b tensile deformed at 3% , 4% , 10% and 13% . **Fig. 3.5a** is the SEM image of specimen B without deformation. The red color in strain map represent high strain and blue color in strain map represent low strain. Tensile direction is in horizontal direction. From strain maps shown in **Fig. 3.5 (b-e)**, the high strain color (yellow and red color) increase with increasing tensile strain. On the other hand, the low strain color (blue color) decreases with increasing tensile strain. The morphology of high strain in strain maps is showing strip-like morphology. The spread direction of the strip-like high strain is inclined to the tensile direction at an

angle of about 45 degrees. The strip-like high strains are tent to connect with each other.

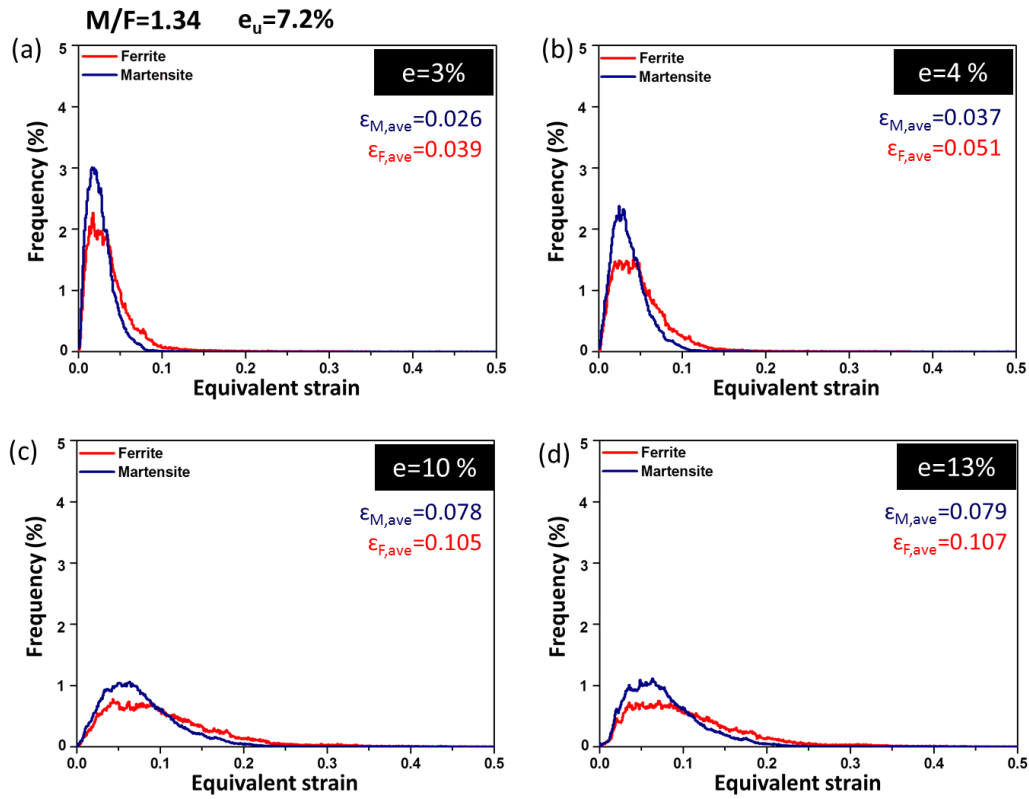


Figure 3.6 Local strain distribution in ferrite phase and martensite phase obtained from strain maps in **Fig .3.5**. The local strain distributed in martensite phase and ferrite phase are separated. The uniform elongation of specimen B is 7.2%. The bin size of the distribution is an equivalent strain of 0.001.

Figure 3.6 shows Local strain distribution in ferrite phase and martensite phase obtained from strain maps in **Fig .3.5**. The local strain distributed in martensite phase and ferrite phase are separated and plotted as histograms into blue curve and red curve, respectively. The average local strain in martensite phase ($\epsilon_{M,ave}$) and ferrite phase

($\epsilon_{F,ave}$) are both increased with increasing tensile strain before specimen necking. In addition, at the beginning of tensile deformation ($e=3\%$) (**Fig. 3.6a**), it can be seen both high strain region (equivalent strain near 0.1) and low strain region (equivalent strain near 0) are distributed in ferrite phase and martensite. With further deformation ($e=4\%$ to $e=10\%$), just after specimen necking (**Fig. 3.6(b-c)**), the low strain region in martensite and ferrite phase is still located in the small strain region, while the high strain region in martensite and ferrite is shifted into larger strain level. This indicates that the deformation in martensite phase and in ferrite phase is relatively inhomogeneous. Compare with the **Fig.3.6c** and **Fig. 3.6d**, the strain distributed in ferrite phase and martensite phase almost no change after the specimen necking. Since the observed area is out of necked region, which means the local strain is localized in necked region after the specimen necking. This result is considered to be associated with post uniform deformation (deformation after necking). The details will be discussed and studied in the future study.

3.4.3 Strain partitioning in specimen C (M/F=1.59)

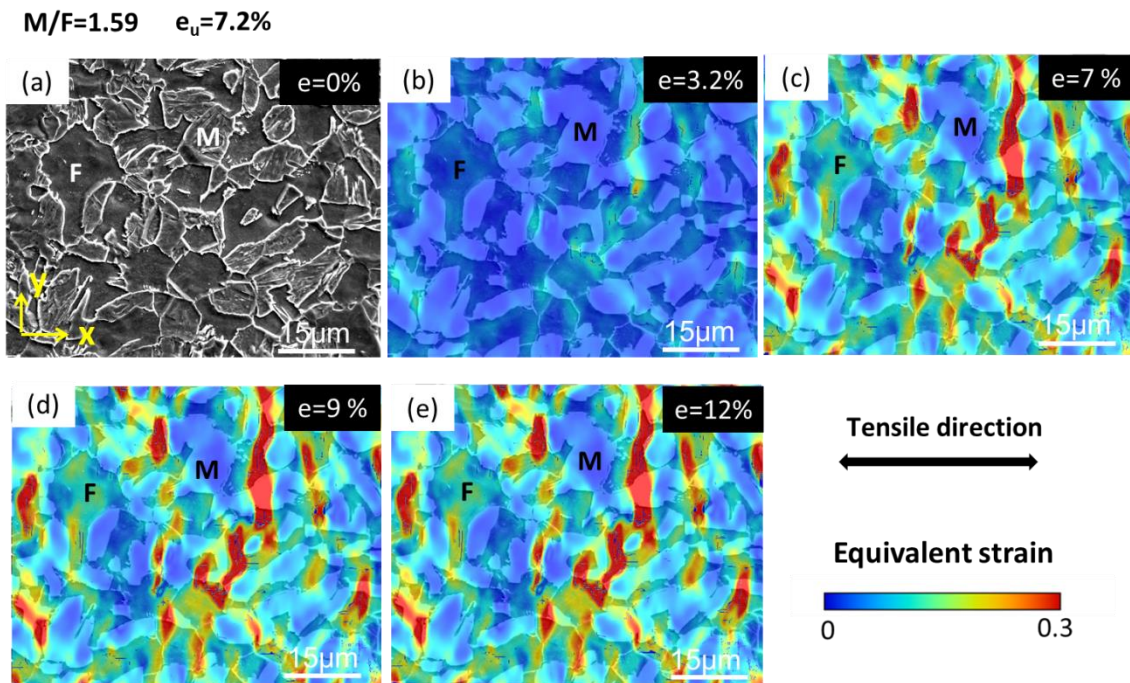


Figure 3.7 Strain maps of specimen C tensile deformed (b) $e=3.2\%$, (c) 7% , (d) 9% (e) 12% . (a) SEM image of specimen C before deformation. “M”, “F” represent martensite phase and ferrite phase, respectively. The uniform elongation of specimen B is 7.2% . Tensile direction t is in horizontal direction.

Figure 3.7 shows the strain maps of specimen C tensile deformed at 3.2% , 7% , 9% and 12% . **Fig. 3.7a** is the SEM image of specimen C without deformation. The red color in strain map represent high strain and blue color in strain map represent low strain. Tensile direction is in horizontal direction. From strain maps shown in **Fig. 3.7 (b-e)**, the high strain color (yellow and red color) increase with increasing tensile strain. On the other hand, the low strain color (blue color) decreases with increasing tensile strain. The morphology of high strain in strain maps is showing rod-like morphology. The spread direction of the rod-like high strain is inclined to perpendicular to the tensile

direction.

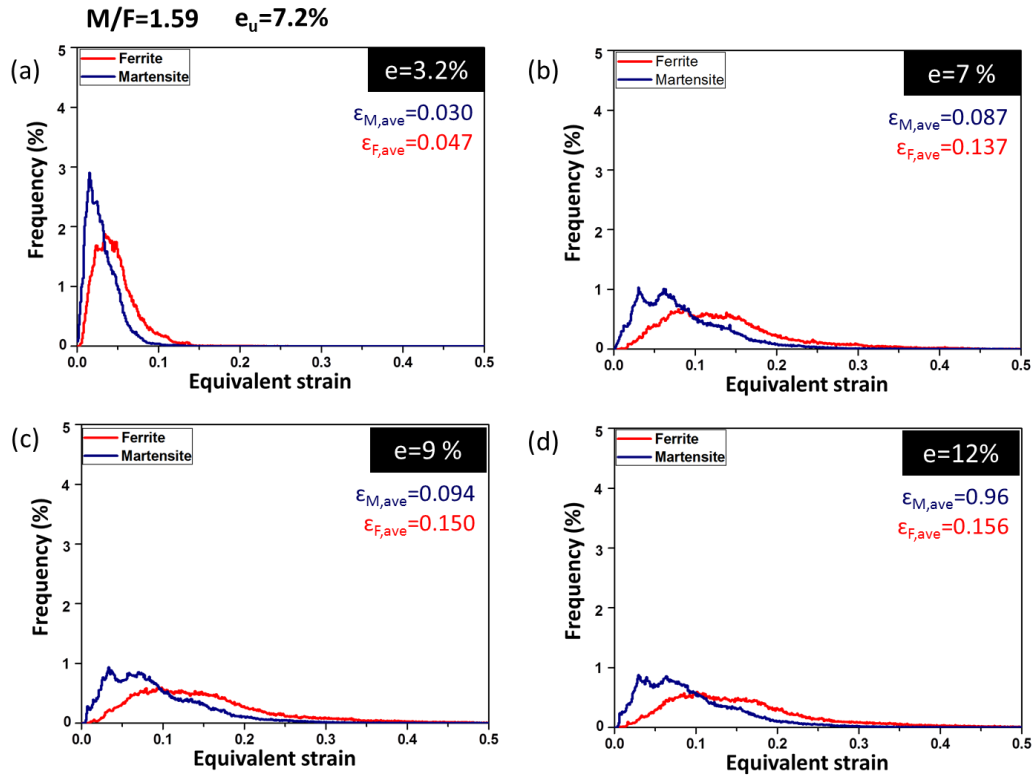


Figure 3.8 Local strain distribution in ferrite phase and martensite phase obtained from strain maps in **Fig .3.7**. The local strain distributed in martensite phase and ferrite phase are separated. The uniform elongation of specimen C is 7.2%. The bin size of the distribution is an equivalent strain of 0.001.

Figure 3.8 shows Local strain distribution in ferrite phase and martensite phase obtained from strain maps in **Fig .3.7**. The local strain distributed in martensite phase and ferrite phase are separated and plotted as histograms into blue curve and red curve, respectively. The average local strain in martensite phase ($\epsilon_{M,ave}$) and ferrite phase ($\epsilon_{F,ave}$) are both increased with increasing tensile strain before specimen necking. In

addition, at the beginning of tensile deformation ($e=3\%$) (**Fig. 3.8a**), it can be seen both high strain region (equivalent strain near 0.1) and low strain region (equivalent strain near 0) are distributed in ferrite phase and martensite. With further deformation ($e=7\%$ to $e=9\%$), just after specimen necking (**Fig. 3.8(b-c)**), the low strain region in martensite and ferrite phase is still located in the small strain region, while the high strain region in martensite and ferrite is shifted into larger strain level. This indicates that the deformation in martensite phase and in ferrite phase is relatively inhomogeneous. Compare with the **Fig.3.6c** and **Fig. 3.6d**, the strain distributed in ferrite phase and martensite phase almost no change after the specimen necking. Since the observed area is out of necked region, which means the local strain is localized in necked region after the specimen necking. This result is considered to be associated with post uniform deformation (deformation after necking). The details will be discussed and studied in the future study.

3.4.4 Comparison of the deformation behaviors of specimens with different hardness ratios

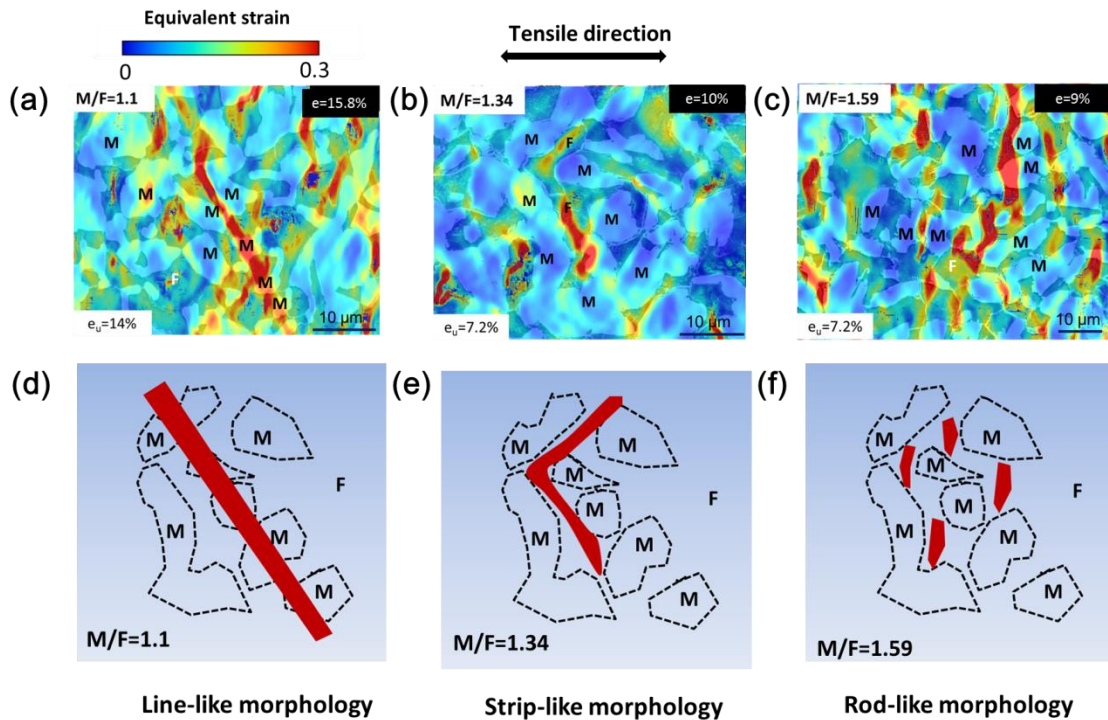


Figure 3.9 Strain maps of the specimens after necking and the illustrations of high strain in specimens A (M/F=1.1), B (M/F=1.34) and C (M/F=1.59). (a) Strain map of specimen A tensile deformed at 15.8%, (b) strain map of specimen B tensile deformed at 10%, (c) strain map of the specimen C tensile deformed at 9% ,(d) high strain in specimen A shows line-like morphology, (e) high strain in specimen B shows strip-like morphology, and (f) high strain in specimen C shows rod-like morphology. “M”, “F” represent martensite phase and ferrite phase, respectively.

Figure 3.9 shows strain maps of the specimens after necking and the illustrations of high strain in specimens A (M/F=1.1), B (M/F=1.34) and C (M/F=1.59). **Fig. 3.9a** shows strain map of specimen A tensile deformed at 15.8%. The hardness ratio between martensite and ferrite phase in specimen A is small (M/F=1.1). The high

strain shows line-like morphology in the strain map of specimen A shown in **Fig. 3.9a**. It can be seen the line-like high strain propagates through martensite phase and ferrite phase without considering the phase's type. **Fig. 3.9b** shows the strain map of the specimen B. Compared with specimen A ($M/F=1.1$), the hardness ratio (M/F) between martensite phase and ferrite phase in specimen B ($M/F=1.34$) become larger, which indicate martensite become harder. The high strain seems hard to propagate through martensite, due to the hardness ratio increase. And the high strain in specimen B shows strip-like morphology in the strain map shown in **Fig. 3.9b**. And the high strain shown in the strain map of specimen B tends to connect with each other. With further increase the hardness ratio (M/F), the martensite phase becomes much harder. **Fig. 3.9c** shows the strain map of specimen C ($M/F=1.59$), the hard martensite phase constrained the high strain in ferrite phase region. And the high strain is separated by hard martensite. The high strain in specimen C shows rod-like morphology, which is perpendicular to the tensile direction.

3.4.5 Discussion

As discussed in Chapter 2, according to Considère's criterion [1](eq 2.2) for plastic instability, necking will appear if the true flow stress becomes larger than the work hardening rate. When the equation is satisfied (work hardening rate became smaller than true stress), necking takes place and uniform elongation can be determined. When the true stress and true strain meet the equation (2), the true strain ϵ equals the uniform elongation of the specimen. If the work hardening rate does not change for different specimens, when the true stress (ultimate) increase, the uniform elongation will decrease.

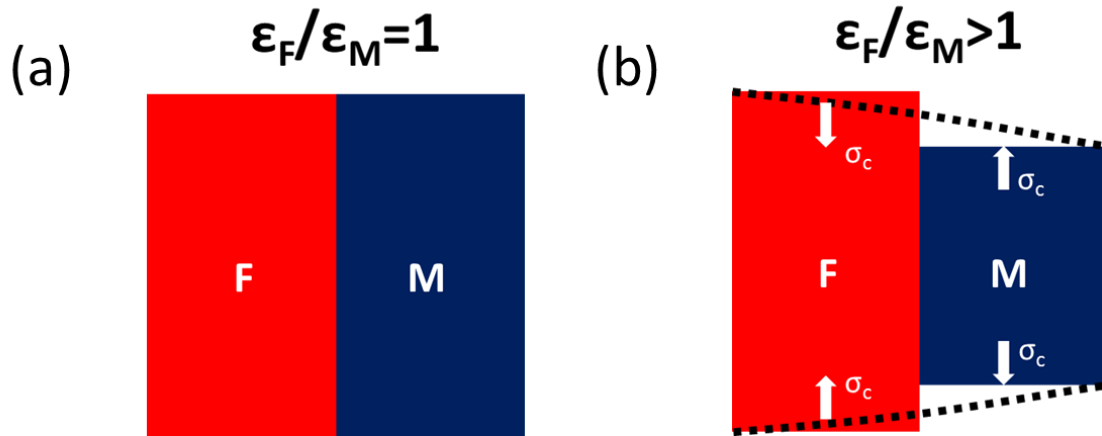


Figure 3.10 illustration of phases stress generate between martensite phase and ferrite phase. ϵ_F/ϵ_M : strain(average phase strain) ratio between ferrite phase and martensite phase; σ_c : compatibility stress (phase stress); “M”, “F” represent martensite phase and ferrite phase, respectively.

Figure 3.10 show illustration of phases stress generate between martensite phase and

ferrite phase. **Fig. 3.10a** show the case of $\varepsilon_F/\varepsilon_M=1$. It means the same strain changes on ferrite phase and martensite phase simultaneously. In this case, there is no extra stress generate between two phases. Fig.3.14b show another case of $\varepsilon_F/\varepsilon_M>1$. It means the more strain distribute on ferrite phase than on martensite phase under the same load. Consider the connection (or interphase) between ferrite phase and martensite phase, there must generate a compatibility stress σ_c (or phase stress) to sustain their connection. The compatibility stress σ_c increases with increasing $\varepsilon_F/\varepsilon_M$.

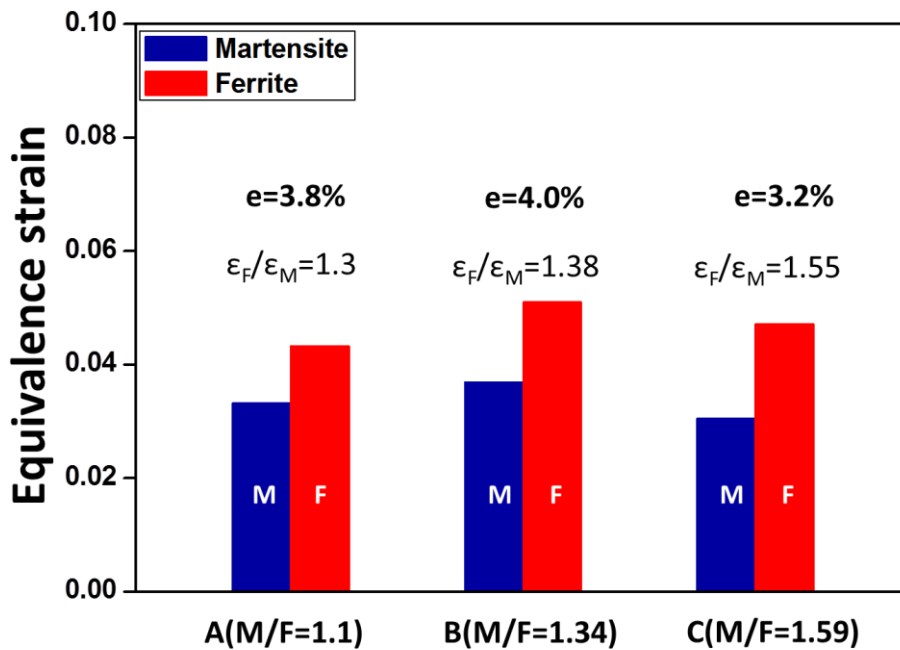


Figure 3.11 Average phase strain in martensite phase and ferrite phase in specimen A, specimen B and specimen C. $\varepsilon_F/\varepsilon_M$: strain(average phase strain) ratio between ferrite phase and martensite phase;

Figure 3.11 shows average phase strain in martensite phase and ferrite phase in specimen A, specimen B and specimen C. Specimen A, B and C were deformed at the similar tensile strain. The strain ratio (ϵ_F/ϵ_M) on specimen C is larger than specimen A and specimen B. Large strain ratio between ferrite and martensite will generate a larger compatibility stress to keep the strain change continuously between two phases (because two phases are connected by interphase boundary). This large compatibility stress will enhance the strain hardening in specimen C. This might be the reason why although the tensile strength in specimen C is higher than in specimen B, the uniform elongation in specimen C is nearly the same as in specimen B.

3.6 Conclusions

In Chapter 3, local deformation behavior of martensite phase and ferrite phase in DP steels with various hardness ratios between martensite phase and ferrite phase was studied. The main results are summarized as follows:

1. DIC results of the local strain distribution in martensite phase and ferrite phase in specimen A (M/F=1.1). The average local strain in martensite phase ($\epsilon_{M,ave}$) and ferrite phase ($\epsilon_{F,ave}$) are both increased with increasing tensile strain. Both high strain region and low strain region in ferrite phase and martensite phase are shifted into larger strain level. This indicates that the deformation in martensite phase and in ferrite phase is relatively homogeneous. It can be seen the line-like high strain generates in the strain map and propagates through martensite phase and ferrite phase without considering the phase's type.

2. DIC results of the local strain distribution in martensite and ferrite phase in specimen B (M/F=1.34) and specimen C (M/F=1.59). The average local strain in martensite phase ($\epsilon_{M,ave}$) and ferrite phase ($\epsilon_{F,ave}$) are both increased with increasing tensile strain before specimen necking. During tensile deformation, the low strain region in martensite and ferrite phase is still located in the small strain region, while the high strain region in martensite and ferrite is shifted into larger strain level. This indicates

that the deformation in martensite phase and in ferrite phase is relatively inhomogeneous. Due to the large hardness difference between martensite and ferrite phase, the high strain is constrained in ferrite phase by hard martensite phase. In specimen B (M/F=1.34), the high strain show strip-like morphology and the high strain tend to connected with each other. In specimen C (M/F=1.59), the high strain show rod-like morphology perpendicular to the tensile direction and the high strain is separated by hard martensite phase. The present result suggests that the local high strain morphology can be controlled by changing the nanohardness ratio between martensite and ferrite in DP steels.

3. As shown **Fig. 2.9** in Chapter 2, with increasing tensile strength, the uniform elongation maintained in dual phase steels ($M/F \geq 1.34$). It is found that the strain ratio (local strain partitioning between ferrite and martensite) increase with increasing nanohardness ratio between martensite and ferrite at similar tensile strain. Large difference of strain partitioning between ferrite and martensite will generate large phase stress which enhance the stain hardening in the specimens.

Reference

[1] N. Tsuji, Y. Ito, Y. Saito, Y. Minamino, *Scripta Mater*, 47 (2002) 893-899.

[2] Y. Ososkov, D.S. Wilkinson, M. Jain, T. Simpson, *Int J Mater Res*, 98 (2007) 664-673.

Chapter 4 Effect of volume fraction of martensite on deformation behavior in dual phase steel

4.1. Introduction

As investigation in **Chapter 2** and **Chapter 3**, hardness ratio (M/F) between martensite phase and ferrite phase in dual phase (DP) steel could be a good parameter for controlling the strength and ductility in DP steels. The ultimate tensile strength had a linear relationship with nanohardness ratio of martensite and ferrite. By changing nanohardness ratios (M/F) in DP steels, the relationship between tensile strength and uniform elongation break the tradeoff relationship of conventional steels. With increasing tensile strength, the uniform elongation maintained in DP steels with various nanohardness ratios ($M/F \geq 1.34$). The reason investigated in **Chapter 2** shows that the maintained uniform elongation in DP steels is due to the work hardening rate increase. In order to understand the reason more in detail, local deformation of martensite phase and ferrite phase were studied in DP steels with various nanohardness ratios between martensite phase and ferrite phase in **Chapter 3**. It is found that large hardness difference between martensite and ferrite in DP steels will generate large phase stress between martensite phase and ferrite phase during plastic deformation. And large

phase stress between two phases enhanced strain hardening in DP steels. However, all the present results are based on studying a martensite-based DP steel ($V_m=80\%>50\%$, V_m : volume fraction of martensite phase). Isolated ferrite phase is surrounding by net-work martensite phase. As described in **Chapter 1**, there are many factors[1-10] which can affect the mechanical properties of DP steels. Zhang et al., found that the low volume fraction of martensite in the DP steel improved strain hardening ability due to the soft ferrite phase in DP steel [2]. Paul used finite element method to study the martensite volume fraction effect and found that the band of stress triaxiality distribution will increase with increasing martensite volume fraction[9]. Many studies [11]on volume fraction change of martensite show the strength and ductility change in DP steels. However, the difference in the hardness ratio (M/F) change on the mechanical properties between ferrite-based DP steel ($V_m<50\%$) and martensite-based DP steel ($V_m>50\%$) has not been clarified yet. Therefore, in this chapter, the deformation behaviors in martensite-based DP steel and ferrite-based DP steel will be compared by changing the hardness ratio between martensite phase and ferrite phase.

4. 2. Experimental procedure

In this study, chemical composition of the steel is the same as it used in **Chapter 2**.

The chemical composition of the steel is presented in **Table 2.1**. In order to make ferrite-based DP specimens, heat treatment process used in this study is shown in **Fig. 4.1**.

4.1. A sheet 1 mm thick of the steel was homogenized at 950 °C (above A_3 temperature) for 1.8 ks, followed by air cooling to obtain a microstructure composed

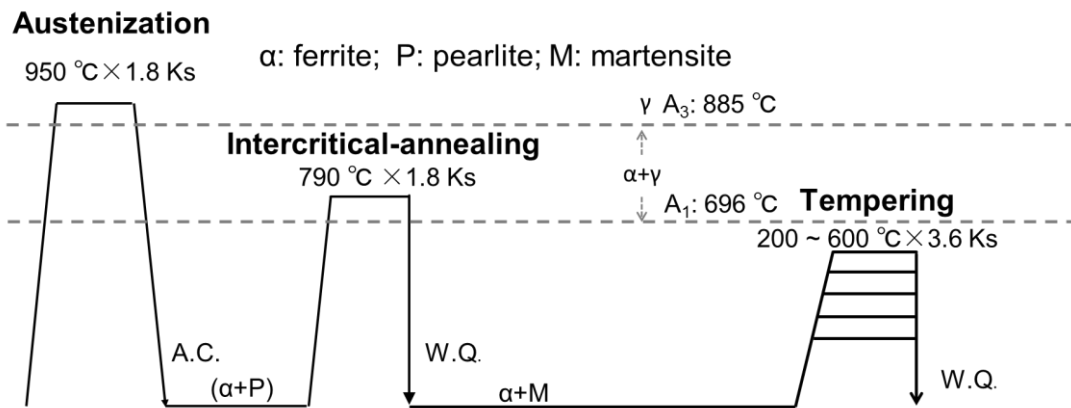


Fig. 4.1 Schematic illustration of the heat treatment process for preparing ferrite-base DP steels is used in this study.

of ferrite and pearlite. The sheet was then intercritically annealed at 790 °C (ferrite + austenite region) followed by water quenching to obtain a ferrite-based DP structure composed of martensite and ferrite, and then tempered at various temperatures ranging from 200 to 600 °C for 3.6 ks to change hardness of martensite and ferrite phases. All the heat treatments were carried out by a salt bath furnace. The microstructures of the specimens were observed by scanning electron microscopy (SEM, Jeol: JSM7800F) and

Electron Back-Scattered Diffraction (EBSD). For the microstructure observations, the specimens were polished mechanically by emery papers and then electrochemically in a 10 % perchloric acid solution (100 ml HClO_4 + 900 ml CH_3COOH). The polished surfaces were etched in a 3 % nital solution to distinguish martensite and ferrite phases. The volume fraction of martensite was measured by calculating the martensite area from low magnification (500X) SEM images. Tensile tests at an initial strain rate of $8.3 \times 10^{-4} \text{ s}^{-1}$ were conducted at room temperature. Tensile test specimens with a gauge length of 10 mm, width of 5 mm, and thickness of 1 mm were prepared from the heat-treated specimens by spark-cutting. Extensometer was used to measure tensile strain of the specimens. The extensometer was removed after the specimen was necked. The part of stress-strain curve after specimen necking was estimated by the crosshead travel. Nanohardness of the specimens were also measured by Nanoindentation test machine (Hysitron: TI 950 TriboIndenter) with a Berkovich indenter. The loading rate was $50 \mu\text{N s}^{-1}$, and the maximum load was 500 N. The nanohardness of martensite and ferrite phases were obtained within martensite and ferrite phase region, and the obtained values were averaged. Local strain on martensite phase and ferrite phase are measurement by DIC method which is the same as described in **Chapter 3**. The measurement of strain map by DIC method is shown in **Fig. 3.1**

4.3. Comparison of tempering temperature on microstructure evolution in martensite-based DP steel and ferrite-based DP steel

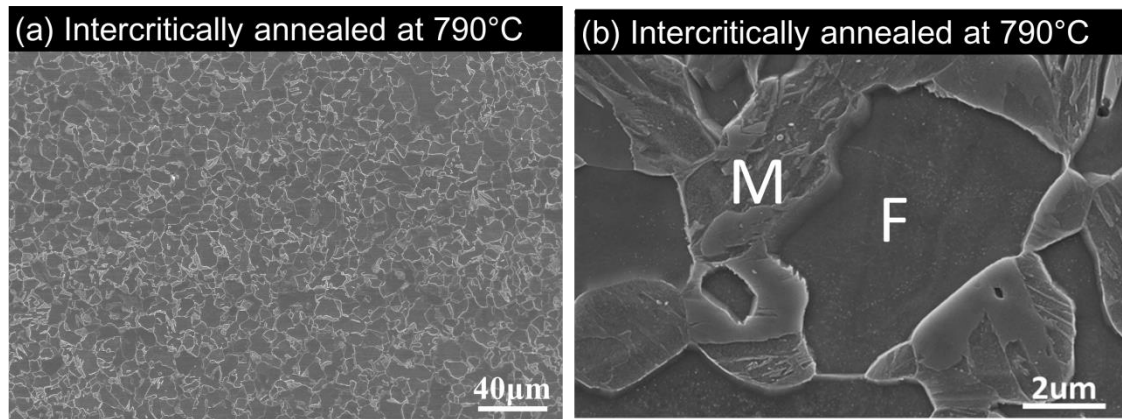


Figure 4.2 SEM images showing microstructures of the ferrite-based DP specimen intercritically annealed at 790 °C.

Figure 4.2 shows the SEM microstructures of the ferrite-based specimen intercritically annealed at 790 °C. The specimen was etched in a 3 % nital solution before SEM observation. Under the SEM observation, the specimen reveals net-work connected martensite and isolated ferrite structure (**Fig. 4.2a**). Ferrite phase shows a dark color and smooth surface, on the contrary martensite phase shows a relatively bright color and uneven surface (**Fig. 4.2b**). The volume fraction of martensite (V_m) was 29% , measured by calculating the martensite area using low magnification SEM images at 500 times. The morphology of net-work connected martensite and the volume

fraction of martensite were decided by isothermal intercritical annealing condition and intercritical annealing temperature.

Figure 4.3 shows EBSD boundary maps of ferrite-base DP steels ($V_m=29\%$) and martensite-base DP steels ($V_m=80\%$). In the grain boundary maps, the blue lines and red lines are indicating the high angle boundary ($\theta \geq 15^\circ$) and low angle boundary ($2^\circ \leq \theta < 15^\circ$), respectively. **Fig. 4.3a** shows ferrite-based DP steel intercritically annealed at 790°C . Martensite is recognized from its substructure and morphology. As can be seen, low angle boundaries indicated substructures are mainly distributed in martensite phase. **Fig. 4.3b** shows ferrite-based DP steel tempered at 400°C . From EBSD results, there is no significant difference from the intercritically annealed specimen shown in **Fig. 4.3a**. However, the ferrite-based DP steel tempered at 600°C show very less low angle boundaries in EBSD map, on the contrary, high angle boundaries increased in martensite phase (small grains in EBSD map). It is considered that recovery and recrystallization are appeared in martensite phase. **Fig. 4.3d** shows martensite-based DP steel intercritically annealed at 840°C . As can be seen, many low angle boundaries are distributed in martensite phase. **Fig. 4.3e** shows martensite-based DP steel tempered at 400°C . From EBSD results, there is no significant difference from the intercritically annealed specimen shown in **Fig. 4.3a**.

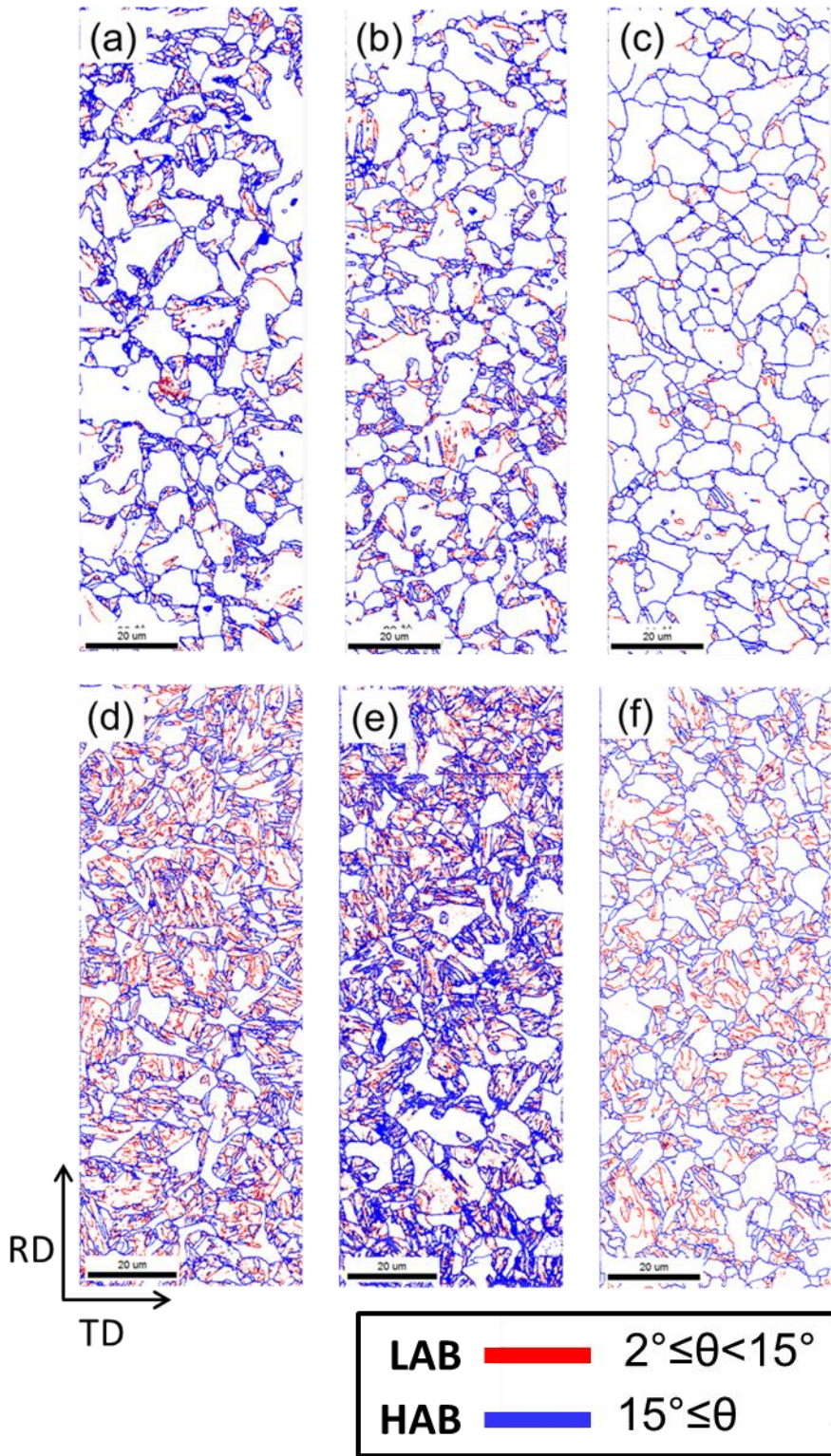


Figure 4.3 EBSD boundary maps of the ferrite-based DP steel specimens intercritically annealed at 790 °C and subsequently tempered at various temperatures for 3.6 Ks. (a)

intercritically annealed at 790 °C, and subsequently (b) tempered at 400 °C, (c) tempered at 600 °C. EBSD boundary maps of the martensite-based DP steel specimens intercritically annealed at 840 °C and subsequently tempered at various temperatures for 3.6 Ks. (d) intercritically annealed at 840 °C, and subsequently (e) tempered at 400 °C, (f) tempered at 600 °C. LAB and HAB are representing low angle boundaries with misorientation of 2-15° drawn in red lines and high angle boundaries with misorientation above 15° drawn in blue lines, respectively.

That indicates that the substructures are still remaining until tempered at 400 °C.

However, the martensite-based DP steel tempered at 600 °C shown in **Fig. 4.3f** show some high angle boundaries appear in martensite phase, however, there are still many low angle boundaries in martensite phase.

4.4 Comparison of tempering temperature on microstructure evolution

4.4.1 Nanohardness change of martensite and ferrite phases:

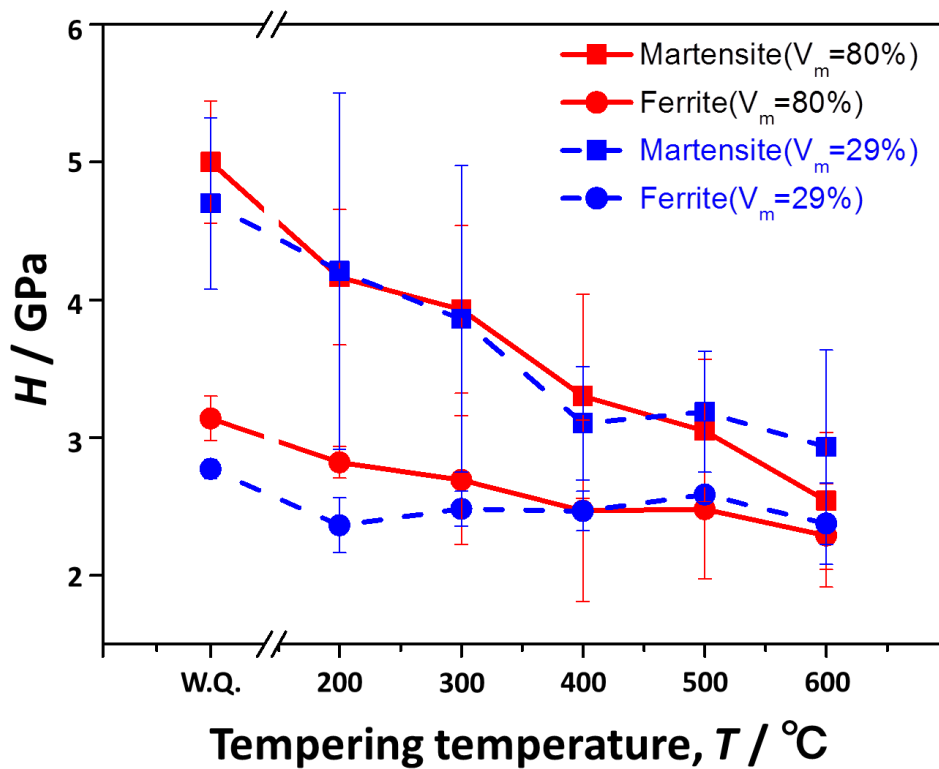


Figure 4.4 Tempering temperatures as a function of nanohardness values of martensite and ferrite in ferrite-based DP steels ($V_m=29\%$) and martensite-based DP steels ($V_m=80\%$).

Figure 4.4 Tempering temperatures as a function of nanohardness values of martensite and ferrite. For ferrite-based DP steel, blue curves represent nanohardness results of ferrite and martensite phases. The scattering of hardness in martensite is basically larger than that in ferrite. This is possibly because several boundaries inside the

martensite structure, such as lath boundaries, block boundaries, and packet boundaries, could affect the nanohardness of martensite measured within a small volume. It is found that with increasing the tempering temperature, the nanohardness of martensite decreased and then almost keeps constant tempered at 400-600 °C. The nanohardness of ferrite phase was first decrease, and then keeps constant with increasing tempering temperature. For intercritically annealed specimens, nanohardness of ferrite phase in ferrite-based DP steel specimen is smaller than martensite-based DP steel specimen. It is probably because the volume fraction of martensite phase in ferrite-based DP steel is less than martensite-based DP steel. A fewer amounts of dislocations generated in ferrite phase in ferrite-based DP steel during martensite transformation (from austenite transformed into martensite).

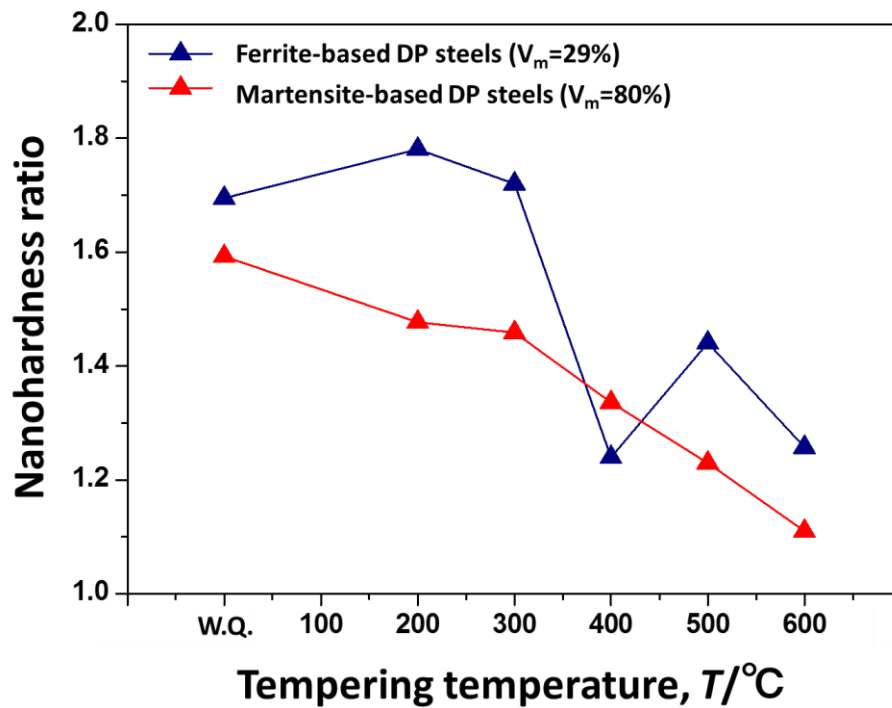


Figure 4.5 Tempering temperatures as a function of nanohardness ratio between martensite and ferrite in ferrite-based DP steels and martensite-based DP steels.

Figure 4.5 shows the relationship about tempering temperatures as a function of nanohardness ratio (M/F) in ferrite-based DP steels and martensite-based DP steels. In ferrite-based DP steels, nanohardness ratio first increase with tempering the specimen at 200 °C, and then decreased at 400 °C. The relationship between the nanohardness ratio and the tempering temperature in ferrite-based DP steels show non-linear relationship compared with the martensite-based DP steels.

4.4.2 Stress-strain behaviors

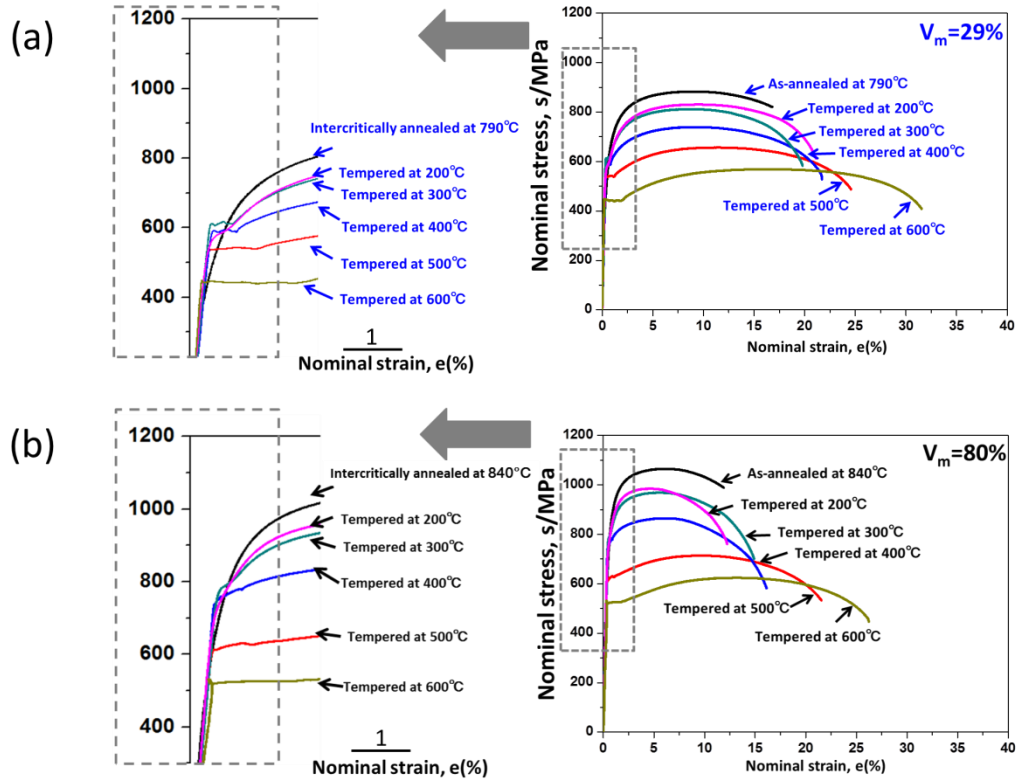


Figure 4.6 Stress-strain curves of specimens (a) ferrite-based DP steels, (b) martensite-based DP steels.

Figure 4.6 shows stress-strain curves of ferrite-based DP steel specimens (**Fig. 4.6a**) and martensite-based DP steel specimens (**Fig. 4.6b**). For the yielding behavior, the specimens change from continuous yielding into discontinuous yielding after tempering in both ferrite-based DP steel specimen and martensite-based DP steel specimen. Tensile strength was decreased with increasing tempering temperature in all kinds of DP steel specimens. However, in ferrite-based DP steel specimens, the Lüders deformation strain are larger and yield drops are sharper than in martensite-based DP steel specimens.

According to the phase map shown in **Fig. 1.3** in **Chapter 1**, the carbon content in martensite phase is higher in ferrite-based DP steel specimens. More carbide will appear in martensite phase in ferrite-base DP steel specimens, which will pin the mobile dislocations results in Lüders deformation and sharp upper yield point.

4.4.3 Effect of tempering temperature on strength and elongation.

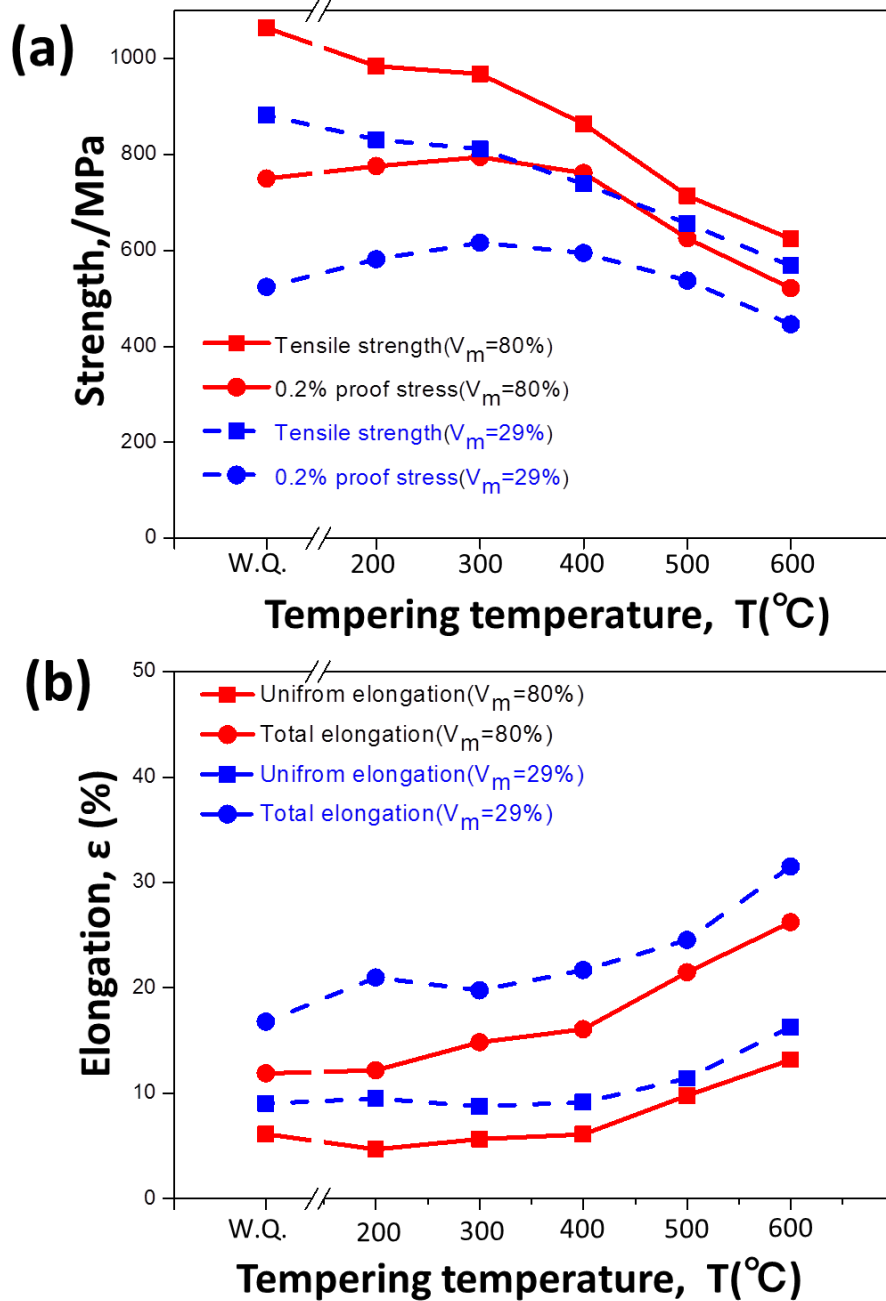


Figure 4.7 The strength and elongation plotted as a function of tempering temperature.

(a) 0.2% proof stress and ultimate tensile strength plotted as a function of tempering

temperature. (b) Uniform elongation and total elongation plotted as a function of tempering temperature.

Fig. 4.7a summarizes the change of strength (0.2% proof stress and ultimate tensile strength) as a function of tempering temperature. For both ferrite-based DP steel specimens and martensite-based DP steel specimens, it is found that the ultimate tensile strength monotonously decreased with increasing the tempering temperature. On the other hand, the 0.2% proof stress firstly increased a little bit by tempering at temperatures below 300 °C, and then decreased above 300 °C. The increase of 0.2% proof stress by tempering at temperatures below 300 °C is presumably because precipitated carbides pinned mobile dislocations in martensite phase. After further tempering above 300 °C, the coarsening of carbides and martensite led to the decrease of 0.2% proof stress. The difference between the two kinds of DP steel specimens is ferrite-based DP steel specimens having lower tensile strength and 0.2% proof stress (yield strength) than martensite-based DP steel specimens. **Fig. 4.7b** shows the change of elongation, i.e., uniform elongation and total elongation, as a function of tempering temperature. With increasing the tempering temperature, the total elongation monotonously increased in two kinds of DP steel specimens. On the other hand, the uniform elongation did not change so much after tempering at temperature below

400 °C, while it quickly increased above 400 °C in two kinds of DP steel specimens. The difference between the two kinds of DP steel specimens is that ferrite-based DP steel specimens having larger elongations (uniform elongation and total elongation) than martensite-based DP steel specimens at the same tempering temperature condition.

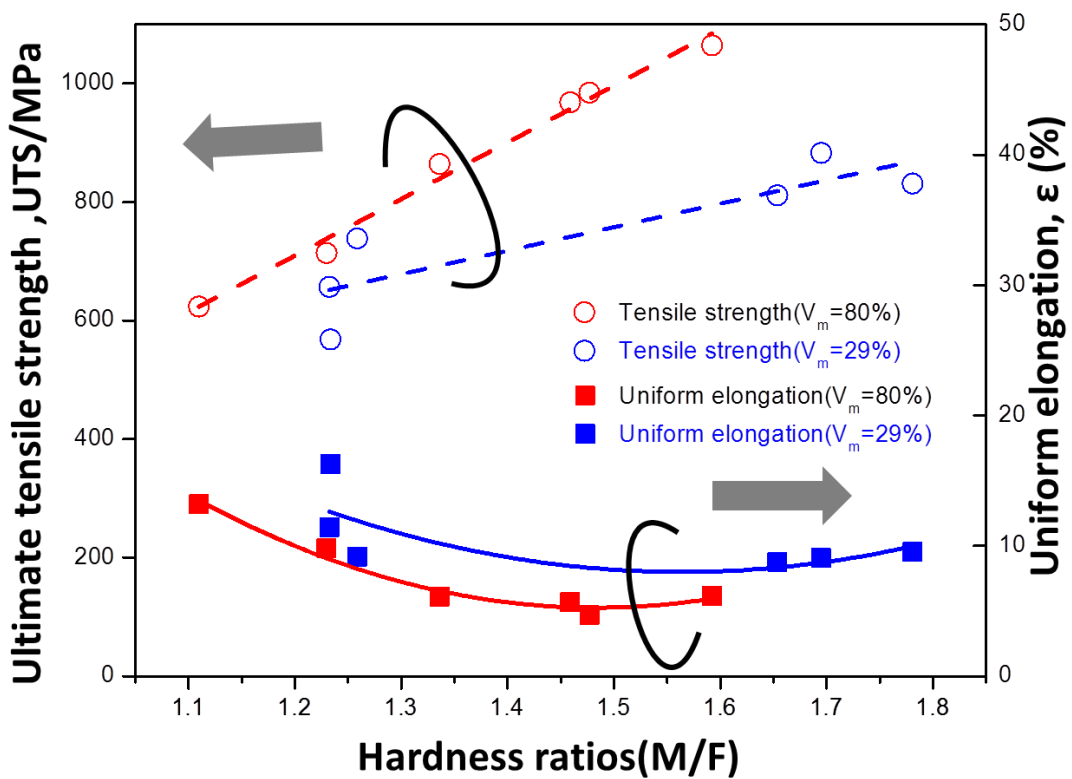


Figure 4.8 Ultimate tensile strength and uniform elongation in the DP steels summarized as a function of the nanohardness ratio. The dash lines are linear fitting curves for ultimate tensile strength, and the solid curves are non-linear fitting curves for uniform elongation.

Figure 4.8 shows the ultimate tensile strength and uniform elongation in the DP steels

summarized as a function of the nanohardness ratio. In the ferrite-based DP steels ($M/F < 1.3$), with increasing ultimate tensile strength, the uniform elongation decrease shows tradeoff relationship. Similar to the martensite-based DP steels, with further increase the ultimate tensile strength, the uniform elongation maintained in ferrite-based DP steels. The slope of strength fitting curve in martensite-based DP steels is larger than it in ferrite-based DP steels. That indicated that, with increase nanohardness ratio, the ultimate tensile strength in martensite-based DP steel increase faster than the strength in ferrite-based DP steel.

4.5 Effect of hardness ratio between two phases on deformation behavior in ferrite-based dual phase steel

In order to understand the deformation behavior of martensite phase and ferrite phase in ferrite-based DP steels, specimen A (M/F=1.23), specimen B (M/F=1.26) and specimen C (M/F=1.69) are selected to investigate.

4.5.1 Strain partitioning in specimen A (M/F=1.23)

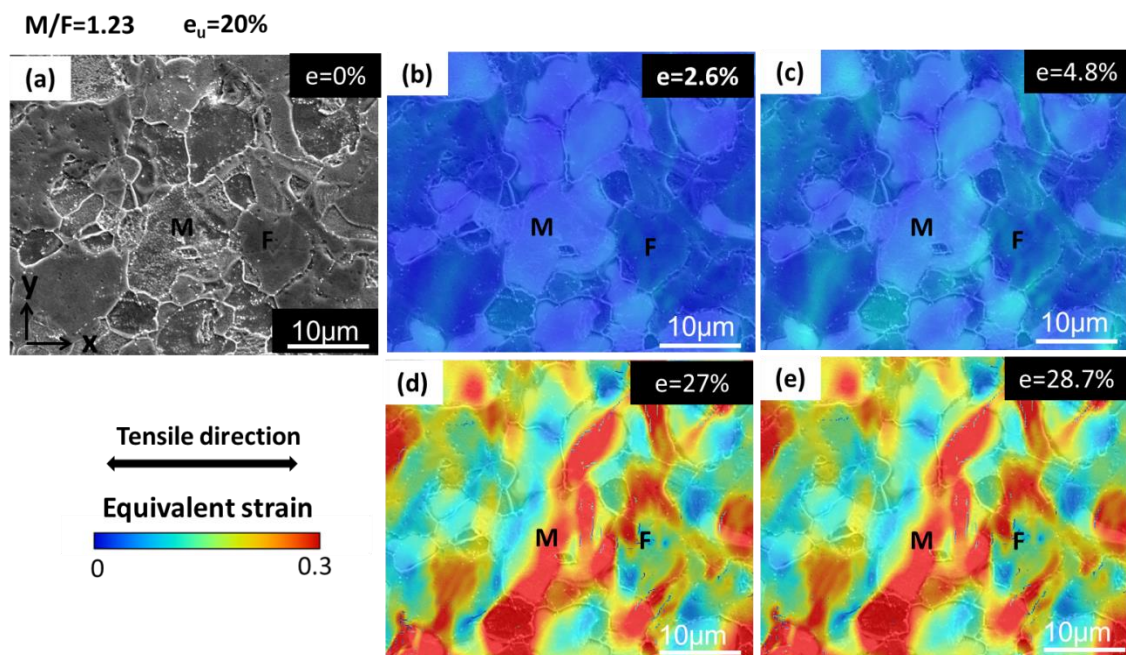


Figure 4.9 Strain maps of specimen A tensile deformed (b) $e=2.6\%$, (c) 4.8% , (d) 27% and (e) 28.7% . (a) SEM image of specimen A before deformation. “M”, “F” represent martensite phase and ferrite phase, respectively. The uniform elongation of specimen A is 20% . Tensile direction is in horizontal direction.

Figure 4.9 shows the strain maps of specimen A tensile deformed at 2.6% , 4.8% , 27% ,

and 28.7%. **Fig. 4.9a** is the SEM image of specimen A without deformation. Tensile direction is in horizontal direction. The red color in strain map represent high strain and blue color in strain map represent low strain. The morphology of high strain in strain maps is showing line-like morphology. The spread direction of the line-like high strain is inclined to the tensile direction at an angle of about 45 degrees.

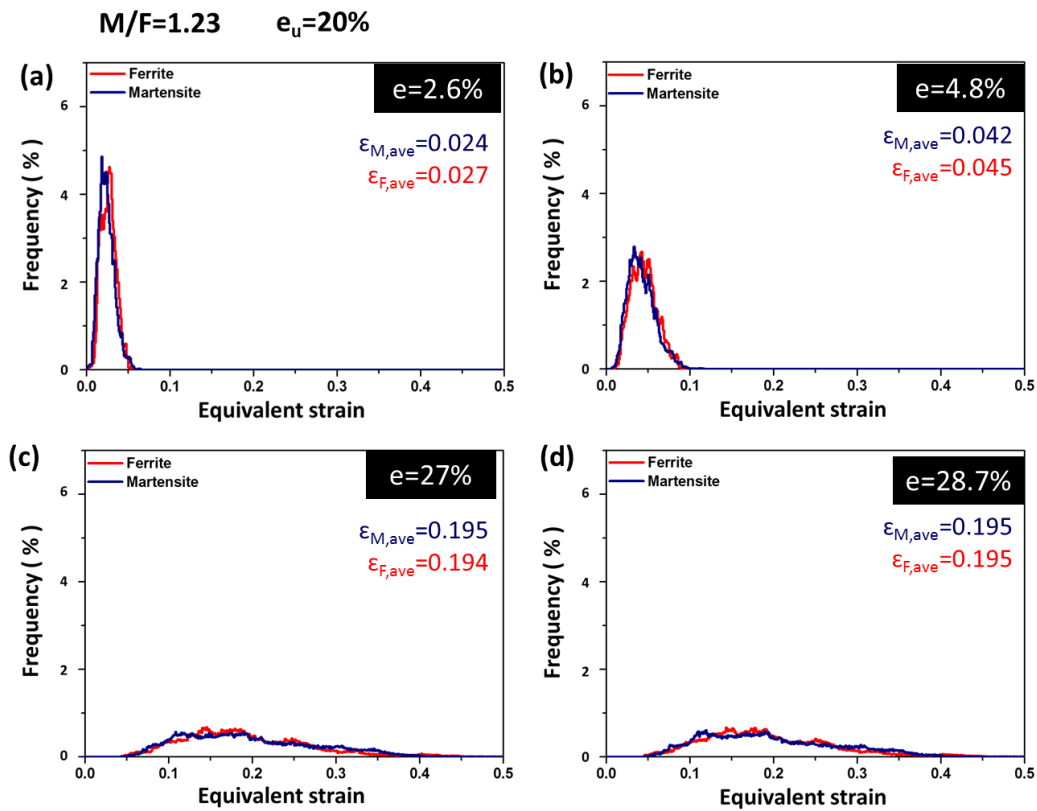


Figure 4.10 Local strain distribution in ferrite phase and martensite phase obtained from strain maps in **Fig .4.9.**. The local strain distributed in martensite phase and ferrite phase are separated. The uniform elongation of specimen A is 20%. The bin size of the distribution is an equivalent strain of 0.001.

Figure 4.10 shows Local strain distribution in ferrite phase and martensite phase obtained from strain maps in **Fig .4.9.** The local strain distributed in martensite phase and ferrite phase are separated and plotted as histograms into blue curve and red curve, respectively. The average local strain in martensite phase ($\epsilon_{M,ave}$) and ferrite phase ($\epsilon_{F,ave}$) are both increased with increasing tensile strain. In addition, the strain distributions of ferrite and martensite are too close to each other. Both high strain region and low strain region in ferrite phase and martensite phase are shifted into larger strain level. This indicates that the deformation in martensite phase and in ferrite phase is relatively homogeneous.

4.5.2 Strain partitioning in specimen B (M/F=1.26)

M/F=1.26 $e_u=12.1\%$

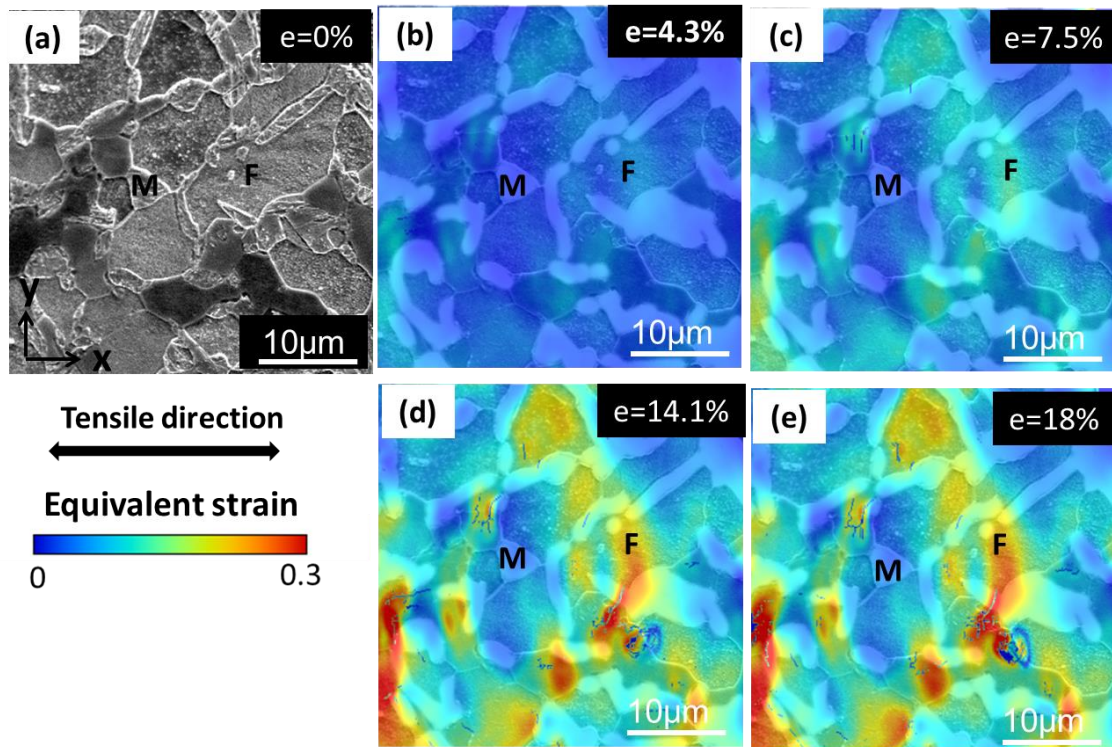


Figure 4.11 Strain maps of specimen B tensile deformed (b) $e=4.3\%$, (c) 7.5% , (d) 14.1% and (e) 18% . (a) SEM image of specimen B before deformation. “M”, “F” represent martensite phase and ferrite phase, respectively. The uniform elongation of specimen B is 12.1% . Tensile direction is in horizontal direction.

Figure 4.11 shows the strain maps of specimen b tensile deformed at 4.3% , 7.5% , 14.1% and 18% . **Fig. 4.11a** is the SEM image of specimen B without deformation. The red color in strain map represent high strain and blue color in strain map represent low strain. Tensile direction is in horizontal direction. From strain maps shown in **Fig. 4.11 (b-e)**, the high strain color (yellow and red color) increase with increasing

tensile strain. On the other hand, the low strain color (blue color) decreases with increasing tensile strain. The morphology of high strain in strain maps is showing strip-like morphology.

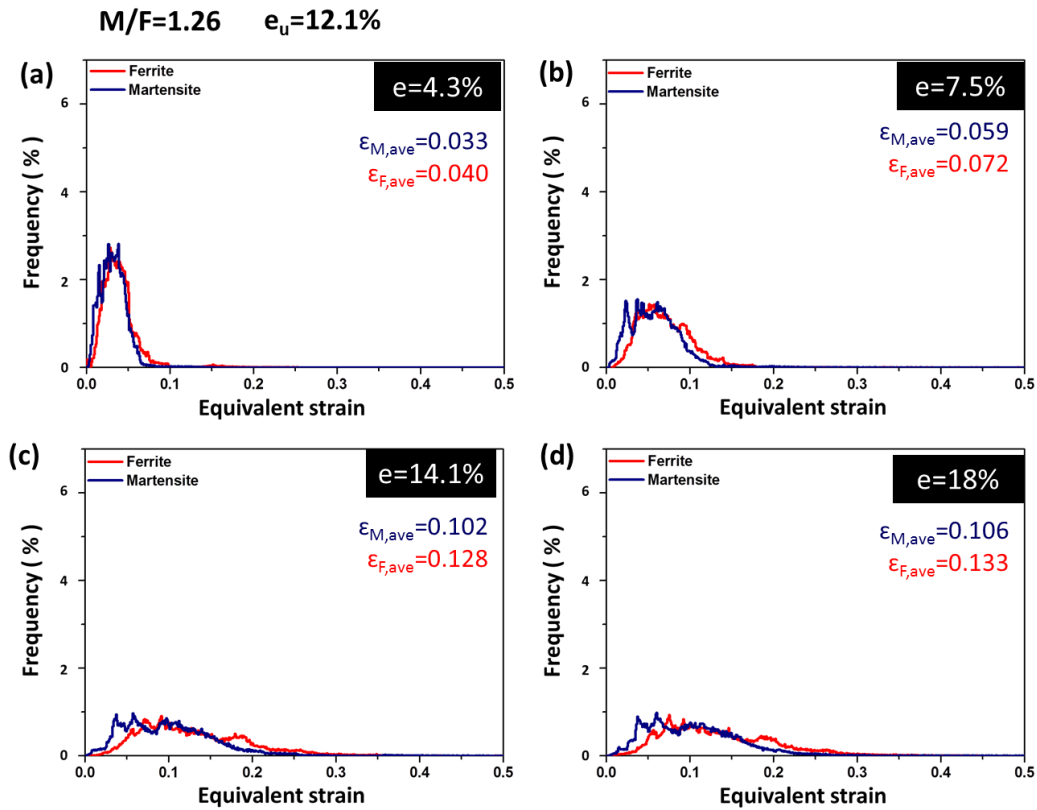


Figure 4.12 Local strain distribution in ferrite phase and martensite phase obtained from strain maps in **Fig .4.11**. The local strain distributed in martensite phase and ferrite phase are separated. The uniform elongation of specimen B is 12.1%. The bin size of the distribution is an equivalent strain of 0.001.

Figure 4.12 shows Local strain distribution in ferrite phase and martensite phase obtained from strain maps in **Fig .4.11**. The local strain distributed in martensite phase and ferrite phase are separated and plotted as histograms into blue curve and red curve, respectively. The average local strain in martensite phase ($\epsilon_{M,ave}$) and ferrite phase

($\epsilon_{F,ave}$) are both increased with increasing tensile strain before specimen necking. During deformation ($e=7.5\%$ to $e=14.1\%$), just after specimen necking (**Fig. 4.12(b-c)**), the low strain region in martensite and ferrite phase is still located in the small strain region, while the high strain region in martensite and ferrite is shifted into larger strain level. This indicates that the deformation in martensite phase and in ferrite phase is relatively inhomogeneous.

4.5.3 Strain partitioning in specimen C (M/F=1.69)

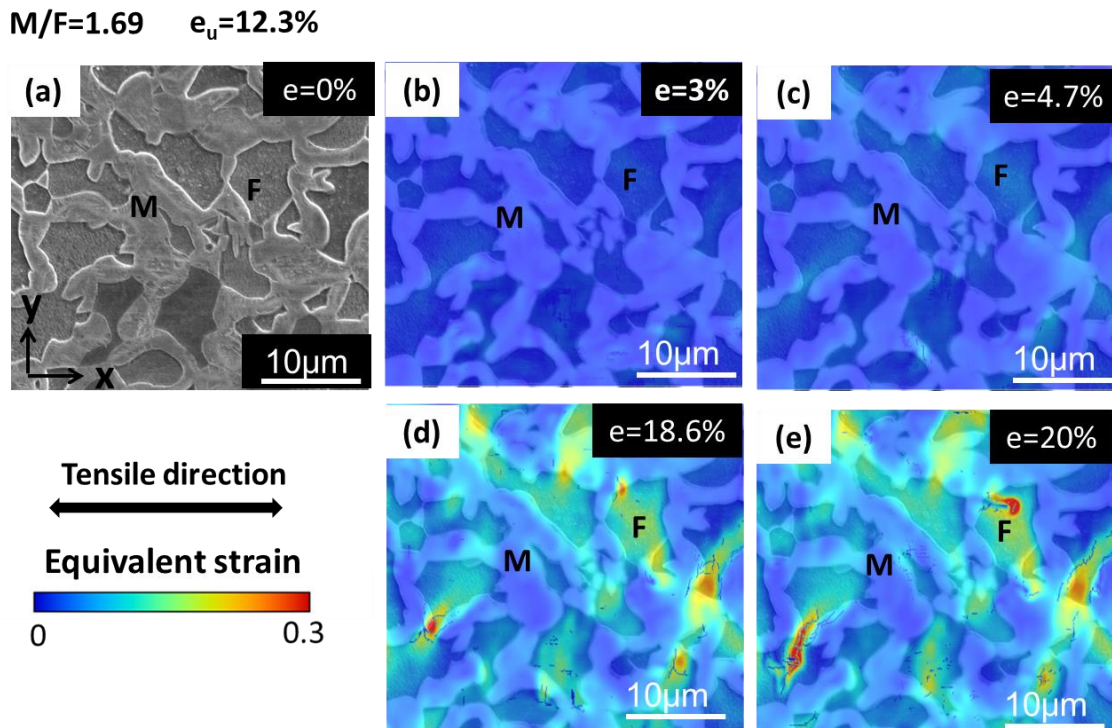


Figure 4.13 Strain maps of specimen C tensile deformed (b) $e=3\%$, (c) 4.7% , (d) 18.6% (e) 20% . (a) SEM image of specimen C before deformation. “M”, “F” represent martensite phase and ferrite phase, respectively. The uniform elongation of specimen B is 12.3% . Tensile direction t is in horizontal direction.

Figure 4.13 shows the strain maps of specimen C tensile deformed at 3%, 4.7%, 18.6% and 20%. **Fig. 4.13a** is the SEM image of specimen C without deformation. Tensile direction is in horizontal direction. The red color in strain map represent high strain and blue color in strain map represent low strain. From strain maps shown in **Fig. 4.13 (b-e)**, the high strain color (yellow and red color) increase with increasing tensile strain. On the other hand, the low strain color (blue color) decreases with increasing tensile strain. The morphology of high strain in strain maps is showing strip-like morphology.

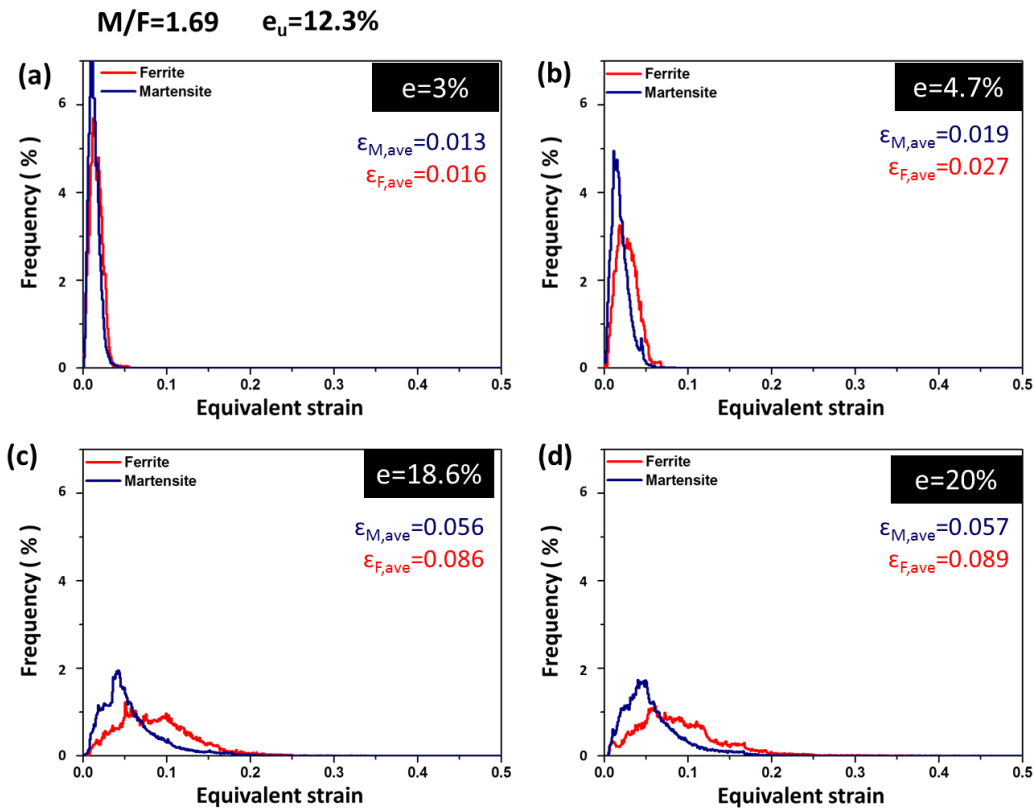


Figure 4.14 Local strain distribution in ferrite phase and martensite phase obtained

from strain maps in **Fig .4.14**. The local strain distributed in martensite phase and ferrite phase are separated. The uniform elongation of specimen C is 12.3%. The bin size of the distribution is an equivalent strain of 0.001.

Figure 4.14 shows Local strain distribution in ferrite phase and martensite phase obtained from strain maps in **Fig .4.13**. The local strain distributed in martensite phase and ferrite phase are separated and plotted as histograms into blue curve and red curve, respectively. The average local strain in martensite phase ($\epsilon_{M,ave}$) and ferrite phase ($\epsilon_{F,ave}$) are both increased with increasing tensile strain before specimen necking. In addition, at the beginning of tensile deformation ($e=3\%$) (**Fig. 4.14a**), it can be seen both high strain region and low strain region are distributed in ferrite phase and martensite. With further deformation ($e=4.7\%$ to $e=18.6\%$), just after specimen necking (**Fig. 4.14(b-c)**), the low strain region in martensite and ferrite phase is still located in the small strain region, while the high strain region in martensite and ferrite is shifted into larger strain level. This indicates that the deformation in martensite phase and in ferrite phase is relatively inhomogeneous.

4.5.4 Comparison of the deformation behaviors of specimens with different hardness ratios

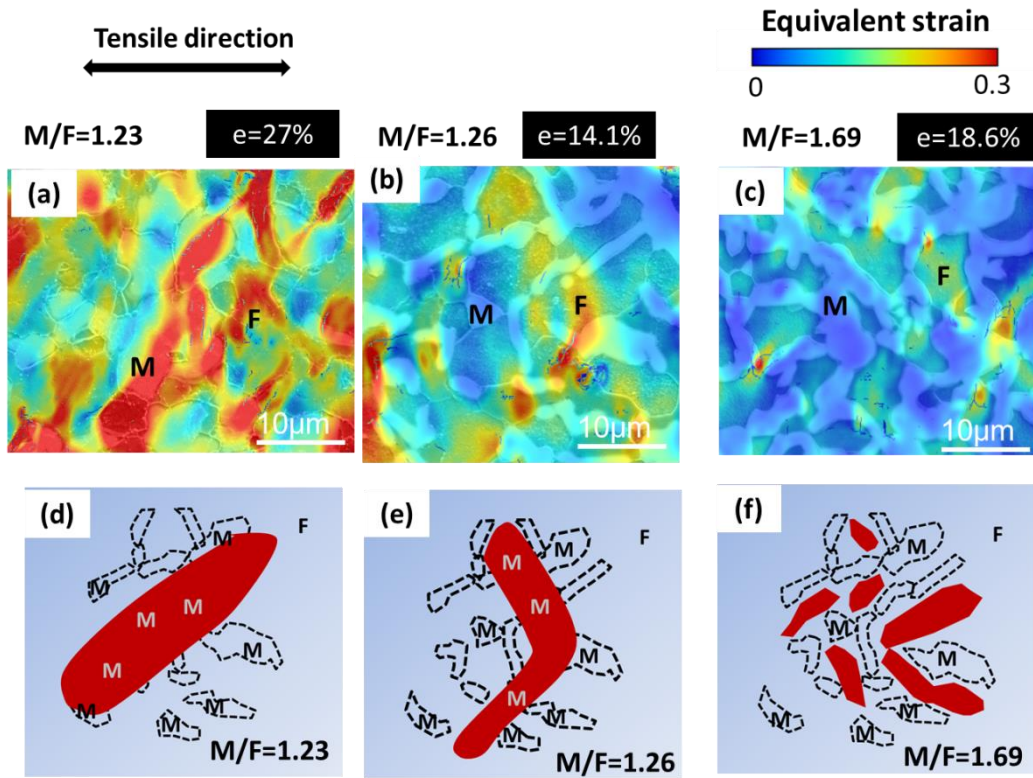


Figure 4.15 Strain maps of the specimens after necking and the illustrations of high strain in specimens A (M/F=1.23), B (M/F=1.26) and C (M/F=1.69). (a) Strain map of specimen A tensile deformed at 27%, (b) strain map of specimen B tensile deformed at 14.1%, (c) strain map of the specimen C tensile deformed at 18.6% , (d) high strain in specimen A shows line-like morphology, (e) high strain in specimen B shows strip-like morphology, and (f) high strain in specimen C shows strip-like morphology. “M”, “F” represent martensite phase and ferrite phase, respectively.

Figure 4.15 shows strain maps of the specimens after necking and the illustrations of high strain in specimens A (M/F=1.23), B (M/F=1.26) and C (M/F=1.69). **Fig. 4.15a** shows strain map of specimen A tensile deformed at 27%. The hardness ratio between

martensite and ferrite phase in specimen A is small ($M/F=1.23$). The high strain shows line-like morphology in the strain map of specimen A shown in **Fig. 4.15a**. It can be seen the line-like high strain propagates through martensite phase and ferrite phase without considering the phase's type. **Fig. 4.15b** shows the strain map of the specimen B. Compared with specimen A ($M/F=1.23$), the hardness ratio (M/F) between martensite phase and ferrite phase in specimen B ($M/F=1.26$) become larger, which indicate martensite become harder. The high strain still can propagate through martensite, though the hardness ratio increase. However, the high strain somehow constrained in ferrite. And the high strain in specimen B shows strip-like morphology in the strain map shown in **Fig. 4.15b**. With further increase the hardness ratio (M/F), the martensite phase becomes much harder. **Fig. 4.15c** shows the strain map of specimen C ($M/F=1.59$), the hard martensite phase constrained the high strain in ferrite phase region. The high strain shows strip-like morphology, and the high strain tends to connect with each other.

4.5.5 Comparison of the deformation behaviors of specimens in ferrite-based DP steels and martensite-based DP steels with different hardness ratios

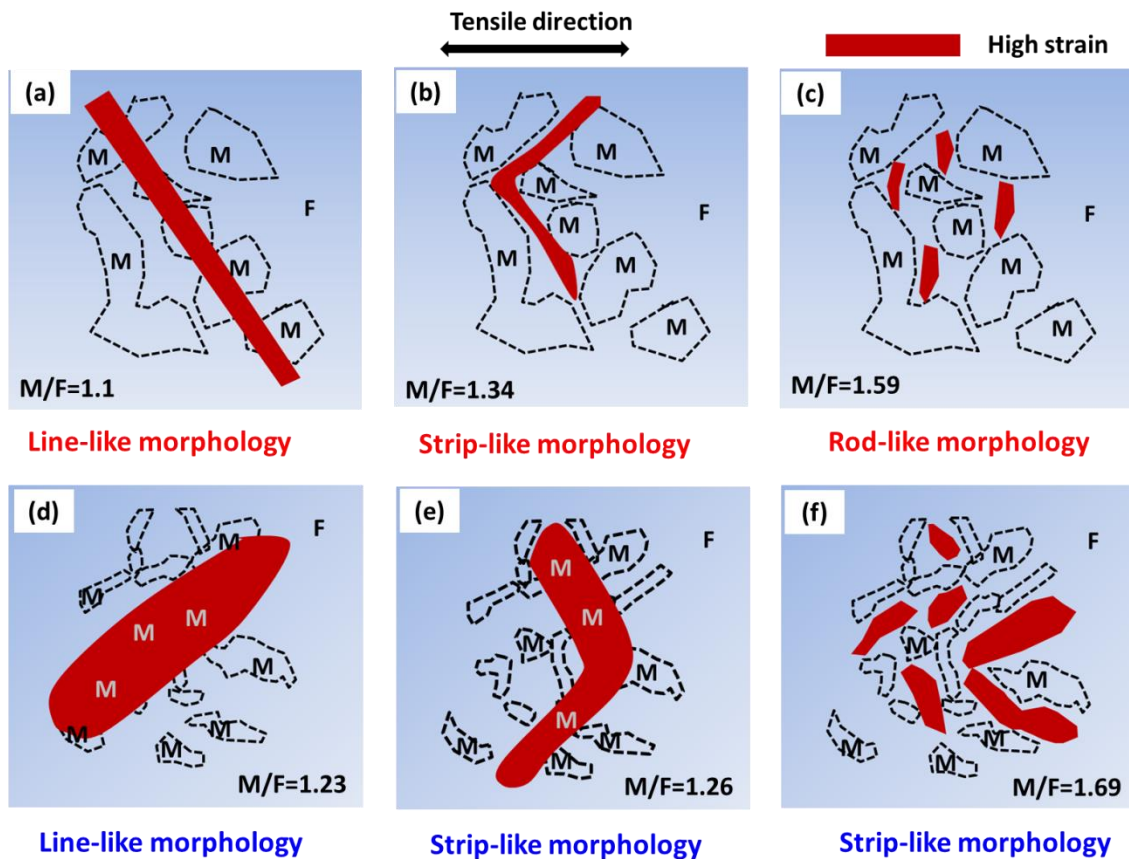


Figure 4.16 Schematic illustrations showing the high strain in martensite-based DP steels with (a) $M/F=1.1$, (b) $M/F=1.34$ and (c) $M/F=1.59$. High strain in ferrite-based DP steels with (a) $M/F=1.23$, (b) $M/F=1.26$ and (c) $M/F=1.69$. Red color represents high strain.

Figure 4.16 showing the high strain in martensite-based DP steels and ferrite-based DP steels with various hardness ratios. As can be seen in Fig. 4.16a and **Fig. 4.16d**, the high strain shows line-like morphology through martensite and ferrite in low hardness

ratio specimens. Increase the hardness ratio (M/F), the line-like high strain is blocked by hard martensite phase showing strip-like morphology in **Fig. 4.16(b-e)**. However, in **Fig. 4.16e**, high strain can go through martensite due to the hardness difference between martensite and ferrite is not large. With further increase the hardness ratio, the high strain is constrained in ferrite phase. In martensite-based DP steel shown in **Fig. 4.16c**, the high strain shows rod-like morphology, separate by hard martensite. However, the high strain in ferrite-based DP steel shown in **Fig. 4.16f** show a higher hardness ratio than martensite-based specimen in **Fig. 4.16c**. However, the high strain in ferrite-based DP steel shows strip-like morphology. It might be because in ferrite-based DP steel, ferrite space is larger than martensite-based DP steel, the high strain in ferrite-based DP steel can have space to propagate, hence, showing strip-like morphology. On the other hand, the high strain in martensite-based DP steel is constrained in small ferrite space, hence, showing rod-like morphology.

4.6 Discussion

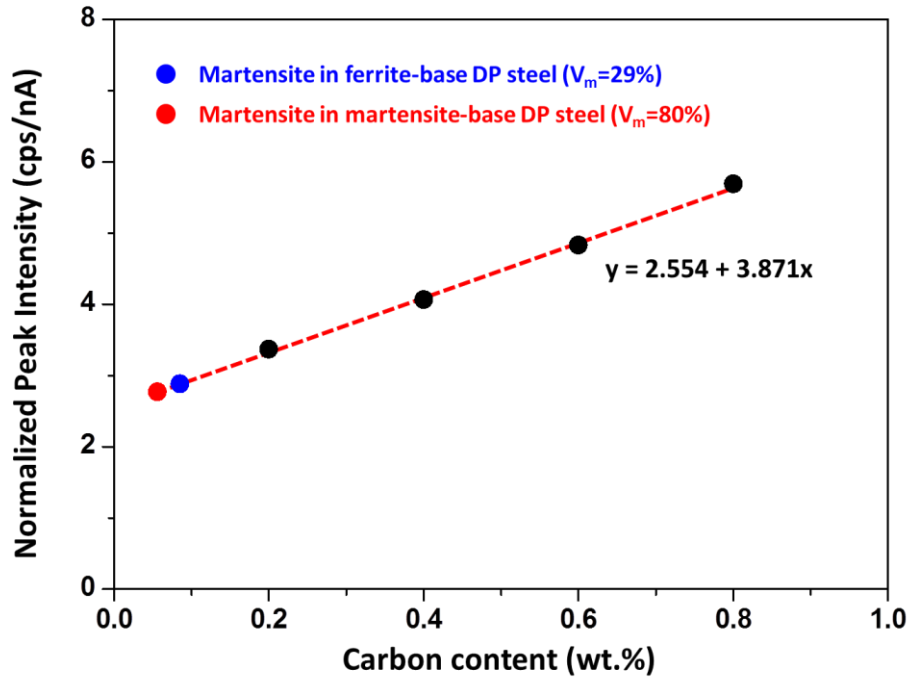


Figure 4.17 shows the wavelength dispersive spectrometer (WDS) method to estimate the carbon content in martensite phase. Dash line is liner fitting curve.

Figure 4.17 shows the wavelength dispersive spectrometer (WDS) method to estimate the carbon content in martensite phase. WDS measurement were carried out under voltage 15kv, current 12.43nA, measured 200s. Considering the accuracy of WDS measurement, all specimens were measured under magnification of 1000 times. First, full martensite specimens of Fe_{0.2}C, Fe_{0.4}C, Fe_{0.6}C and Fe_{0.8}C were prepared by annealing at 950 °C for 1.8ks followed by water quenching. Linear fitting curve was obtain by fit the full martensite specimens. By measuring the peak intensity of

martensite phase in DP steel, carbon content in martensite phase was estimate by equation of linear fitting curve. The carbon content in martensite estimated ferrite-based DP steel specimen and martensite-based DP steel specimen are 0.085 and 0.056, respectively. However, it should point out that the martensite carbon content measured in ferrite-based DP steel specimen contain part of ferrite phase. It is because the phase size of martensite in ferrite-base DP steel specimen is smaller than the size of focal point. Even that the carbon content of martensite in ferrite-based DP steel specimen is higher than the carbon content of martensite in martensite-based DP steel specimen. This might be the reason why the hardness ratio is higher in ferrite-based DP steel after intercritical annealing (M/F=1.69) than in martensite-based DP steel after intercritical annealing (M/F=1.59).

Figure 4.18 shows average phase strain in martensite phase and ferrite phase in ferrite-based DP steel (M/F=1.69) and martensite-based DP steel (M/F=1.59). It can be seen, two specimen tensile deformed similar tensile strain, strain ratio(ϵ_F/ϵ_M) in martensite-based DP steel shows higher value than strain ratio in ferrite-based DP steel. However, the strain ratio in martensite-based DP steel ($\epsilon_F/\epsilon_M=1.55$) in higher than in ferrite-based DP steel($\epsilon_F/\epsilon_M=1.42$). As discussed in Chapter 3, larger strain ratio

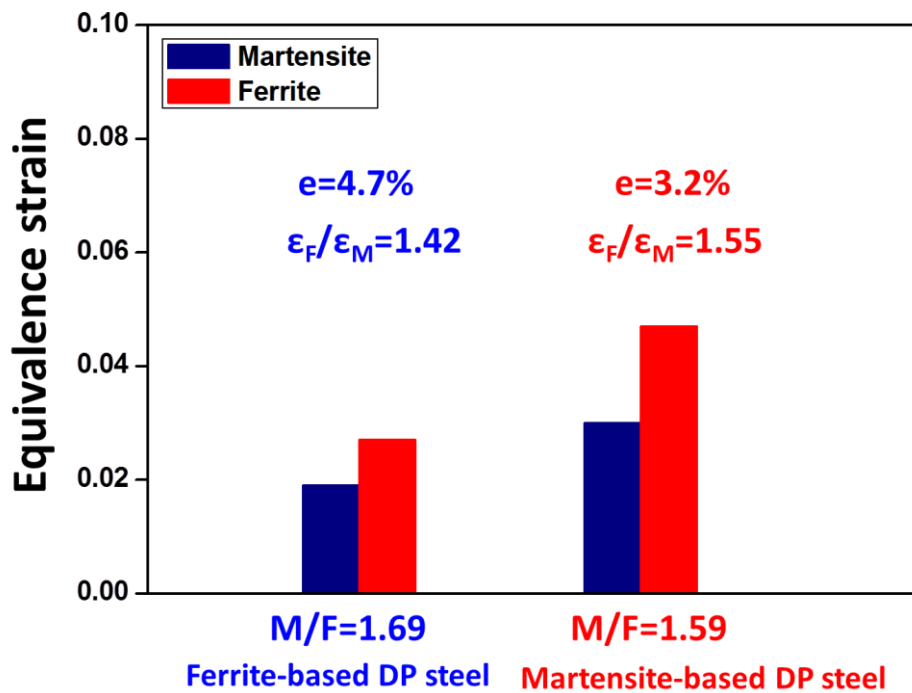


Figure 4.18 Average phase strain in martensite phase and ferrite phase in martensite-based DP steel and ferrite-based DP steel.. ϵ_F/ϵ_M : strain(average phase strain) ratio between ferrite phase and martensite phase;

between ferrite and martensite will generate a larger compatibility stress to keep the strain change continuously between two phases (because two phases are connected by interphase boundary). This large compatibility stress will enhance the strain hardening. So the martensite-based DP steels show a higher strain hardening ability than the specimen in ferrite-based DP steels with a similar hardness ratio.

4. 7 Conclusions

In Chapter 4, Comparison of the deformation behaviors in martensite based DP steel ($V_m=80\%$, V_m :Volume fraction of martensite) and ferrite based DP steel($V_m=29\%$) with various hardness ratios between martensite and ferrite. The main results are summarized as follows:

1. EBSD results show more low angle boundaries ($2^\circ < \Theta < 15^\circ$) in martensite-based DP steel. The specimen tempered at 600°C , low angle boundaries in ferrite based DP steel are almost disappeared and martensite phase with high angle boundaries ($\Theta \geq 15^\circ$) show recrystallized structure in ferrite-based DP steel. In ferrite-based DP steel, the tensile strength not linear decrease with reducing nanohardness ratios (M/F). The uniform elongation change in ferrite-based DP steel shows a similar tendency with the nanohardness ratio change in martensite-based DP steel.

2. The local strain distribution in martensite phase and ferrite phase in ferrite-based DP steel show similar tendency as it shown in martensite based DP steel shown in **Chapter3**. The morphology of high strain in ferrite based DP steel specimens show strip-like morphology and line-like morphology.in high hardness ratio specimen and low hardness ratio specimen.

3. Under similar hardness ratio specimen in ferrite-based DP steel and martensite based

DP steel, the strain ratio in martensite-based DP steel is higher than ferrite-based DP steel. It is suggest that the strain hardening ability in martensite-based DP steel is higher than ferrite-based DP steels with the similar hardness ratio between martensite phase and ferrite phase.

Reference

- [1] J. Zhou, A.M. Gokhale, A. Gurumurthy, S.P. Bhat, *Mat Sci Eng a-Struct*, 630 (2015) 107-115.
- [2] J. Zhang, H. Di, Y. Deng, R.D.K. Misra, *Mat Sci Eng a-Struct*, 627 (2015) 230-240.
- [3] M. Zaeimi, A. Basti, M. Alitavoli, *J Mater Eng Perform*, 24 (2015) 1781-1789.
- [4] S.K. Paul, N. Stanford, T. Hilditch, *Mat Sci Eng a-Struct*, 638 (2015) 296-304.
- [5] Q. Lai, O. Bouaziz, M. Goune, L. Brassart, M. Verdier, G. Parry, A. Perlade, Y. Brechet, T. Pardoën, *Mat Sci Eng a-Struct*, 646 (2015) 322-331.
- [6] M. Turkmen, S. Gunduz, *Acta Metall Sin-Engl*, 27 (2014) 279-289.
- [7] T. Matsuno, D. Maeda, H. Shutoh, A. Uenishi, M. Suehiro, *Isij Int*, 54 (2014) 938-944.
- [8] A. Ghaheri, A. Shafyei, M. Honarmand, *Mater Design*, 62 (2014) 305-319.
- [9] S.K. Paul, *Mater Design*, 50 (2013) 782-789.
- [10] M.R. Akbarpour, A. Ekrami, *Mat Sci Eng a-Struct*, 477 (2008) 306-310.
- [11] A. Saai, O.S. Hopperstad, Y. Granbom, O.G. Lademo, *Procedia Materials Science*, 3 (2014) 900-905.

Chapter 5: Microstructure and mechanical properties of dual phase Cu-Zn alloy composed of soft and hard phases

5.1. Introduction

Dual phase (DP) alloy has a microstructure consist of soft phase and hard phase shows a good balance of strength and ductility. The DP alloy can be simply classified as ferrous DP alloy and non-ferrous DP alloy. In ferrous DP alloy, as described in previous chapters, DP steel composed of soft ferrite phase and hard martensite phase exhibits a high tensile strength and a good elongation [1]. As described in **Chapter 1**, many factors such as grain sizes[2-9], volume fraction of second phase[10, 11] and constituent phases morphology[12, 13] have been studied to investigate the mechanical properties of DP steels. In addition, some DP steels have retained metastable austenite phase, retained metastable austenite phase will transform into martensite phase during plastic deformation [14-16]. The tensile strength is enhanced by strain hardening. This effect is called “TRIP” effect, which stand for Transformation Induced Plasticity. Shen et al.[15] studied the retained austenite morphology on strength and ductility. Their results showed lamellar retained austenite is the guiding microstructure component responsible for the higher mechanical stability, compared to the blocky one.

Lee et al.[16] studied the volume fraction and stability of retained austenite on formability in DP steels. Their results showed that increasing volume fraction of retained austenite could improve the formability. Although the factors mentioned above have been studied, why DP steels show the good mechanical properties are still unclear.

As described in **Chapter 3**, one reason is because for understanding the good mechanical properties of ferrite and martensite DP steels, it is necessary to study the deformation behavior of martensite and ferrite phase during deformation of DP steels.

However, in DP steel, martensite phase has a body-centered tetragonal (BCT) structure and ferrite has a BCC structure, martensite and ferrite have a similar phase structure, therefore, it is hard to distinguish them by EBSD, XRD etc. methods. For understanding the deformation behavior of two phases in DP alloys, it is easier to study the deformation behavior of two phases using DP alloy having different phase structures (FCC, BCC and etc.). As mentioned in **Chapter 1**, α - β brass having two different phase structures has an advantage to study the deformation behavior of two phases during specimen deformation. In addition, for α - β brass, the factors studied in DP steels are also available. By studying α - β brass alloy, it is also beneficial to understand the deformation behavior in DP steels. Based on the reasons described above, in this study, we use Cu-40 wt pct. Zn alloy to make specimens having different α - β dual phase

microstructures to study their deformation behaviors.

5.2. Experimental procedure

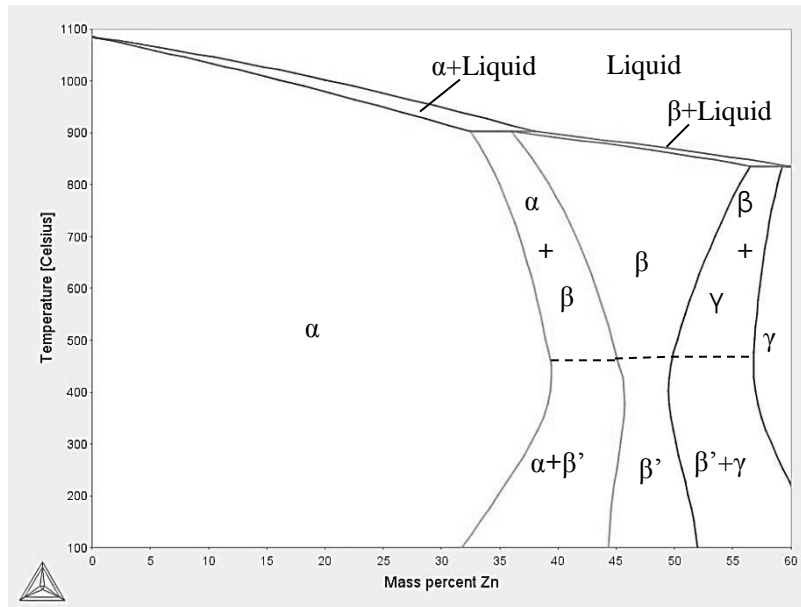


Figure 5.1 Cu-Zn phase diagram calculated by thermo-calc. α phase has a FCC structure, β phase has a Disordered-BCC structure and β' phase has an Ordered-BCC structure.

A binary alloy with a nominal composition of Cu-40wt pct. Zn was used. **Figure 5.1** shows Cu-Zn phase diagram calculated by thermos-cal. In the Cu-Zn phase diagram, α phase has a FCC structure, β phase has a Disordered-BCC structure and β' phase has an Ordered-BCC structure. A sheet 2 mm thick of Cu-Zn alloy was used in this study. Specimen A was heated at 850°C (β single phase region) for 1.8 ks and followed by air

cooling to homogenize the microstructure of alloy. Thereafter, for obtaining different microstructures of specimen B and specimen B, specimen B was solution treated at 700°C (α and β two phases region) for 1.8 ks followed by water quenching and specimen C was solution treated at 800°C (β single phase region) for 1.8 ks followed by water quenching . All the heat treatments were carried out using a salt bath furnace.

The microstructures of the specimens were observed by Optical Microscope (OM), Scanning Electron Microscopy (SEM) and Electron back-scattered diffraction (EBSD). X-ray diffraction (XRD) was used to examine phase structure in specimens. For SEM and EBSD observations, specimens were mechanically polished by emery papers and then electrochemically in an acid solution (100ml H₃PO₄+900ml H₂O). For OM observation, the polished surfaces were etched in an acid solution (10ml HCl+40ml C₂H₅OH+2g FeCl₃). Tensile tests at an initial strain rate of $8.3 \times 10^{-4} \text{ s}^{-1}$ were conducted at room temperature to test mechanical properties of the specimens. For doing tensile test, tensile test specimens with a gauge length of 10 mm, width of 5 mm, and thickness of 2 mm were prepared from the heat-treated specimens by spark-cutting. Nanoindentation test machine (Hysitron: TI 950 TriboIndenter) with a Berkovich indenter was used to measure the nanohardness of phases in specimens. The loading

rate of nanoindentation test was $50 \mu\text{N s}^{-1}$, and the maximum load was $500 \mu\text{N}$. In-situ neutron diffraction experiment was carried out to observe diffraction intensity and peak position change during continuous loading. The size of tensile test specimen for in-situ neutron diffraction experiments was having a gauge length of 12 mm, width of 3 mm and thickness of 2 mm. In-situ diffraction experiment was carried out at room temperature during tensile deformation by “TAKUMI” at J-PARC [17]. And axial direction of neutron diffraction results were shown and discussed in **Chapter 5**.

5.3. Results and discussion

5.3.1 Microstructure and phase identification of specimens before deformation

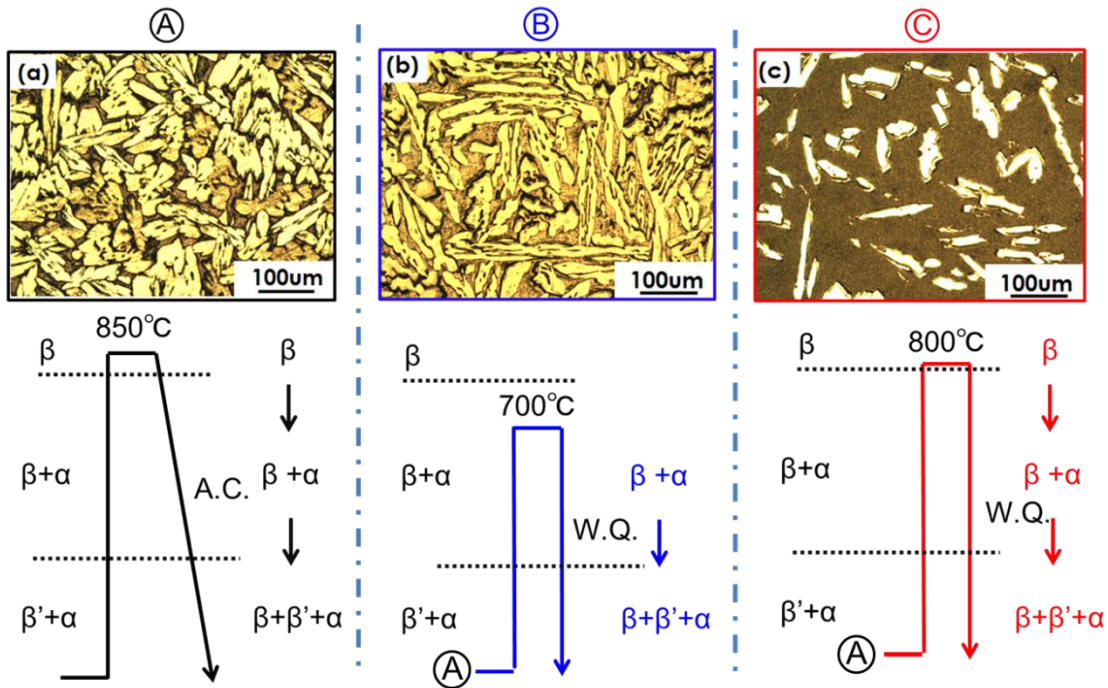


Figure 5.2 OM images of the Cu-40 wt pct. Zn specimens, taken by annealing at (a) 850°C for 1.8 ks cooled in air, and then heating to (b) 700°C for 1.8ks quenched in water, or heating to (c) 800°C for 30 min quenched in water. Specimens were etched in an acid solution (10ml HCl+40ml C₂H₅OH+2g FeCl₃) for OM observation. The heat treatment processes of the specimens were shown below optical micrographs.

Figure 5.2 shows OM images of specimen A (**Fig. 5.2a**), specimen B (**Fig. 5.2b**) and specimen C (**Fig. 5.2c**) after etching. **Fig. 5.2a** shows OM image of specimen A. It shows plate-like structure in the matrix. **Fig. 5.2b** and **Fig. 5.2c** show OM images of

specimen B and specimen C. They also show plate-like structure in the matrix. Based on the phase diagram of Cu-Zn alloy in **Fig. 5.1** and the experimental process in **Fig. 5.2**, specimens A, B and C should have microstructures composed of α phase (FCC), β phase (Disordered-BCC) and β' phase (Ordered-BCC).

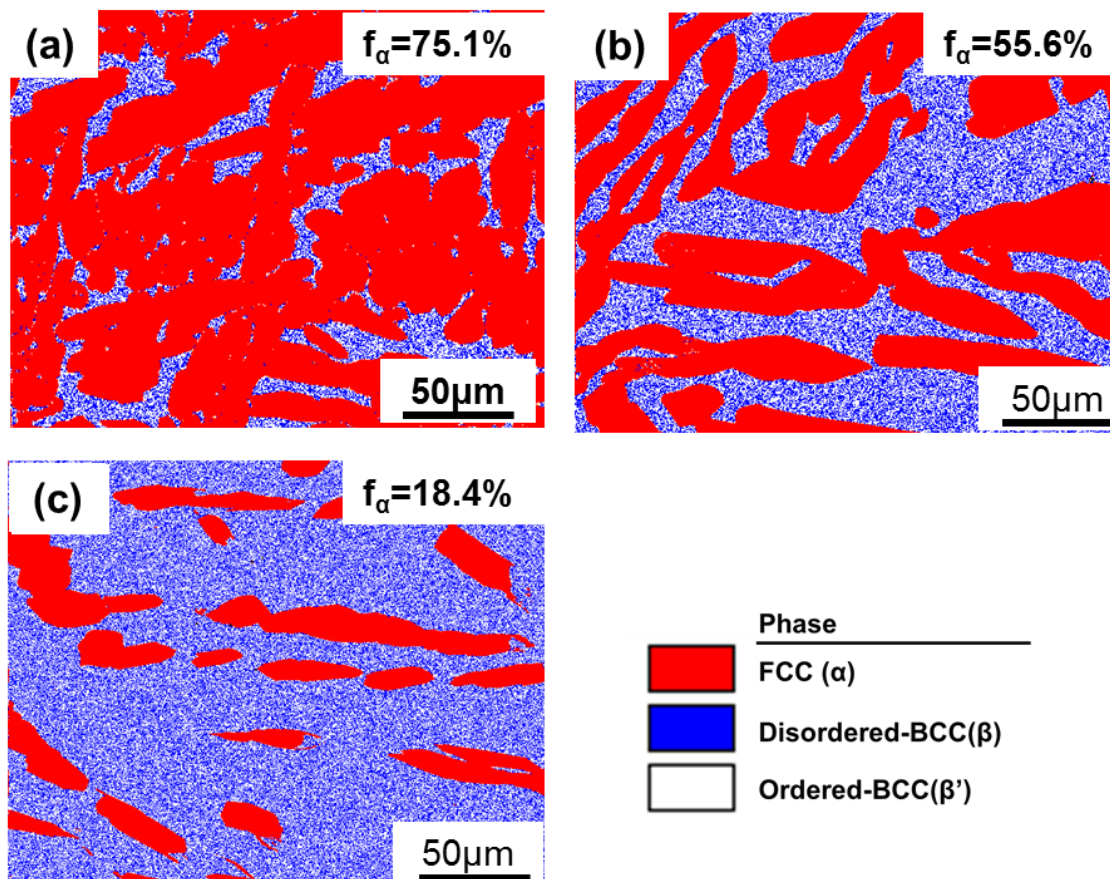


Figure 5.3 Electron back-scattered diffraction (EBSD) phase maps of the Cu-40wt. %Zn specimens, taken by annealing at (a) 850°C for 1.8 ks cooled in air, and then heating to (b) 700°C for 1.8 ks quenched in water, or heating to (c) 800°C for 1.8 ks quenched in water. Red color in EBSD phase maps represents FCC phase structure indicate α phase; Blue color in EBSD phase maps represents Disordered-BCC structure

indicate β phase; White color in EBSD phase maps represents Ordered-BCC structure indicate β' phase. The volume fraction of α phase in specimens is shown in EBSD phase maps.

Figure 5.3 shows the EBSD phase maps of specimen A (**Fig. 5.3a**), specimen B (**Fig. 5.3b**) and specimen C (**Fig. 5.3c**). In EBSD phase maps, red color represents FCC phase structure indicate α phase in Cu-Zn phase diagram. Blue color and white color are representing Disordered-BCC phase structure and Ordered-BCC phase structures indicated β phase and β' phase in Cu-Zn phase diagram, respectively. **Fig. 5.3a**, **Fig. 5.3b** and **Fig. 5.3c** show that the plate-like structure possesses red color and matrix possesses blue and white colors, which indicate the plate-like structure is α (FCC) phase and the matrix are β (BCC) and β' (ordered-BCC) phases. In specimen B and specimen C the volume fraction of α phase were 55.6% and 18.4%, respectively, by line point counting from low magnification OM images. EBSD results show β and β' phases were in the matrix, however, the structure difference between β and β' phases are too small, so there is a possibility that the EBSD could misidentify the β and β' phases in the matrix. For this reason, we measured the XRD results of specimen A and specimen B before tensile deformation shown in **Figure 5.4**.

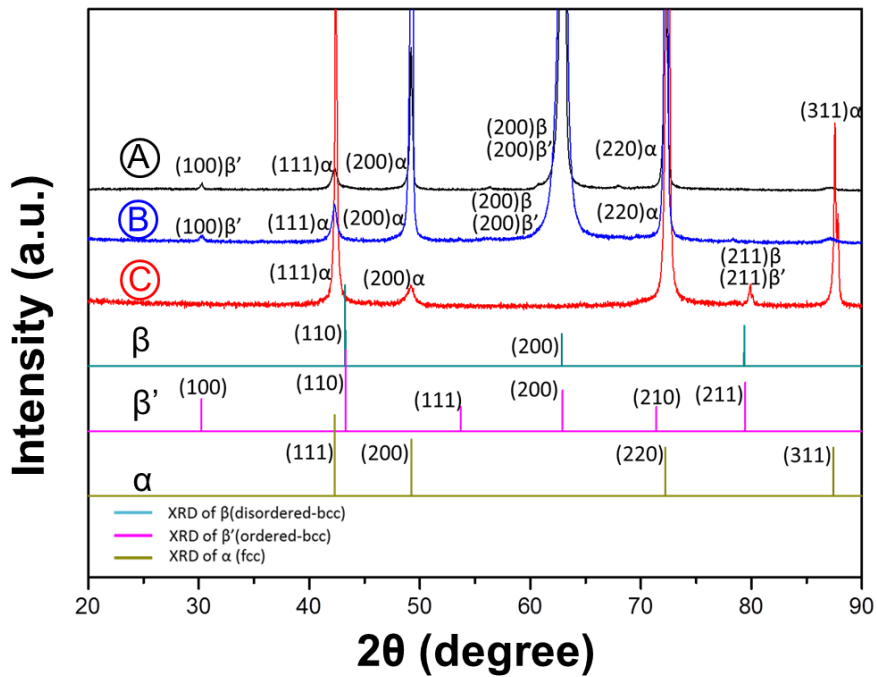


Figure 5.4 XRD patterns of the specimens A, B and C before tensile deformation. The peak positions of α phase, β phase and β' phase were shown under XRD result of specimen C.

Figure 5.4 shows the XRD patterns of specimens A, B and C before tensile deformation. The peak positions of α phase, β phase and β' phase were shown below the XRD result of specimen C. For XRD result of specimen A, diffraction peaks of $(100) \beta'$ phase and $(200) \alpha$ phase were appeared, which indicated β' phase and α phase were existed in the specimen A. Compared with $(100) \beta'$ phase, diffraction peak intensity of $(200) \beta'$ phase was too huge. The huge intensity of diffraction peak was because it overlapped

the diffraction peaks of (200) β phase and (200) β' phase. Therefore, α phase, β phase and β' phase should be in the specimen A. The XRD diffraction peaks shown in specimen B was similar as it shown in specimen A. For specimen C, the diffraction peak of (211) β phase was overlapped with the diffraction peak of (211) β' phase. Only (211) β/β' diffraction peak was observed in the specimen C was due to the grain sizes of β/β' phase was too large (average grain sizes of matrix phase was 1.5 μm). In the specimen C, only (211) β/β' phase grain was measured in the XRD measurement. Based on the results of OM images (**Fig. 5.2**) and EBSD (**Fig. 5.3**) and XRD (**Fig. 5.4**), α phase, β phase and β' phase should be contained in the specimens A, B and C. β phase and β' phase were in the matrix of specimens A, B and C.

The present results show that α phase, β phase and β' phase were in specimens A, B and C (**Fig. 5.3** and **Fig. 5.4**). For making dual phase specimens, the specimen B and specimen C were water quenched from two phase region ($\alpha+\beta$) and single phase region (β), respectively. β phase is quite easy to transform into β' phase even by water quenching. Present results shows that β phase is difficulty to completely transformed into β' phase by water quenching. β phase and β' phases show the similar phase structure and the two phases are mixed together in matrix.

5.3.2 Mechanical properties

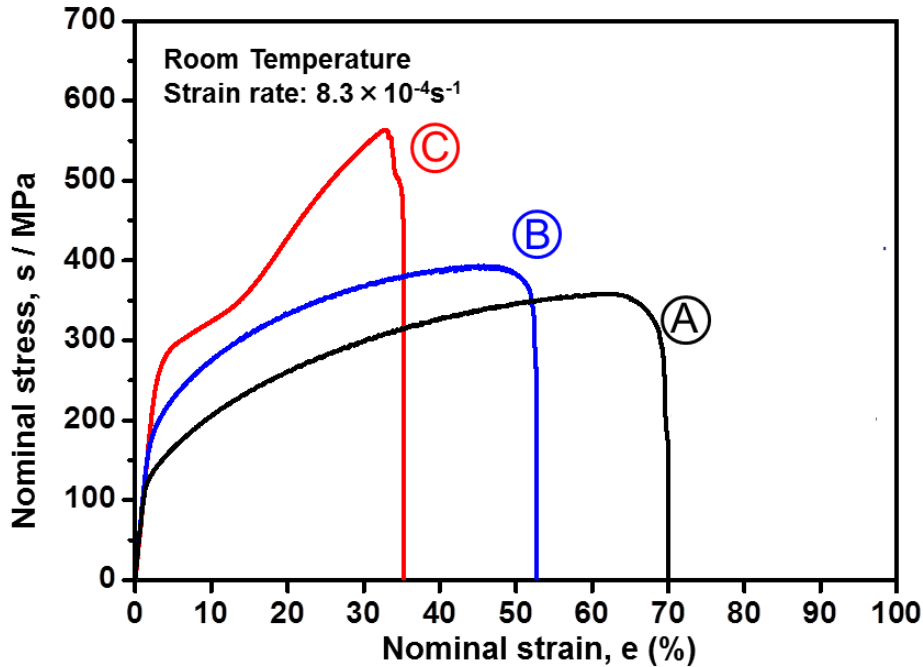


Figure 5.5 Nominal stress-nominal strain curves for specimens A, B and C tensile tested at room temperature. The strain rate of tensile tests is $8.3 \times 10^{-4} \text{s}^{-1}$. Strain was measured by crosshead travel.

Figure 5.5 shows the stress-strain curve of specimens A, B and C tensile tested at room temperature at a constant strain rate $8.3 \times 10^{-4} \text{s}^{-1}$. **Fig. 5.5** shows that specimen C has a higher yield strength and tensile strength than in the specimens A and B. On the other hand, specimen C shows a smaller uniform elongation than it in specimen A and specimen B. For understanding the reason, nanoindentation of specimen C was measured before tensile deformation. The nanoindentation results show that the

nanohardness of α phase and matrix are 1.98 GPa and 2.63 GPa, respectively. The Nanoindentation test results indicate that α phase is softer than the matrix. The volume fraction of soft α phase in specimen C is lower than it in specimens A and B. This might be the reason why specimen C has higher yield strength than specimens A and B shown in **Fig. 5.5**. Akbarpour et al. [10] have reported that, in dual phase steels, yield strength, ultimate tensile strength decrease linearly with increasing soft ferrite volume fraction while ductility increases. The volume fraction effects studied in DP steel is also available in α - β brass.

5.3.3 Microstructure and mechanical properties change in Specimen A ($f_{\alpha}=75.1\%$)

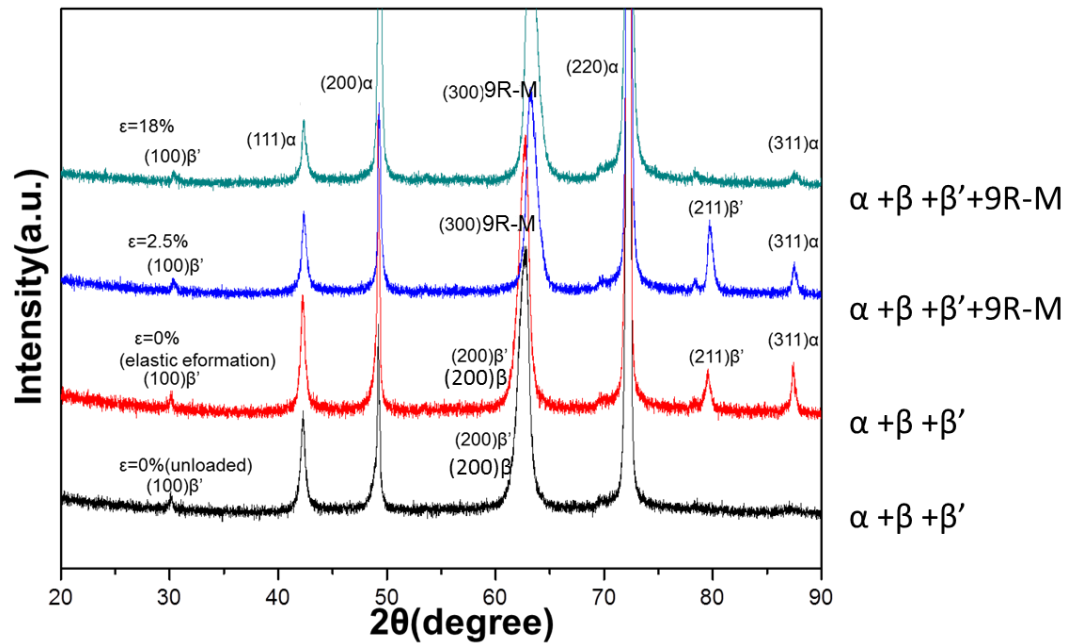


Figure 5.6 XRD results of specimen A deformed at different tensile strain. XRD results were measured after unloading the specimens from tensile test machine.

Figure 5.6 shows the XRD results of specimen A deformed at different tensile strain.

Before tensile deformation ($\epsilon=0\%$, unloaded), XRD result (black curve in **Fig. 5.6**)

show diffraction peaks of α , β and β' phases. The specimen A deformed in the elastic

tensile deformation region ($\epsilon=0\%$, elastic deformation) shows similar XRD result (red

curve) as it shows before tensile deformation. When the specimen A starts plastic

deformation ($\epsilon=2.5\%$), diffraction peak position of (200) matrix phases (β and β' phases)

was changed. Previous studies showed that matrix phases will transform to 9R-M phase which possess a monoclinic structure [18-20]. The lattice parameter of 9R-M is $a=0.4412$ nm, $b=0.2678$ nm, $c=1.919$ nm, $\alpha=90^\circ$, $\beta=88.43^\circ$ and $\gamma=90^\circ$. Base on the parameter of 9R-M phase, it can be calculated that (300) 9R-M shows a diffraction peak at an angle 2θ of 63.54° . The diffraction peak of (200) matrix phase was at an angle 2θ of 62.75° . However, the diffraction peak at the angle 2θ was changed to 63.10° when the specimen tensile deformed at 2.5%. So the diffraction peak position change of (200) matrix phase is due to the formation of 9R-M phase. The specimen shows α , β , β' and 9R-M phases at the beginning of plastic deformation ($e=2.5\%$). When the specimen deformed more ($e=18\%$), a new diffraction peak at an angle 2θ of 71.43° was appeared.

Figure 5.7 shows the EBSD phase maps of specimen A tensile deformed at different strain. In the EBSD phase maps, Red color in EBSD phase maps represents FCC phase structure indicate α phase or represents face-centered tetragonal (FCT) phase structure indicate 3R-M phase; Blue color in EBSD phase maps represents Disordered-BCC structure indicate β phase; White color in EBSD phase maps represents Ordered-BCC structure indicate β' phase. 9R-M phase has monoclinic

structure is indexed into yellow in EBSD phase maps. Both FCC phase structure and

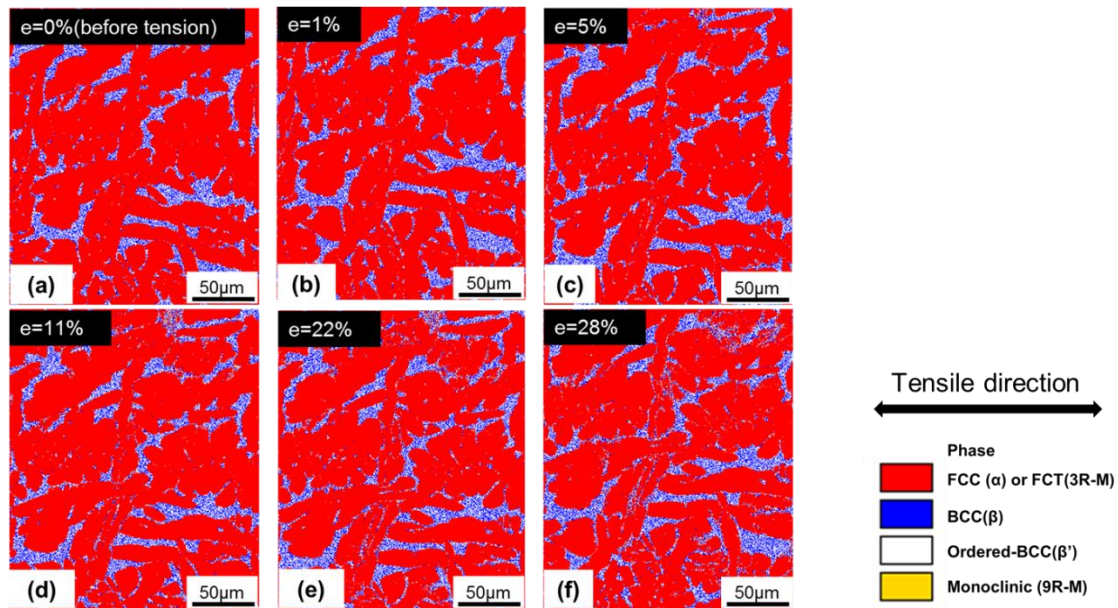


Figure 5.7 EBSD phase maps of specimen A tensile deformed at (a) $e=0\%$, before tensile deformation, (b) $e=1\%$, (c) $e=5\%$, (d) $e=11\%$, (e) $e=22\%$ and (f) $e=28\%$. EBSD results were measured after unloading the specimens from tensile test machine. Tensile direction is in the horizontal direction. Red color in EBSD phase maps represents FCC phase structure indicate α phase or represents face-centered tetragonal (FCT) phase structure indicate 3R-M phase; Blue color in EBSD phase maps represents Disordered-BCC structure indicate β phase; White color in EBSD phase maps represents Ordered-BCC structure indicate β' phase. 9R-M phase has monoclinic structure is indexed into yellow in EBSD phase maps.

FCT phase structure possessed red color is because the structure of FCC phase and FCT phase are quite similar, so it is hard to distinguish them by EBSD phase map. There is no yellow color in EBSD phase map even specimen A tensile deformed 28% shown in

Fig. 5.7f. Together with XRD result shown in **Fig. 5.6**, it is indicated that 9R-M phase

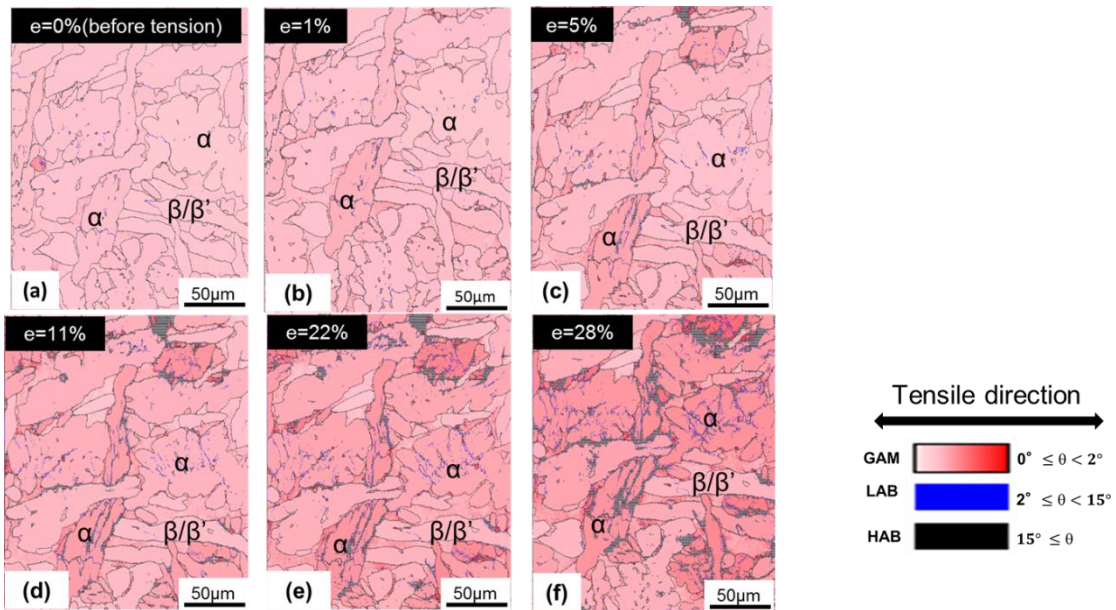


Figure 5.8 The grain average misorientation maps (GAM) of specimen A tensile deformed at (a) $e=0\%$, before tensile deformation, (b) $e=1\%$, (c) $e=5\%$, (d) $e=11\%$, (e) $e=22\%$ and (f) $e=28\%$. LAB is low-angle boundary with misorientation of $2-15^\circ$ is drawn in blue lines. HAB is high-angle boundary with misorientation above 15° is drawn in black lines. The gray color in (d-f) are heavily deformed area, and no reliable EBSD result can be obtained due to the low confidence index (CI) value in these areas. α phase and matrix phases (β/β') are labeled on GAMs, according to the result of EBSD phase maps shown in **Fig. 5.7**. Tensile direction is in the horizontal direction.

is invisible to EBSD phase map.

Figure 5.8 shows the grain average misorientation map (GAM) of specimen A. In GAM map, the orientation was calculated between each neighboring pair of points within the grain. The GAM values indicate the dislocation density and substructures.

The GAM values were colored in **Fig. 5.8**. White color represents low GAM value and red color represents high GAM value. From **Fig 5.8a** to **Fig 5.8f**, it can be found more dark red color was in α phase than the red color can be found in matrix (β/β') with increasing tensile deformation strain. The result indicated that there were more dislocations and fine substructures in α phase than them in matrix phases. The results suggested that α phase in specimen A was deformed more than matrix phases (β/β') during tensile deformation.

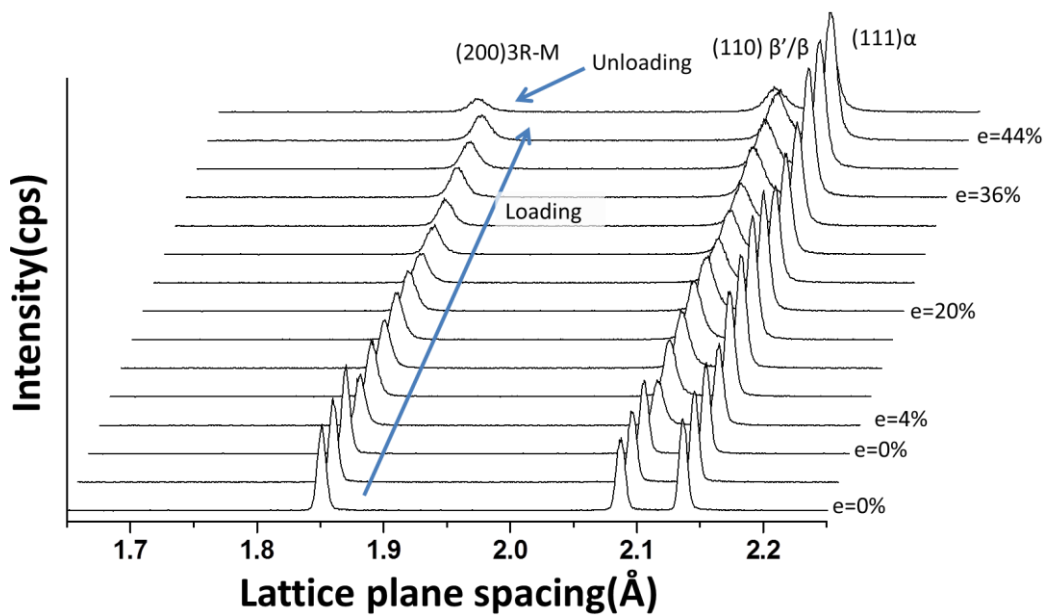


Figure 5.9 In-situ neutron diffraction results of specimen A during tensile deformation. Neutron diffraction profiles are in the axial direction. Tensile strain is shown from 0% to 44%.

Figure 5.9 shows the In-situ neutron diffraction results of specimen B during tensile deformation. Diffraction peaks of 3R-M phase, matrix phases (β/β') and α phase are existed in the specimen A before deformation ($\epsilon=0\%$). Base on the diffraction peak of (200) plane of 3R-M phase in specimen A, lattice parameters of 3R-M phase can be calculated as $a=b=0.36994$ nm, $c=0.36151$ nm and $\alpha=\beta=\gamma=90^\circ$.

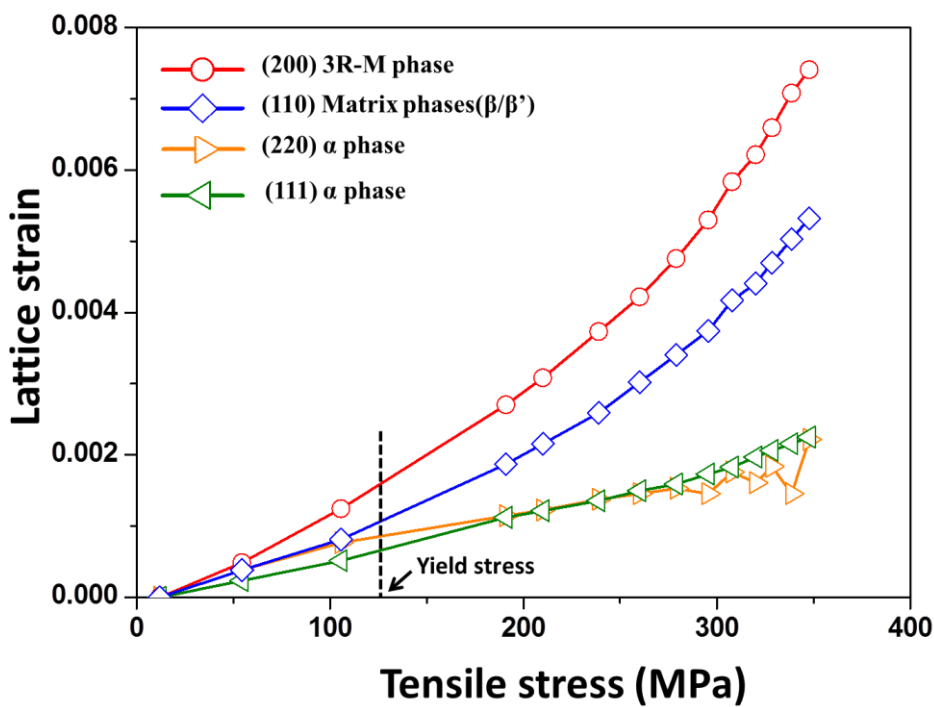


Figure 5.10 Changes in lattice strains of (200) 3R-M phase, (110) matrix phases, (220) α phase and (111) α phase as a function of the tensile stress.

Figure 5.10 shows Changes in lattice strains of (200) 3R-M phase, (110) matrix phases,

(220) α phase and (111) α phase as a function of the tensile stress in specimen A. It is found that the lattice strain in 3R-M phase and matrix phases quickly increased after the specimen yielding. The result indicates that 3R-M phase and matrix phases bear higher stress after the specimen yielding. In α phase, (220) and (111) lattice strain in α phase slightly increased after the specimen yielding.

In order to see the stress partitioning on each whole phase, phase strain of each phase was estimated by averaging different (hkl) lattice strains. In specimen A, the grain size of β/β' phase is quite large ($d=1.5\text{mm}$), so only several grains of matrix phases can be observed during experiment. In specimen A, lattice strain of (110) matrix phases was treated as matrix phases strain. And the lattice strain of (200) grains of 3R-M phase was treated as 3R-M phase strain. The average lattice strain of (220) grains and (111) grains in α phase was treated as α phase strain.

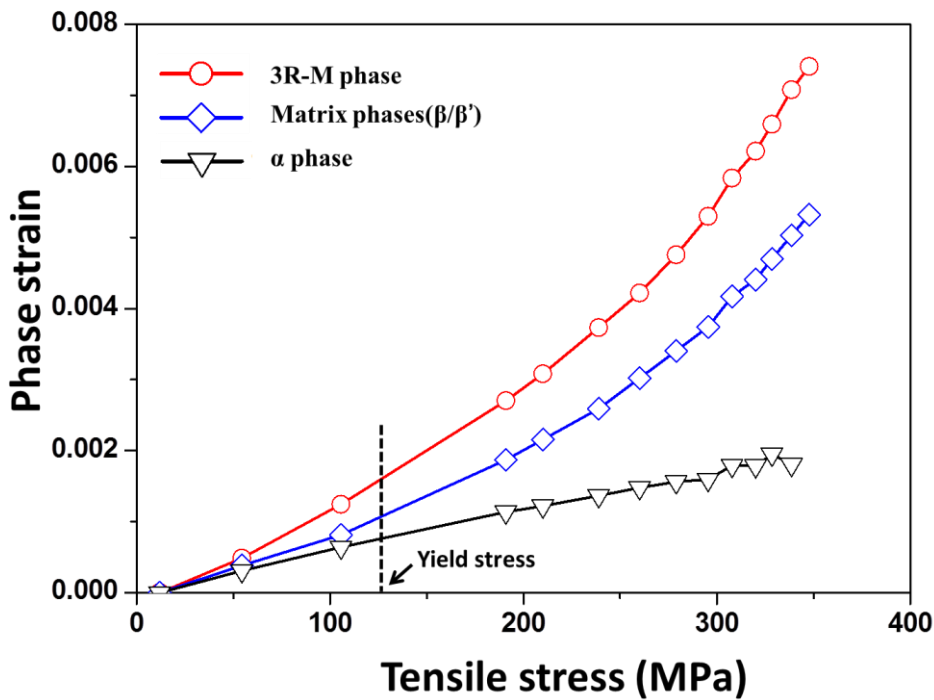


Figure 5.11 Change in phase strains in specimen A as a function of the tensile stress.

Figure 5.11 shows change of the phase strain of 3R-M phase, matrix phases and α phase as a function of tensile stress and tensile strain. **Fig. 5.11** shows before the specimen yielding, 3R-M phase, Matrix phases and α phase strains are linearly increased with increasing tensile stress. After the specimen yielding, phase strain in α phase slightly increase with increasing tensile stress. After the specimen yielding, the phase strains in 3R-M phase and the matrix phases increase faster with increasing tensile stress. That means hard 3R-M phase and the matrix phase bear more stress after yielding. The results shown in **Fig. 5.11** indicate that 3R-M should be hardest among the phases. And matrix phase is harder than α phase.

5.3.4 Microstructure and mechanical properties change in Specimen B ($f_{\alpha}=55.6\%$)

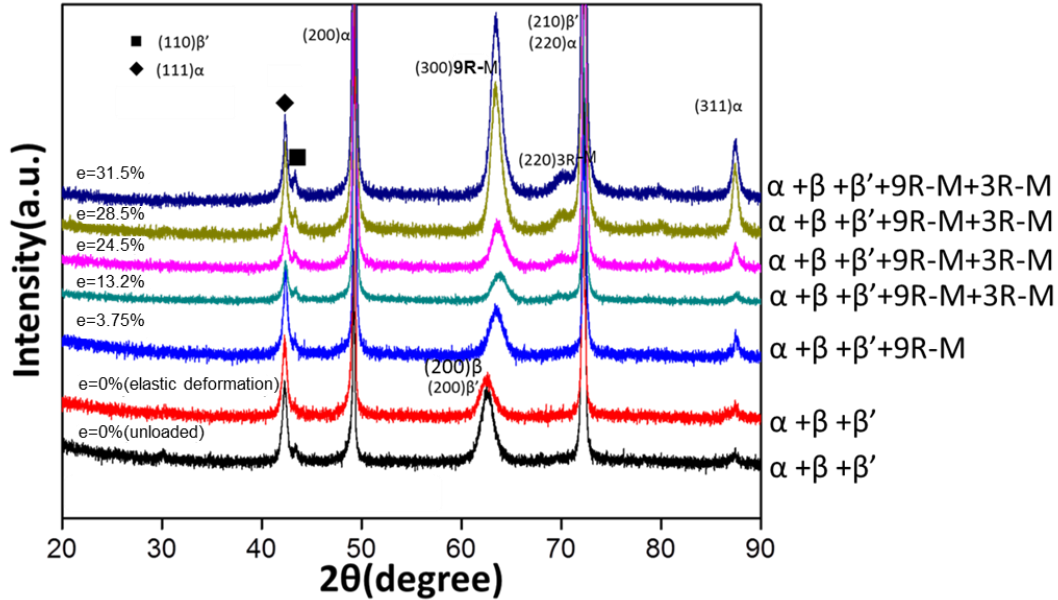


Figure 5.12 XRD results of specimen B deformed at different tensile strain. XRD results were measured after unloading the specimens from tensile test machine.

Figure 5.12 shows the XRD results of specimen B deformed at different tensile strain.

Before tensile deformation ($e=0\%$, unloaded), XRD result (black curve in Fig. 5.12)

show diffraction peaks of α , β and β' phases. Diffraction peak of specimen B

deformed in elastic region shows similar result as specimen B before deformation.

When plastic deformation start ($e=3.75\%$), diffraction peak position of (200) matrix

phase (β and β' phases) was changed. As discussed in **Fig. 5.6**, the diffraction peak

position change of (200) matrix phase is due to the formation of 9R-M phase. The

specimen shows α , β , β' and 9R-M phases at the beginning of plastic deformation ($e=3.75\%$). When the specimen deformed more ($e=13.2\%$), a new diffraction peak at an angle 2θ of 71.43° was appeared. Previous studies showed that during plastic deformation, 9R-M phase could transform to 3R-M phase which possess a FCT structure [18, 20, 21]. The new diffraction peak at an angle 2θ of 71.43° indicates (220) 3R-M phase appear. When further deformed the specimen ($e=24.5\%$, $e=28.5\%$, $e=31.5\%$), the diffraction peak intensity of (220) 3R-M phase increase, which means the content of 3R-M phase increase.

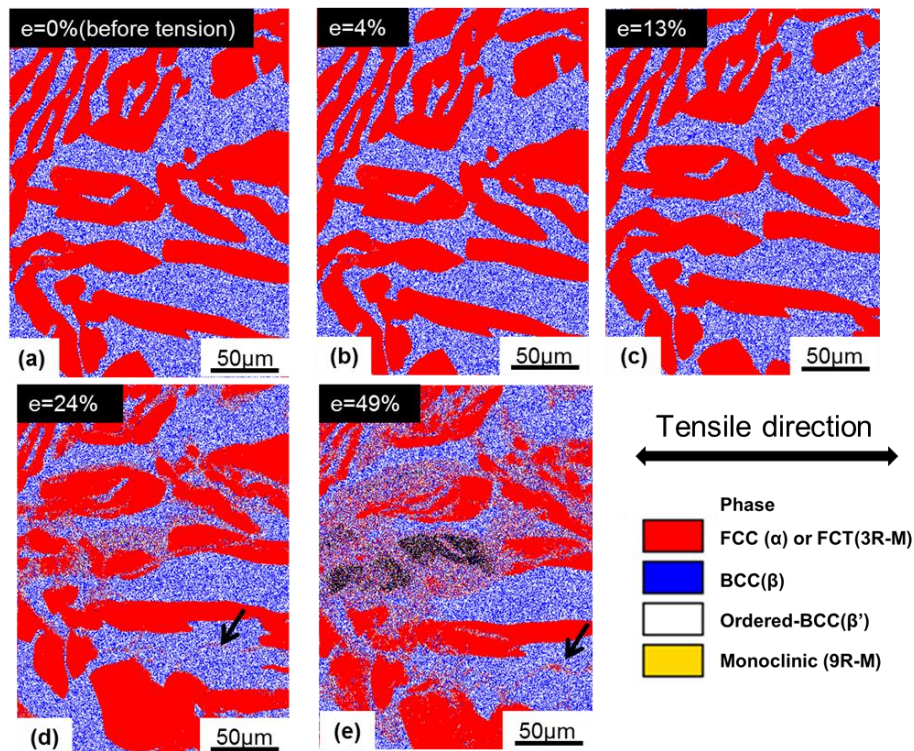


Figure 5.13 EBSD phase maps of specimen A tensile deformed at (a) $e=0\%$, before tensile deformation, (b) $e=4\%$, (c) $e=13\%$, (d) $e=24\%$ and (e) $e=49\%$. EBSD results

were measured after unloading the specimens from tensile test machine. Tensile direction is in the horizontal direction. Red color in EBSD phase maps represents FCC phase structure indicate α phase or represents face-centered tetragonal (FCT) phase structure indicate 3R-M phase; Blue color in EBSD phase maps represents Disordered-BCC structure indicate β phase; White color in EBSD phase maps represents Ordered-BCC structure indicate β' phase. 9R-M phase has monoclinic structure is indexed into yellow in EBSD phase maps.

Figure 5.13 shows the EBSD phase maps of specimen B tensile deformed at different strain. In the EBSD phase maps, the red color represents FCC phase structure or FCT phase structure. The blue color is BCC phase structure and white color is ordered bcc phase structure. The 9R-M phase was indexed into yellow color. As discussed in **Fig. 5.7**, FCT phase and FCC phase are hard to be distinguished under EBSD observation. Together with the XRD result in **Fig. 5.12**, 9R-M phase is also invisible to EBSD phase map, which is the similar to the specimen A observation shown in **Fig. 7**. At higher tensile strain ($\epsilon = 24\%$), it can be found a few amount of new red color in the matrix. Together with XRD results shown in **Fig. 5.12**, this new red color should be 3R-M phase having a FCT structure.

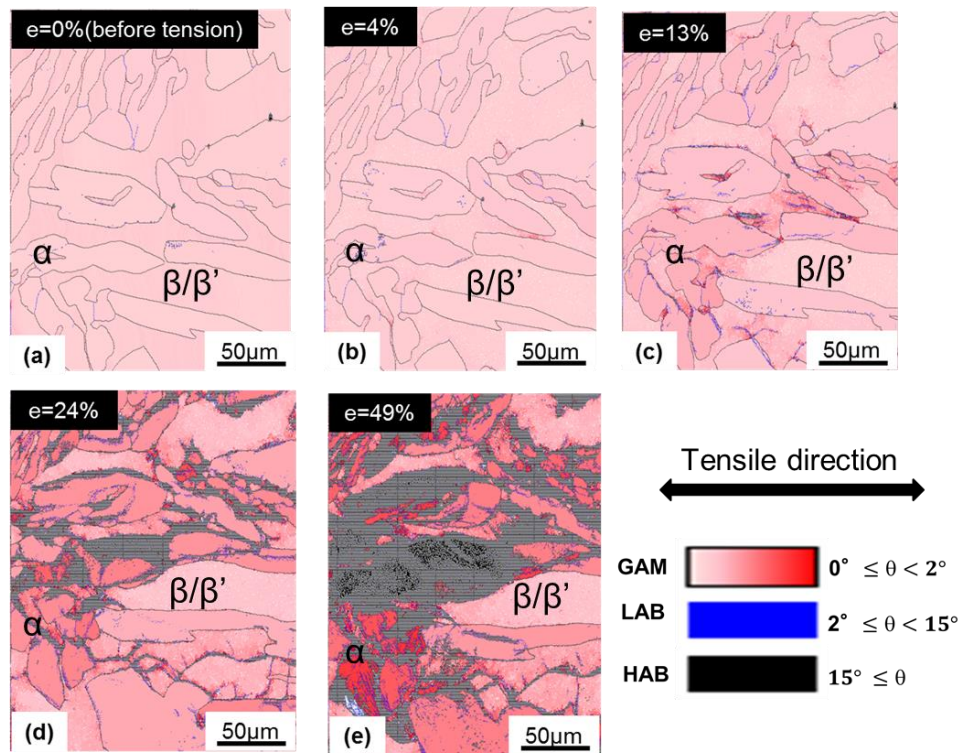


Figure 5.14 The grain average misorientation maps (GAM) of specimen B tensile deformed at (a) $e=0\%$, before tensile deformation, (b) $e=4\%$, (c) $e=13\%$, (d) $e=24\%$ and (e) $e=49\%$. LAB is low-angle boundary with misorientation of $2-15^\circ$ is drawn in blue lines. HAB is high-angle boundary with misorientation above 15° is drawn in black lines. The gray color in (d-e) are heavily deformed area, and no reliable EBSD result can be obtained due to the low confidence index (CI) value in these areas. α phase and matrix phases (β/β') are labeled on GAMs, according to the result of EBSD phase maps shown in **Fig. 5.13**. Tensile direction is in the horizontal direction.

Figure 5.14 shows the grain average misorientation map (GAM) of specimen B. The GAM values were colored in **Fig. 5.14**. White color represents low GAM value and red color represents high GAM value. α phase and matrix phases (β/β') are labeled on

GAMs, according to the result of EBSD phase maps shown in **Fig. 5.13**. From **Fig 5.14a** to **Fig 5.14e**, with increasing tensile strain, it can be found more dark red color was in α phase than the red color can be found in matrix (β/β'). It indicated that there were more dislocations and fine substructures in α phase than in matrix. That means α phase was deformed more than matrix phase during tensile deformation.

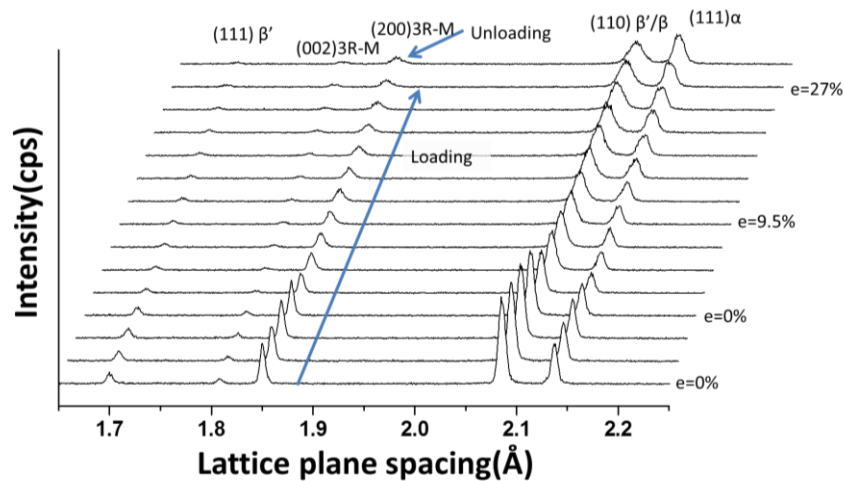


Figure 5.15 In-situ neutron diffraction results of specimen B during tensile deformation.

Neutron diffraction profiles are in the axial direction. Tensile strain is shown from 0% up to 27%.

Figure 5.15 shows the In-situ neutron diffraction results of specimen B during tensile deformation. Diffraction peaks of (002) plane and (200) plane of 3R-M phase, (110)

plane of matrix phases (β/β') and (111) α phase are existed in the specimen B before tensile deformation ($\epsilon=0\%$). During tensile deformation, the changes in lattice strains are shown in **Fig. 5.16**.

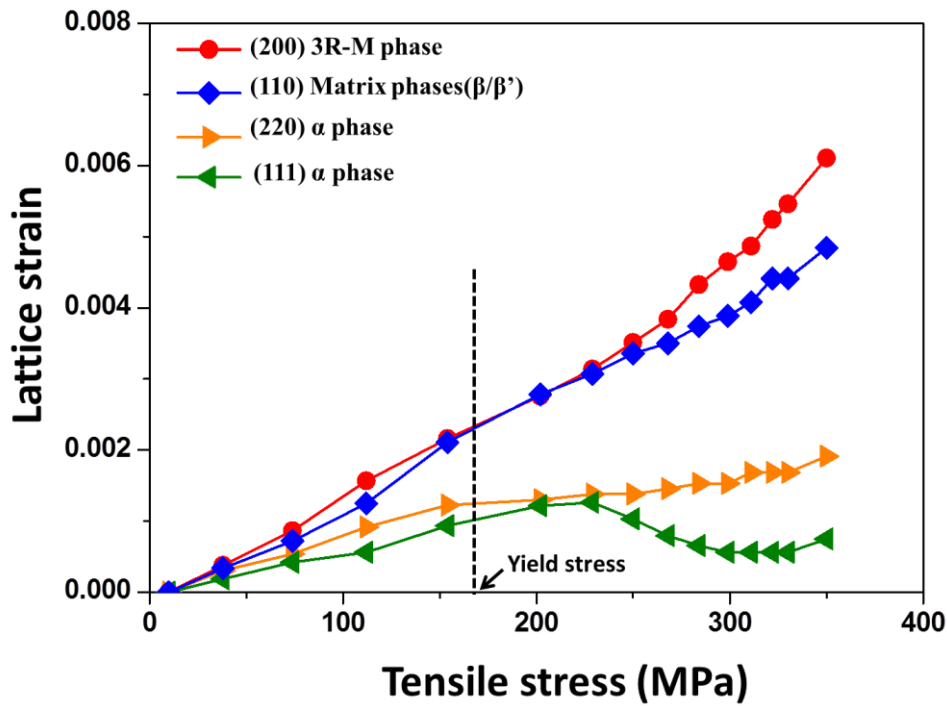


Figure 5.16 Changes in lattice strains of (200) 3R-M phase, (110) matrix phases and (220) α phase and (111) α phase as a function of the tensile stress. The yield stress is marked using dash line.

Fig. 5.16 shows Changes in lattice strains of (200) 3R-M phase, (110) matrix phases, (220) α phase and (111) α phase as a function of the tensile stress in specimen B during tensile test in the axial direction. It is found that the lattice strain in 3R-M phase and

matrix phases quickly increased after the specimen yielding, which is similar to the specimen A shown in Fig. 5.10. The result indicates that 3R-M phase and matrix phases bear higher stress after the specimen yielding. In α phase, (220) lattice strain in α phase slightly increased after the specimen yielding. But (111) lattice strain in α phase decreased after the specimen yielding. That means (111) plane in α phase is weaker than (220) plane during deformation. The phase strains estimated by averaging (hkl) lattice strains are shown in **Fig. 5.17**.

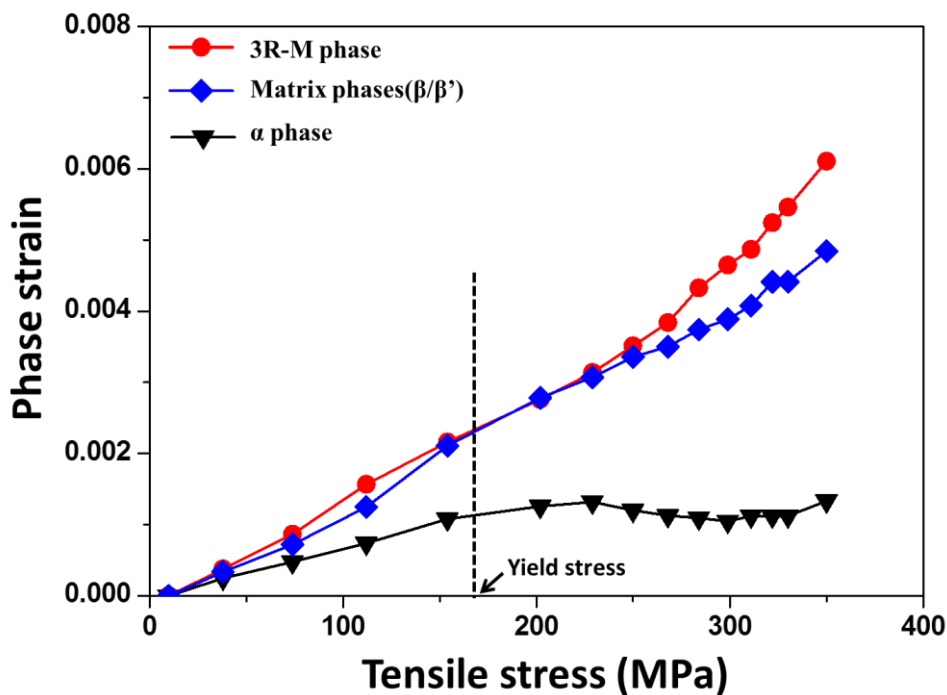


Figure 5.17 Change in phase strains in specimen B as a function of the tensile stress. Yield stress is marked in dash line.

Figure 5.17 shows change of the phase strain of 3R-M phase, matrix phases and α

phase as a function of tensile stress and tensile strain. **Fig. 5.17** shows before the specimen yielding, 3R-M phase and Matrix phases strains are increased with increasing tensile stress. After the specimen yielding, phase strain in α phase slightly decreased with increasing tensile stress. After the specimen yielding, the phase strains in 3R-M phase and the matrix phases rapidly increased with increasing tensile stress. The result indicates that hard 3R-M phase and the matrix phase bear more stress after yielding. After yielding, α phase starts plastic deformation firstly. The results shown in **Fig. 5.17** indicate that 3R-M should be hardest among the phases and matrix phase is harder than α phase.

5.3.5 Microstructure and mechanical properties change in Specimen C ($f_{\alpha}=18.4\%$)

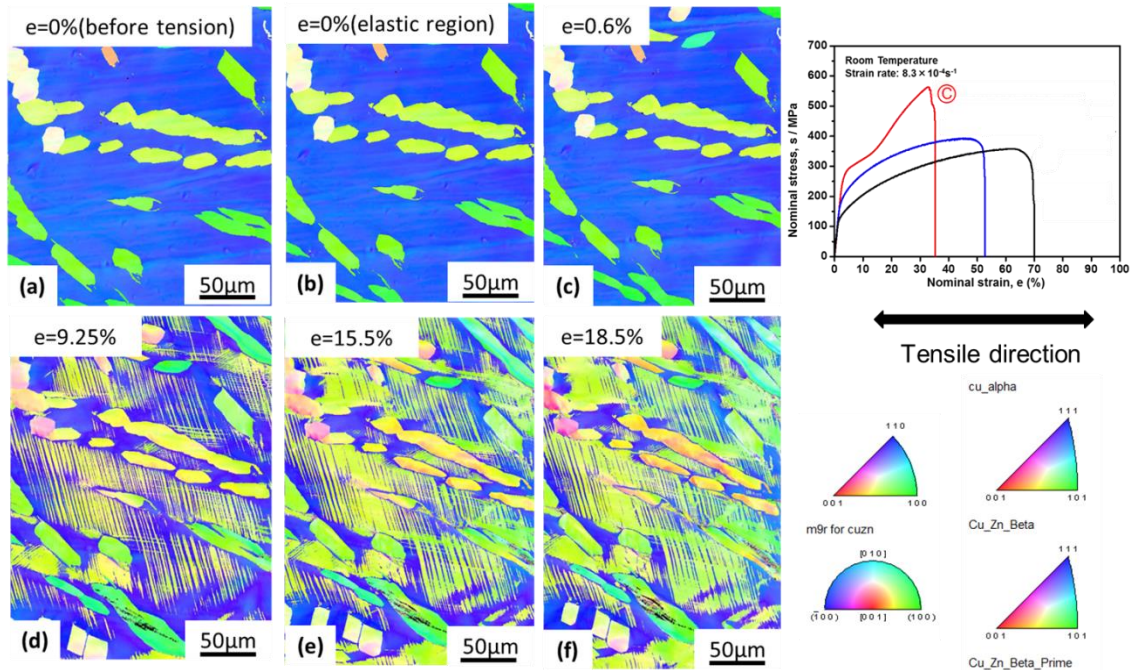


Figure 5.18 Inverse pole figure (IPF) maps of specimen C deformed at different tensile strain. Stress-strain curve is shown on the right side. Tensile direction is in the horizontal direction.

Fig. 5.18 shows inverse pole figure (IPF) maps of specimen C. As can be seen, there was no orientation change in elastic deformation region (**Fig. 5.18b**) and early plastic deformation region (**Fig. 5.18c**). When the specimen deformed at higher tensile strain ($e \geq 9.25\%$), it can be found new orientations appeared in matrix phase. With increasing tensile strain, more content of new orientations were appeared. The plate structure was α phase. The color change in α phase during deformation indicates

orientation changes, which were due to the plastic deformation.

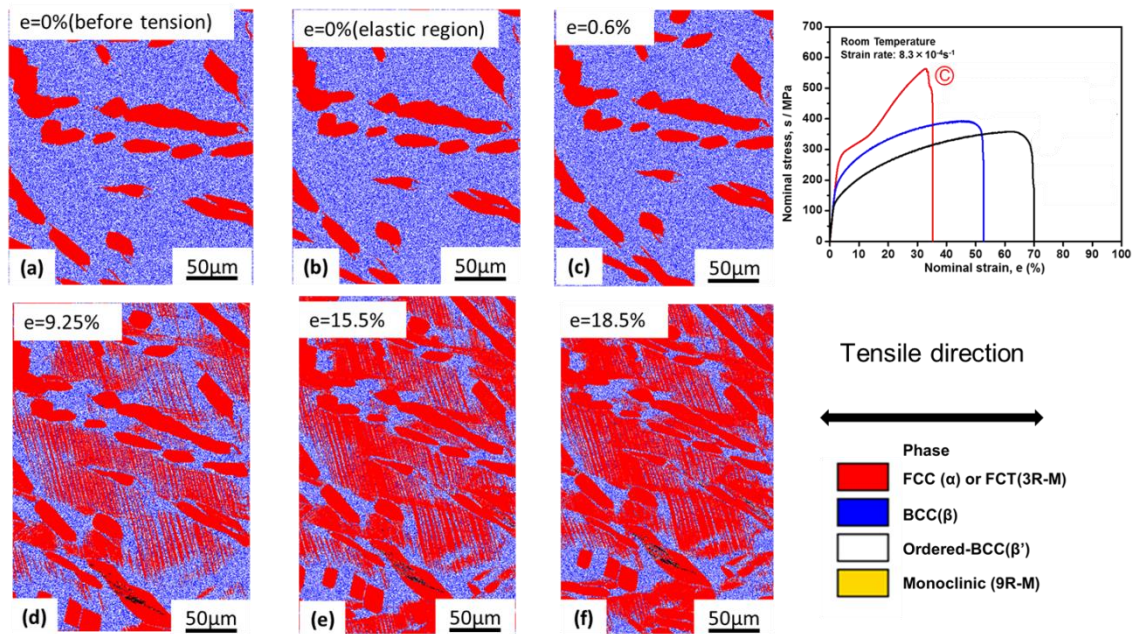


Figure 5.19 EBSD phase maps of specimen C deformed at different tensile strain. Stress-strain curve is shown on the right side. Tensile direction is in the horizontal direction.

Fig. 5.19 shows the EBSD phase maps of specimen C deformed at different tensile strain. In the EBSD phase maps, the red color represents FCC phase structure or FCT phase structure. The blue core represents BCC phase structure and white color represents Ordered-BCC phase structure. The 9R-M phase was indexed into yellow color. As discussed in **Fig. 5.7**, 9R-M phase is invisible to EBSD measurement. It can be seen, there was no new phase appearing in elastic deformation region (**Fig 5.19b**)

and early plastic deformation region (**Fig. 5.19c**). When the specimen deformed at higher tensile strain ($e \cong 9.25\%$), new phase possessed red color was appeared in matrix. With increasing tensile strain, more content of new phase were appearing. Together the results with **Fig. 5.18**, the new orientation in **Fig. 5.18** are the new phase which possessed FCC phase structure or FCT phase structure.

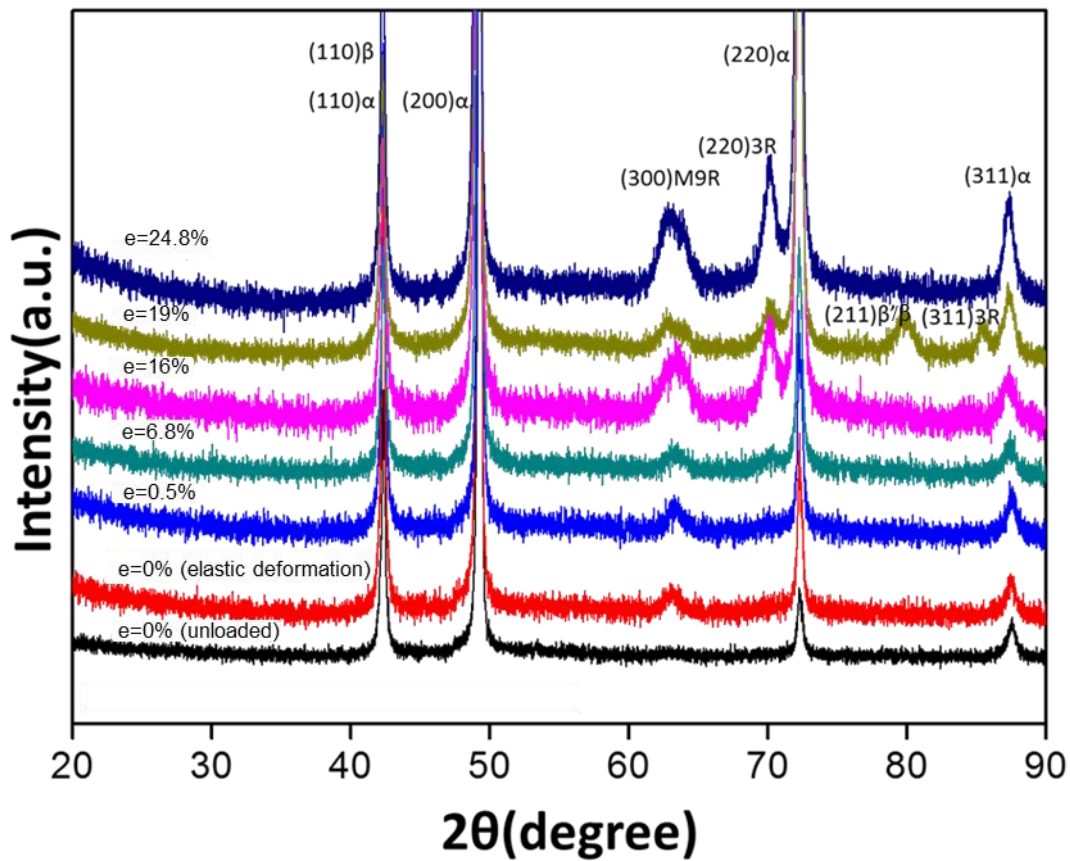


Figure 5.20 XRD results of specimen C deformed at different tensile strain. XRD results were measured after unloading the specimens from tensile test machine.

Fig. 5.20 shows the XRD results of specimen C deformed at different tensile strain. It can be seen that (220)3R-M phase start appearing at high tensile strain ($\epsilon=16\%$). Together with the results of Figure 5.20, the new phase appear in **Fig. 5.20** should be 3R-M phase. (211) β/β' phase appeared ($\epsilon=16\%$) might be caused by the deformation of the specimen. The (211) β/β' phase plane appear in the measurement area during tensile deformation.

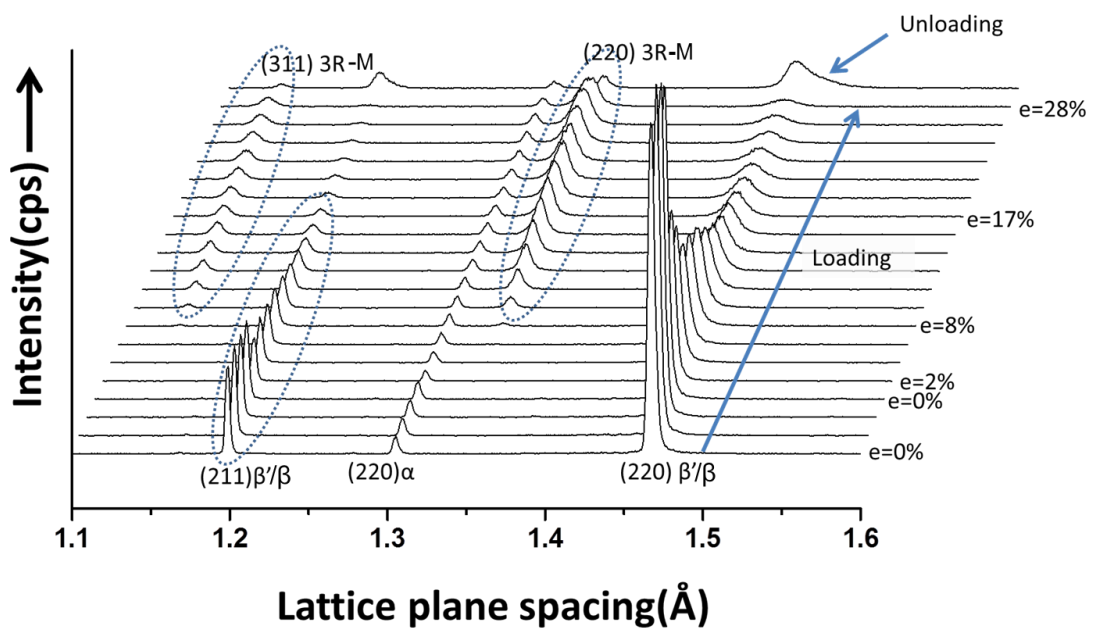


Figure 5.21 In-situ neutron diffraction results of specimen C during tensile deformation. Neutron diffraction profiles are in the axial direction. Tensile strain is shown from 0% to 28%.

Fig. 5.21 shows the In-situ neutron diffraction results of specimen C during deformation. As can be seen, intensity of (211) β / β' diffraction peak and (220) β / β' diffraction peak were decreased when plastic deformation was started ($e=2\%$). Decreasing the intensity of β / β' diffraction peak was because β / β' phase transformed into 9R-M phase. When the specimen was tensile deformed at 8%, (311) and (220) diffraction peak of 3R-M phase were appeared. With further deformation, the intensity of (311)3R-M and (220) 3R-M diffraction peak were increasing. Increasing the intensity diffraction peak of 3R-M phase means that the content of 3R-M phase was increased during deformation. After unloading, the diffraction peak intensity of (311)3R-M and (220)3R-M phase were decreased, while the diffraction peak intensity of (211) β/β' and (220) β / β' were increasing. The remaining of 3R-M phase is due to deform α phase [21]

Fig. 5.22 shows the identical area of SEM image and EBSD result of specimen B deformed at 18.5%. In SEM image shown in **Fig. 5.22a**, dark-grey and white contrast color were appeared. With the EBSD result shown in **Fig. 5.22b**, it can be confirmed that dark-gray in **Fig. 5.22a** is 3R-M phase and bright-gray area is matrix phases. Nanoindentation test was carried out to measure the nanohardness of each phase. The nanohardness of matrix phases is 2.64GPa. The nanohardness of 3R-M phase is

3.16GPa, which is harder than the matrix phases. For specimen C, once the tensile

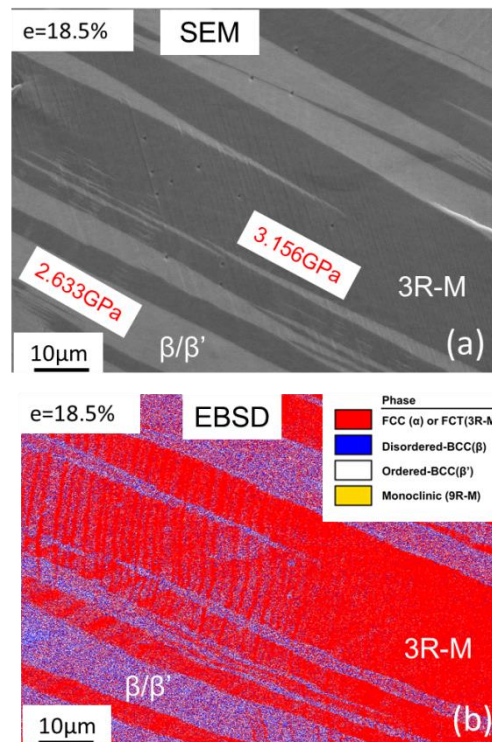


Figure 5.22 shows SEM image of the specimen C tensile deformed at (a) 18.5 % and (b) the identical area of EBSD phase map. The points in SEM image are the indentations of the Nanoindentation test.

strain become larger than 8%, 9R-M phase began to transform to 3R-M phase (Figure 5.21). It also found the similar phase transformation appear in Cu-38.5 wt pct Zn alloy tensile deformed at room temperature [19]. During continuous tensile deformation, the diffraction peak intensity of 3R-M phase was increasing, which indicates the content of 3R-M phase was continuous increasing. Hardness of each phase in specimens and phase's volume fraction can affect the strength in specimens. For specimen C,

increasing the tensile strength is due to increasing the volume fraction of hard 3R-M phase (Figure 5.19) [22]. The tensile deformation behavior in specimen C is similar to “TRIP” effects in austenite steels [23]. It has been reported that after unloading the specimen, 3R-M phase will reverse to 9R-M phase, and 9R-M phase will reverse to β/β' phase [21].

For the specimens A, B and C, the soft α was permanently deformed during plastic deformation. **Fig. 5.7 and Fig. 5.14** show high GAM values in deformed α phase, which indicate high dislocation density, was in α phase. Therefore, 3R-M phase will not fully reverse back to 9R-M phase due to deform α phase [21]. Although the intensity of diffraction peak of 3R-M phase decrease after unloading, the diffraction peak of 3R-M phase is still remain in **Fig. 5.21**.

5.4 Conclusion

In the present Chapter, microstructure and mechanical properties of a Cu-40wt pct Zn alloy having a dual phase microstructure has been studied. Main results are summarized as follows.

1. Different volume fraction of α phase specimens A ($f_{\alpha}=75.1\%$), B ($f_{\alpha}=55.6\%$) and C ($f_{\alpha}=18.4\%$) were obtained after heat treatment. Specimen A and specimen B contain α (FCC) phase, β (Disordered-BCC) phase, β' (Ordered-BCC) phase and 3R-M phase. Specimen C contain α (FCC) phase, β (Disordered-BCC) phase and β' (Ordered-BCC) phase.
2. For specimens A, B and C, increasing of the yield strength is due to reducing the volume fraction of soft α phase.
3. For specimens A and B, GAM maps show soft α phase exhibits higher GAM values than in hard β/β' phase. This result was indicates that the deformation of soft α phase deformed more than the deformation of hard β/β' phase during tensile deformation. The deformed soft α phase has high density of dislocations and fine substructures which can increase its interior misorientation.
4. In-situ neutron diffraction results show hard 3R-M phase and matrix phases (β and β'

phases) show higher lattice strain than α phase at a tensile stress after specimen yielding, which indicate that 3R-M phase and matrix phases (β and β' phases) bear more tensile stress after yielding result in enhancing the work hardening in the specimens.

5. The deformation of specimen C shows shape memory effect (SME) and superelasticity (SE), which like TRIP effect in metastable austenite steels. The significant increase in strain-hardening is due to formation of hard 3R-M phase during deformation.

References

- [1] M. Rashid, SAE Technical Paper, 1977.
- [2] Y. Mazaheri, A. Kermanpur, A. Najafizadeh, *Isij Int*, 55 (2015) 218-226.
- [3] N. Saeidi, F. Ashrafizadeh, B. Niroumand, *Mat Sci Eng a-Struct*, 599 (2014) 145-149.
- [4] A. Karmakar, R.D.K. Misra, S. Neogy, D. Chakrabarti, *Metall Mater Trans A*, 44A (2013) 4106-4118.
- [5] Y. Kang, Q. Han, X. Zhao, M. Cai, *Mater Design*, 44 (2013) 331-339.
- [6] Y. Chen, E. Wang, Y. Guo, W. Chen, The law of the grain size changing in the warm tension test for the B340/590DP dual-phase steel, in: H.X. Zhang, Y. Han, F. Chen, J. Wen (Eds.) *Materials and Computational Mechanics*, Pts 1-3, 2012, pp. 1264-1268.
- [7] P.R. Mondi, V.S. Sarma, S. Sankaran, *T Indian I Metals*, 64 (2011) 89-92.
- [8] M. Calcagnotto, Y. Adachi, D. Ponge, D. Raabe, *Acta Mater*, 59 (2011) 658-670.
- [9] K. Mukherjee, S.S. Hazra, M. Militzer, *Metall Mater Trans A*, 40A (2009) 2145-2159.
- [10] M.R. Akbarpour, A. Ekrami, *Mat Sci Eng a-Struct*, 477 (2008) 306-310.
- [11] J. Zhang, H. Di, Y. Deng, R.D.K. Misra, *Materials Science and Engineering: A*, 627

(2015) 230-240.

[12] Q. Han, Y. Kang, P.D. Hodgson, N. Stanford, *Scripta Mater*, 69 (2013) 13-16.

[13] D. Das, P.P. Chattopadhyay, *J Mater Sci*, 44 (2009) 2957-2965.

[14] R. Zhu, S. Li, I. Karaman, R. Arroyave, T. Niendorf, H.J. Maier, *Acta Mater*, 60 (2012) 3022-3033.

[15] Y.F. Shen, L.N. Qiu, X. Sun, L. Zuo, P.K. Liaw, D. Raabe, *Mat Sci Eng a-Struct*, 636 (2015) 551-564.

[16] C.G. Lee, S.J. Kim, T.H. Lee, S.H. Lee, *Mat Sci Eng a-Struct*, 371 (2004) 16-23.

[17] J. Abe, T. Hattori, K. Komatsu, H. Arima, M. Arakawa, A. Sano, H. Kagi, S. Harjo, T. Ito, A. Moriai, K. Aizawa, M. Arai, W. Utsumi, *Journal of Physics: Conference Series*, 215 (2010) 012023.

[18] Y.F. Hsu, W.H. Wang, *Mater Charact*, 48 (2002) 1-10.

[19] Y.F. Hsu, W.H. Wang, C.M. Wayman, *Metall Trans A*, 22 (1991) 1479-1490.

[20] N. Haberkorn, A.M. Condo, M. Sirena, F. Soldera, F.C. Lovey, *Mater Lett*, 124 (2014) 256-260.

[21] Y.F. Hsu, W.H. Wang, C.M. Wayman, *Metall Mater Trans A*, 30 (1999) 729-739.

[22] T.A. Schroeder, C.M. Wayman, *Acta Metallurgica*, 26 (1978) 1745-1757.

[23] G. Azizi, H. Mirzadeh, M.H. Parsa, *Mat Sci Eng a-Struct*, 639 (2015) 402-406.

Chapter 6 Summary and conclusions

In the present dissertation, the mechanical properties of dual phase (DP) alloys have been studied. Two kinds of DP alloys have been used to study the mechanical properties from the view point of hardness difference between hard phase and soft phase.

In DP steels, the hardness ratios (hardness between martensite phase and ferrite phase) have been changed by tempering to study the relationship between mechanical properties of DP steel and hardness ratios. The special mechanical properties in DP steels, such as high work hardening ability is considered to related with the deformation behavior of individual phases. To understand the strain partitioning and stress partitioning in DP steel are important to understand the mechanical properties (high work hardening behavior, etc.). However, there is some difficult to distinguish the martensite phase (BCT) and ferrite phase (BCC) by X-Ray and other diffraction methods, especially in low carbon steel ($C < 0.25\%$) which only resulting in small difference between martensite phase and ferrite phase. Therefore, non-ferrous DP alloys are considered to study the mechanical properties by studying the deformation behavior of hard phase and soft phase. Cu-Zn alloy consists of α phase (FCC) and β phase (BCC) is chosen to do the research. The main results in each chapter are

summarized as follows:

In **Chapter 1**, background and purpose of this study were introduced.

In **Chapter 2**, strength and ductility of ferrite and martensite dual phase (DP) steels obtained by intercritical annealing and tempering were clarified in the nanohardness ratios between martensite and ferrite ranging from 1.1 to 1.59. The microstructure and mechanical properties of the dual phase steels were studied by SEM, TEM, Nanoindentation and tensile test at room temperature. The microstructure analysis revealed that tempering process resulted in the carbide precipitation and coarsening of martensite structures. The nanohardness of each phase (martensite and ferrite) decreased with increasing the tempering temperature. The ultimate tensile strength had a linear relationship with nanohardness ratio of martensite and ferrite. On the other hand, the uniform elongation firstly did not change by tempering at the temperature below 400 °C, but then decreased by tempering at the temperature above 400 °C with decreasing the nanohardness ratio. It was concluded that the nanohardness ratio can be a good parameter for controlling the mechanical properties of dual phase steels. In addition, the strength and ductility are usually show tradeoff

relationship in traditional steels (plain-carbon steels, martensite steels, etc.). However, dual phase (DP) steel with various hardness ratios between martensite and ferrite shows a new relationship which breaks the tradeoff relationship between strength and elongation. With increasing the tensile strength, the uniform elongation maintained in DP steels ($M/F \geq 1.34$, M/F : refers hardness ratio between martensite phase and ferrite phase in this study). This new relationship in DP steel was explained in terms of plastic instability. The work hardening rate in DP steels ($M/F \geq 1.34$) increased to keep DP steel stable resulting in maintaining the uniform elongation.

In **Chapter 3**, local deformation behavior of martensite phase and ferrite phase in DP steels with various hardness ratios between martensite phase and ferrite phase was studied. DIC results of the local strain distribution in martensite phase and ferrite phase in low hardness ratio specimen ($M/F=1.1$). The average local strain in martensite phase ($\epsilon_{M,ave}$) and ferrite phase ($\epsilon_{F,ave}$) are both increased with increasing tensile strain. Both high strain region and low strain region in ferrite phase and martensite phase are shifted into larger strain level indicates that the deformation in martensite phase and in ferrite phase is relatively homogeneous. It can be seen the line-like high strain was generated in the strain map and propagates through martensite

phase and ferrite phase without considering the phase's type. On the other hand, DIC results of the local strain distribution in martensite and ferrite phase in specimens having high hardness ratios ($M/F \geq 1.34$) show that the low strain region in martensite and ferrite phase is located in the small strain region, while the high strain region in martensite and ferrite is shifted into larger strain level during tensile deformation. This indicates that the deformation in martensite phase and in ferrite phase is relatively inhomogeneous. The high strain show strip-like morphology and rod-like morphology in high hardness ratio specimens ($M/F \geq 1.34$). The present result suggests that the morphology of the local high strain can be controlled by changing the nanohardness ratio between martensite and ferrite in DP steels. It is found that the strain ratio (local strain partitioning between ferrite and martensite) increase with increasing nanohardness ratio between martensite and ferrite at similar tensile strain. Large difference of strain partitioning between ferrite and martensite will generate large phase stress which enhance the strain hardening in the specimens.

In **Chapter 4**, Comparison of the deformation behaviors in martensite based DP steel ($V_m=80\%$, V_m :Volume fraction of martensite) and ferrite based DP steel ($V_m=29\%$) with various hardness ratios between martensite and ferrite. EBSD results show more

low angle boundaries ($2^\circ < \Theta < 15^\circ$) in martensite-based DP steel. The specimen tempered at 600 °C, low angle boundaries in ferrite based DP steel are almost disappeared and martensite phase with high angle boundaries ($\Theta \geq 15^\circ$) show recrystallized structure in ferrite-based DP steel. In ferrite-based DP steel, the tensile strength not linear decrease with reducing nanohardness ratios (M/F). The uniform elongation change with different the nanohardness ratios in ferrite-based DP steel shows a similar tendency as it in martensite-based DP steel. The local strain distribution in martensite phase and ferrite phase in ferrite-based DP steel is showing similar tendency as it shown in martensite based DP steel shown in Chapter3. Here the high hardness ratio refers to $M/F \geq 1.26$, and low hardness ratio refers to $M/F < 1.26$. The morphology of high strain in ferrite based DP steel specimens show strip-like morphology and line-like morphology in high hardness ratio specimen and low hardness ratio specimen, respectively. Under similar hardness ratio, the specimen in ferrite-based DP steel and martensite based DP steel shows different strain ratios. The strain ratio in martensite-based DP steel is higher than ferrite-based DP steel. It is suggest that the strain hardening ability in martensite-based DP steel is higher than ferrite-based DP steels with the similar hardness ratio between martensite phase and ferrite phase.

In **Chapter 5**, microstructure and mechanical properties of a Cu-40wt pct Zn alloy having a dual phase microstructure has been studied. The results show that the increment of the yield strength is due to reducing the volume fraction of soft α phase. GAM maps show that soft α phase exhibits higher GAM values than in hard β/β' phase. This result was indicates that the deformation of soft α phase deformed more than the deformation of hard β/β' phase during tensile deformation. The deformed soft α phase has high density of dislocations and fine substructures which can increase its interior misorientation. In-situ neutron diffraction results show hard 3R-M phase and matrix phases (β and β' phases) show higher lattice strain than α phase at a tensile stress after specimen yielding, which indicate that 3R-M phase and matrix phases (β and β' phases) bear more tensile stress after yielding result in enhancing the work hardening in the specimens. The deformation of specimen having 18.4% α phase shows shape memory effect (SME) and superelasticity (SE), which like transformation induced plasticity(TRIP) effect in metastable austenite steels. The significant increase in strain-hardening is due to formation of hard 3R-M phase during deformation.

In **Chapter 6**, concluded the whole research findings in this research work.

Acknowledgement

I would like to express my sincere gratitude to my supervisor Professor Nobuhiro Tsuji for the continuous support of my Ph.D. study, for his patience, motivation, and immense knowledge. His guidance helped me in all the time of research and writing of this thesis. I would like to thank my co-supervisor assistant Professor Daisuke Terada in Kyoto University, now associate Professor in Chiba Institute of Technology, for his value help and discussions. I also thank associate Professor Akinobu Shibata for his help. Many thanks to associate Professor Nago Kamikawa for his help on analysis digital image correlation result. I also thank Nobuharu Sasaki for his help on wavelength dispersive spectrometer measurement.

Besides, I would like to thank all the members in Tsuji-Lab for your help and engorgement.

Finally, I would like to appreciates the support of the Japanese Government (Monbukagakusho: MEXT) Scholarship.

List of publications

International Proceeding Papers :

Hongxing Li, Si Gao, Yanzhong Tian, Daisuke Terada, Akinobu Shibata, Nobuhiro Tsuji.
“Influence of Tempering on Mechanical Properties of Ferrite and Martensite Dual Phase Steel” [J]. Materials Today: Proceedings, 2015, 2: S667-S671.

Presentation in International Conferences :

1. Hongxing Li, Daisuke Terada, Tsuji Nobuhiro. “Unique Mechanical Property of Cu-Zn Dual Phase Alloy”. 2nd Summer School and Symposium on Nanometals, Weihai, China. 2013 (Poster)
2. Hongxing Li, Daisuke Terada, Akinobu Shibata, Nobuhiro Tsuji. “Influence of tempering on the mechanical properties and microstructure in ferrite and martensite dual phase steel”. International Conference on Martensitic Transformations 2014 (ICOMAT 2014) . Bilbao, Spain. 2014 (Poster)
3. Hongxing Li, Mohit Joshi, Tilak Bhattacharjee, Daisuke Terada, Akinobu Shibata , Nobuhiro Tsuji, “Microstructure and mechanical properties of Cu-Zn dual phase alloy”.

17th International Conference on the Strength of Materials (ICSMA-17) Brno, Czech.
2015 (Oral).

Presentation in Domestic Conferences (Japan) :

1. Hongxing Li, Daisuke Terada, Akinobu Shibata, Nobuhiro Tsuji. “Effect of tempering temperature on the mechanical properties and microstructure of ferrite and martensite dual phase steel”. 167th The Iron and Steel Institute of Japan (ISIJ) spring conference. Tokyo, Japan. 2014 (Poster)

2. Hongxing Li, Daisuke Terada, Akinobu Shibata, Nobuhiro Tsuji. “Influence of tempering on the mechanical properties and microstructure in ferrite and martensite dual phase steel”. 168th The Iron and Steel Institute of Japan (ISIJ) autumn conference. Nagoya, Japan. 2014 (Oral)

3. Hongxing Li, Si Gao, Yanzhong Tian, Daisuke Terada, Akinobu Shibata, Nobuhiro Tsuji. “Effect of hardness ratio between two phases on deformation behavior of low-carbon dual phase steel composed of ferrite and martensite”. The Japan Institute of Metals and Materials (JIM) 156th Annual Spring Meeting. Tokyo, Japan. 2015 (Oral)

4. Hongxing Li, Si Gao, Daisuke Terada, Akinobu Shibata, Naoya Kamikawa Nobuhiro

Tsuji. “Effect of hardness ratio between two phases on strain partitioning of low-carbon dual phase steel composed of ferrite and martensite”. 170th The Iron and Steel Institute of Japan (ISIJ) autumn conference. Kyushu, Japan. 2015 (Oral)

Award:

Hongxing Li, Daisuke Terada, Akinobu Shibata, Nobuhiro Tsuji. “Effect of tempering temperature on the mechanical properties and microstructure of ferrite and martensite dual phase steel”. 167th The Iron and Steel Institute of Japan (ISIJ) spring conference. Tokyo, Japan 2014 (Poster Award for Effort.)